UNIVERSIDADE FEDERAL DE MINAS GERAIS

Instituto de Ciências Exatas

Programa de Pós-Graduação em Química

Tercio Paulo Felix Xisto

FORMATION OF IRON VACANCIES IN TROILITE AND MONOCLINIC PYRRHOTITE AND EARLY OXIDATION MECHANISMS ON MONOCLINIC SURFACES: a DFT study

Belo Horizonte

2025

UFMG / ICEX / DQ. 1.668ª
D. 908ª

Tercio Paulo Felix Xisto

FORMATION OF IRON VACANCIES IN TROILITE AND MONOCLINIC PYRRHOTITE AND EARLY OXIDATION MECHANISMS ON MONOCLINIC SURFACES: a DFT study

Dissertação apresentada ao Programa de Pós-Graduação em Química da Universidade Federal de Minas Gerais, como requisito parcial à obtenção do título de Mestre(a) em Química.

Orientador(a): Prof. Hélio Anderson Duarte

Belo Horizonte
2025

Ficha Catalográfica

X6o
2025
D

Xisto, Tercio Paulo Felix.
Formation of iron vacancies in troilite and monoclinic pyrrhotite and early oxidation mechanisms on monoclinic surfaces [manuscrito] : a DFT study / Tercio Paulo Felix Xisto. 2025.
107 f. : il., gráfs., tabs.

Orientador: Hélio Anderson Duarte.

Dissertação (mestrado) – Universidade Federal de Minas Gerais – Departamento de Química.
Bibliografia: f. 80-92.
Apêndices: f. 93-107.

1. Físico-química – Teses. 2. Funcionais de densidade – Teses. 3. Pirrotita – Teses. 4. Ferro – Teses. 5. Equilíbrio termodinâmico – Teses. 6. Minas – Drenagem – Teses. 7. Oxidação – Teses. 8. Mecânica quântica – Teses. 9. Sulfeto de ferro – Teses. I. Duarte, Hélio Anderson, Orientador. II. Título.

CDU 043

Elaborada por Sérgio Ferreira da Silva – Bibliotecário – CRB6-2719.

UNIVERSIDADE FEDERAL DE MINAS GERAIS

UFMG
Programa de Pós-Graduação em Química
Departamento de Química - ICEx

química
pós-graduação-ufmg

" Formation Of Iron Vacancies In Troilite And Monoclinic Pyrrhotite And Early Oxidation Mechanisms On Monoclinic Surfaces: A DFT Study"

Tercio Paulo Felix Xisto

Dissertação aprovada pela banca examinadora constituída pelos Professores:

Prof. Hélio Anderson Duarte - Orientador
UFMG

Prof. Heitor Avelino de Abreu
UFMG

Prof. Luciano Andrey Montoro
UFMG

Belo Horizonte, 17 de julho de 2025.

[

Documento assinado eletronicamente por **Helio Anderson Duarte**, **Professor do Magistério Superior**, em 17/07/2025, às 12:30, conforme horário oficial de Brasília, com fundamento no art. 5º do Decreto nº 10.543, de 13 de novembro de 2020.

Documento assinado eletronicamente por **Heitor Avelino de Abreu**, **Professor do Magistério Superior**, em 17/07/2025, às 15:01, conforme horário oficial de Brasília, com fundamento no art. 5º do Decreto nº 10.543, de 13 de novembro de 2020.

Documento assinado eletronicamente por **Luciano Andrey Montoro**, **Professor do Magistério Superior**, em 18/07/2025, às 11:19, conforme horário oficial de Brasília, com fundamento no art. 5º do Decreto nº 10.543, de 13 de novembro de 2020.

A autenticidade deste documento pode ser conferida no site https://sei.ufmg.br/sei/controlador_externo.php?acao=documento_conferir&id_orgao_acesso_externo=0, informando o código verificador **4388314** e o código CRC **8FF9FC2C**.

Referência: Processo nº 23072.243873/2025-23 SEI nº 4388314

ACKNOWLEDGMENTS

I would like to thank my mother, Amarilis, and my father, Paulo, who are the foundation of the person I am today. I will be forever grateful for the love, care, and education they have given me throughout my life. To my grandparents, Vovô Caneta and Vovó Martinha, my gratitude is just as great. Everything you have done for me, in every stage of my life, means more than words can express. I know that the best parts of who I am come from you.

I also thank my entire family — My brother Arthur, my aunt Eliza, my cousins Maria Alice, Ana Beatriz, Samuel, and everyone else who, in moments of joy or difficulty, were always by my side.

To my childhood friends, who are still a blessing in my life to this day — my forever Discord crew: Davi, Francisco, Lacort, Juninho, and the whole gang — thank you for all the great moments, laughs, and nonsense we shared online.

I'm grateful to my lab colleagues — Selma, Herick, Pedro, Julia, Nalura, Ana Clara, Guilherme, Amós, Vinícius, and especially Edson — for being essential during this chapter of my life.

A special thank you to my advisor, Professor Hélio Duarte, for the partnership, the guidance, the support, the stories, and the friendly conversations. Thank you for showing me, so naturally, how it is possible to be happy doing science.

I am also deeply grateful to my dear friend Marilia for her patience and companionship over these past two years. Thank you also to Jorge, for all your support, advice, help, and friendship.

I acknowledge UFMG, CNPq, CAPES, FAPEMIG, INCT-Acqua, and RenovaMin for funding and supporting this research.

And finally, I thank God for everything — for placing all these wonderful people in my life. I truly believe that each of you was chosen by Him to be part of my journey. He has never abandoned me, and I trust that He never will. My heartfelt thanks to all of you.

“This is not the end, not even the beginning of the end, but it is, perhaps, the end of the beginning.” (Winston Churchill, Battle of El Alamein, 1942).

ABSTRACT

Pyrrhotite is a family of iron sulfide minerals with different degrees of non-stoichiometry, resulting from the presence of iron vacancies in its structure. These structural defects directly influence the physical and chemical properties of the material, especially its thermodynamic stability and electronic behavior. Understanding these effects is essential, considering that monoclinic pyrrhotite is common in geological environments and plays a relevant role in the generation of acid mine drainage (AMD). In this work, Density Functional Theory (DFT) calculations combined with the quasi-harmonic approximation were used to investigate the formation of iron vacancies in troilite and monoclinic pyrrhotite, as well as the thermodynamic behavior of these defective structures at different temperatures. Structures with varying iron vacancy concentrations were modeled, and for each defective configuration, the Helmholtz free energy was calculated, including electronic, vibrational, and configurational contributions. The results show that the monoclinic phase with 12.5% iron vacancies becomes the most stable around 500 K, while the hexagonal troilite structure becomes thermodynamically preferred above 700 K. This gradual symmetry change with increasing temperature agrees with experimental observations and provides a theoretical explanation for the phase transformation observed in nature. In addition to bulk analysis, the most stable surface of monoclinic pyrrhotite, identified as (001)-3, was investigated. Different molecular oxygen adsorption mechanisms were simulated, revealing significant charge transfer between surface atoms and O_2, along with the formation of covalent bonds in certain configurations, indicating the initial stages of surface oxidation. The projected density of states (PDOS), Electron Localization Function (ELF), and Bader charge analysis supported the characterization of these processes. This study provides a solid theoretical basis for understanding the thermodynamic stability of pyrrhotite and the initial oxidation steps on its surface.

Key-words: DFT; pyrrhotite; iron vacancies; thermodynamic stability; surface oxidation.

RESUMO

A pirrotita é uma família de minerais de sulfeto de ferro com diferentes graus de não estequiometria, resultantes da presença de vacâncias de ferro em sua estrutura. Esses defeitos estruturais influenciam diretamente as propriedades físicas e químicas do material, especialmente sua estabilidade termodinâmica e seu comportamento eletrônico. Compreender esses efeitos é essencial, considerando que a pirrotita monoclínica é comum em ambientes geológicos e desempenha um papel relevante na geração de drenagem ácida de mina (DAM). Neste trabalho, foram realizados cálculos baseados na Teoria do Funcional da Densidade (DFT), combinados com a aproximação quase-harmônica, para investigar a formação de vacâncias de ferro na troilita e na pirrotita monoclínica, bem como o comportamento termodinâmico dessas estruturas defeituosas em diferentes temperaturas. Foram modeladas estruturas com diferentes concentrações de vacâncias até atingir 12,5% de vacâncias. Para cada configuração, foi calculada a energia livre de Helmholtz, considerando as contribuições eletrônica, vibracional e configuracional. Os resultados mostram que a fase monoclínica com 12,5% de vacâncias se torna a mais estável em torno de 500 K, enquanto a estrutura hexagonal da troilita passa a ser preferida acima de 700 K. Essa mudança gradual de simetria com o aumento da temperatura está em acordo com observações experimentais e oferece uma explicação teórica para a transformação de fase observada na natureza. Além da análise em bulk, foi investigada a superfície mais estável da pirrotita monoclínica, identificada como (001)-3. Foram simulados diferentes mecanismos de adsorção molecular de oxigênio, revelando transferência significativa de carga entre os átomos da superfície e o oxigênio, além da formação de ligações covalentes em determinadas configurações, indicando os estágios iniciais do processo de oxidação da superfície. As análises de densidade de estados projetada (PDOS), função de localização eletrônica (ELF) e carga de Bader forneceram suporte para a caracterização desses fenômenos. Este estudo oferece uma base teórica sólida para a compreensão da estabilidade termodinâmica da pirrotita e dos processos iniciais de oxidação na sua superfície.

Palavras-Chave: DFT; pirrotita; vacancias de ferro; estabilidade termodinâmica; oxidação superficial.

LIST OF FIGURES

LIST OF TABLES

LIST OF FIGURES IN THE APPENDIX A

LIST OF TABLES IN THE APPENDIX A

TABLE OF CONTENTS

1 INTRODUCTION

This study reports a computational modeling investigation of two materials from the pyrrhotite group: troilite (FeS) and monoclinic pyrrhotite (Fe_7S_8). It aims to contribute to the understanding of the thermodynamic processes involved in their synthesis and to explore the initial steps of the oxidation mechanism of monoclinic pyrrhotite.

We carried out an analysis of the iron vacancy formation process in the structures of troilite and monoclinic pyrrhotite, evaluating the thermodynamic properties associated with the vacancy formation. We also investigated the oxidation process of monoclinic pyrrhotite, one of the most abundant sulfide minerals. Despite its widespread occurrence, this mineral has limited economic value, being classified as a secondary mineral and often discarded in tailings dams after ore beneficiation. The exposure of pyrrhotite to humid and oxidizing environments can lead to sulfur leaching and the formation of sulfuric acid. This phenomenon is called acid rock drainage which is responsible for important environmental impact [1], [2], [3].

1.1 Pyrrhotite, sulfide minerals, and acid drainage

Sulfide minerals are compounds in which sulfur anions are bonded to metallic cations. This class of minerals represents the primary and most significant source of nonferrous metals of economic and industrial interest [4]. In general, large deposits of these minerals are not widespread across the Earth's crust, however, the most substantial concentrations are found in regions such as China, Russia, Australia, and Canada [1], [2], [5].

Although numerous sulfide minerals are known, only five occur with sufficient abundance to be commonly found as accessory minerals in rocks. These include pyrite (FeS_2), pyrrhotite ($Fe_{1-x}S; 0 \leq x \leq 0.125$), galena ($PbS$), sphalerite ($ZnS$), and chalcopyrite ($CuFeS_2$). Among them, the iron sulfides – pyrite and pyrrhotite – are the most widely distributed in the Earth's crust [6].

In Brazil, gold mining regions have historically been associated with the exploration of sulfide minerals. In the Ouro Preto region, two mines – Piquete and Santa Efigênia – were

dedicated to the extraction of pyrite for export through the ports of Rio de Janeiro. However, following the end of World War II, these mines were decommissioned due to the decline in pyrite prices, the increasing difficulty of extraction, and the acidification of the mine interiors caused by acid drainage [7].

Many metallic elements of economic interest are found among sulfide minerals. Iron sulfides, the most abundant within this class, are often associated with valuable metallic elements such as Ag, Au, Co, Cu, Ni, Pb, Pt, and Zn. In addition to their economic relevance, sulfide minerals can also have significant environmental impacts. When exposed to oxidizing and humid conditions, these minerals may undergo sulfur oxidation, leading to the formation of sulfuric acid [6], [8], [9], [10]. This acid can leach toxic metals into the surrounding soil and aquatic systems – a phenomenon known as Acid Rock Drainage (ARD).

This environmental impact can also have an anthropogenic origin, particularly in the context of mining tailings dams, leading to what is known as Acid Mine Drainage (AMD). Various metallic elements are associated with iron sulfides and can become solubilized under acidic conditions. The most common elements found in acid mine drainage include As, Ba, Cd, Cu, Mn, Mo, Ni, Pb, Se, and Zn [9], [10].

One of the consequences of acid drainage is the bioaccumulation and biomagnification of metallic elements. Once leached from minerals, these elements can be assimilated by microorganisms and other organisms, such as fish and crustaceans, in a process known as bioaccumulation. When these metals accumulate progressively along the food chain, the phenomenon is referred to as biomagnification [11].

Pyrrhotite ($Fe_{1-x}S; 0 \leq x \leq 0.125$) is one of the sulfide minerals particularly susceptible to oxidation under acidic conditions. This iron sulfide mineral is found in numerous deposits worldwide, especially in Russia, China, Australia, and Canada [5], [12]. It is typically associated with igneous and volcanic rocks and is often found in mineral deposits alongside pyrite, sphalerite, galena, and chalcopyrite [1].

Figure 1 shows images of two rivers affected by acid drainage: the Tinto and Odiel Rivers. Both are part of the Huelva estuary, located in Spain, within a region known as the Pyrite Belt. The extensive exploration of sulfide minerals in this area has led to severe environmental contamination [13], [14].

Figure 1: Odiel River in Spain [15].

Sulfide minerals are commonly classified based on their fundamental crystal structures. Pyrrhotite family of materials belongs to the nickeline ($NiAs$) group. Materials with structures derived from nickeline emerge due to structural distortions, ordered atomic omissions, or elemental substitutions. The term pyrrhotite refers to a family of stoichiometric and non-stoichiometric iron sulfide structures [16]. The most common forms of pyrrhotite include the monoclinic structure (4C), troilite (2C), and intermediate forms such as 5C, 6C, and 11C [17], see Table 1. A common way to distinguish these structures is by the parameter C, which indicates how much the length of the pyrrhotite unit cell differs from that of the nickeline unit cell [4], [16].

Troilite corresponds to the first direct derivative of the $NiAs$ structure, where the Ni and As atoms are replaced by Fe and S, respectively. The non-stoichiometric forms of troilite arise from the formation of iron vacancies, in which Fe atoms are systematically removed from the crystal structure across a concentration range from $x = 0$ to $x = 0.125$. This vacancy formation gives rise to all structures within the pyrrhotite group. The ordered removal of iron atoms ultimately leads to the formation of monoclinic pyrrhotite (Fe_7S_8), which is the most iron-deficient member of this group, featuring a 12.5 % iron vacancy. Table 1 lists the naturally occurring pyrrhotite structures, highlighting the crystal lattice parameters *a*, *b*, and *c*, which represent the unit cell dimensions of the pyrrhotite, and *A*, *B*, and *C*, which correspond to the unit cell dimensions of the nickeline structure [4], [5], [17].

Table 1: Naturally occurring structures of pyrrhotite

Molar composition (% of Fe)	Structure	Structure type (unit cell dimensions in Å)	Identification
50.0 FeS	Hexagonal	$a = \sqrt{3}\,A, c = 2C$ a=5.96, c=11.75	Troilite 2C
46.7 Fe_7S_8	Monoclinic	$a = 2\sqrt{3}\,A, b = 2A, c = 4C$ a=11.90, b=6.87 c=22.87 β=90º30’	Magnetic pyrrhotite 4C
47.4 Fe_9S_{10}	Hexagonal	$a = 2A, c = 5C$ a=6.88, c=28.7	Pyrrhotite 5C
47.8 $Fe_{11}S_{12}$	Hexagonal	$a = 2A, c = 6C$ a=6.89, c=34.48	Pyrrhotite 6C
47.6 $Fe_{10}S_{11}$	Hexagonal	$a = 2A, b = 2B, c = 11C$ a=6.89, b=11.95 c=63.18	Pyrrhotite 11C

During ore beneficiation, pyrrhotite is often classified as a secondary mineral – that is, a mineral of low economic value – since the main goal of processing is the recovery of valuable metals such as Cu, Pb, Zn, Au, Pt, and Ag [2]. As a result, pyrrhotite is commonly discarded in tailing dams, where it remains exposed to humid and oxidizing environments. Under these conditions, pyrrhotite can undergo oxidation, leading to the formation of sulfuric acid. This process can result in the leaching of toxic metals into soil and water bodies, causing what is known as acid mine drainage.

The chemical composition of pyrrhotite varies between troilite (FeS) and monoclinic pyrrhotite (Fe_7S_8), resulting in distinct magnetic and electrical properties [18], [19]. Troilite, for instance, is an antiferromagnetic mineral in which the iron layers exhibit alternating magnetization, with an experimental band gap of 0.04 eV [18], [20]. In contrast, monoclinic pyrrhotite is ferromagnetic and displays non-uniform magnetization between the iron layers due to the presence of vacancies in the structure. These vacancies prevent the layers from exhibiting perfectly opposing magnetizations. Experimentally, the magnetization of monoclinic pyrrhotite ranges from 2.0 a 2.5 μB [18].

1.2 Crystal Structure, Electronic Properties, Synthesis, and Chemical Composition of troilite and monoclinic pyrrhotite

Troilite, with the chemical formula FeS, has a unit cell belonging to the hexagonal crystal system, with lattice parameters ***a* = *b* = 5.966 Å,** and ***c* = 11.765 Å** [21]. In its structure, each iron atom is coordinated to six sulfur atoms. Figures 2a and 2b show, respectively, the troilite mineral and its unit cell, which consists of 24 atoms – 12 iron and 12 sulfur.

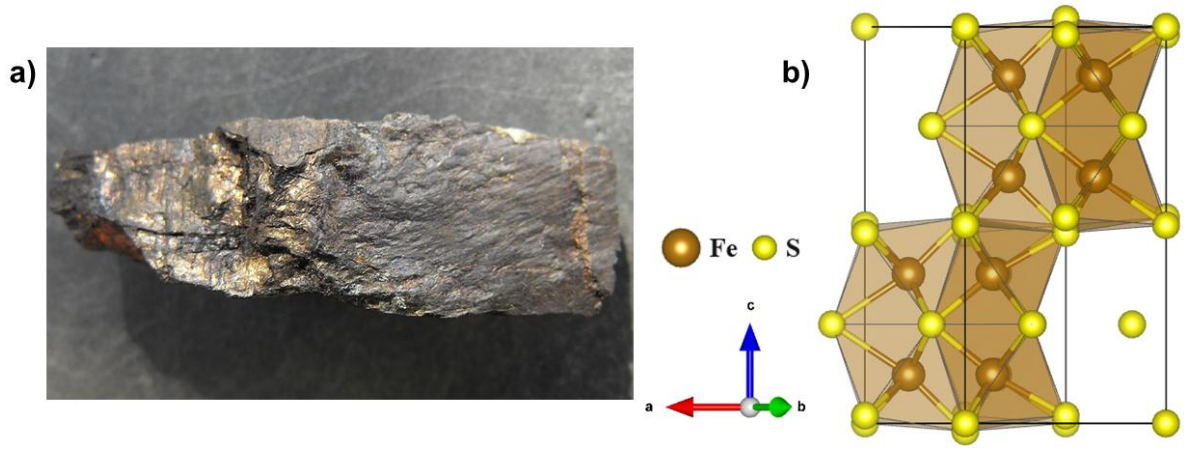

Figure 2: a) Image of troilite [22]; b) Representation of the troilite unit cell.

Monoclinic pyrrhotite, with the chemical formula Fe_7S_8, has a larger unit cell with lattice parameters ***a* =11.90 Å, *b* = 6.87 Å,** and ***c* = 22.87 Å** [23], [24]**.** However, due to the high number of atoms in this structure, its use in computational simulations becomes unfeasible. For this reason, we adopted a simplified monoclinic pyrrhotite structure proposed by Powell et al. [25], with lattice parameters ***a*=11.897 Å, *b*=6.8586 Å,** and ***c*=12.891 Å**. In this model, the authors describe the same 4C ordered-defect structure but in a smaller and more conventional unit cell, using the space group C2/c instead of the unconventional F2/d employed in earlier works. This choice preserves the essential features of the vacancy ordering and the structural distortion, while reducing the number of atoms in the cell. From a computational perspective, using a smaller unit cell is highly advantageous, as it significantly decreases the computational cost by reducing the number of atoms, k-points, and plane waves required in density functional theory (DFT) calculations. Similar to troilite, all iron atoms in the monoclinic pyrrhotite structure are coordinated to six sulfur atoms. Figure 3a and 3b show, respectively, the monoclinic pyrrhotite mineral and its unit cell, which contains 60 atoms – 28 iron and 32 sulfur.

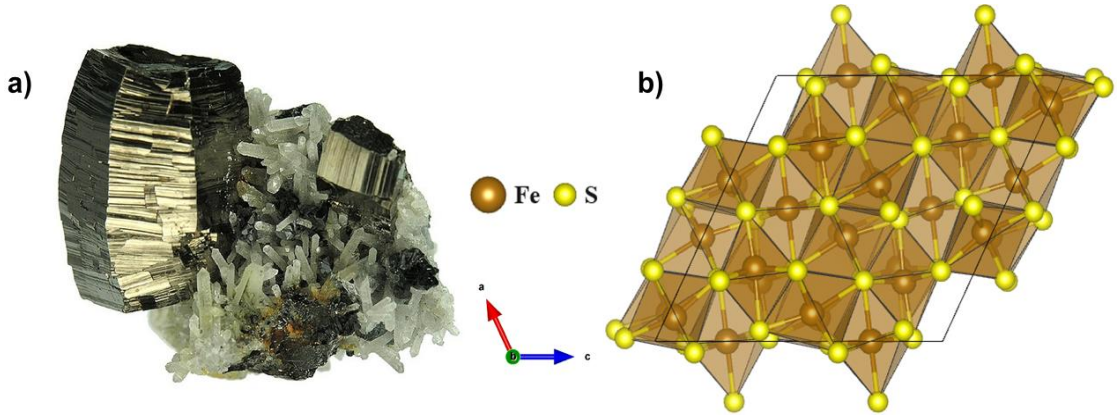

Figure 3: a) Image of monoclinic pyrrhotite [26]; b) Representation of the monoclinic pyrrhotite unit cell.

One notable feature of the monoclinic pyrrhotite crystal structure is the alternation of iron layers with and without vacancies. Studies suggest that the thermodynamic stability of pyrrhotite is influenced by the presence of Fe^{3+} ions near the vacancy-containing planes [23]. This structural disorder, caused by the lack of iron, alters the mineral's magnetic and electronic properties. It is therefore believed that the stability of monoclinic pyrrhotite is directly related to the distinct electronic distribution among the iron atoms located in layers with and without vacancies [27].

Experimental investigations conducted by Pratt et al. [28] using X-ray Photoelectron Spectroscopy (XPS) demonstrated that monoclinic pyrrhotite contains both Fe^{2+} and Fe^{3+} ions coordinated to sulfur atoms, with sulfur predominantly found as S^{2-}. However, disulfide species (S_2^{2-}) were also observed in small amounts. These results indicate that the surface of monoclinic pyrrhotite may exhibit different chemical states compared to its bulk composition.

Pettifer et al. [29] performed Synchrotron Photoemission Spectroscopy (SPES) and X-Ray Adsorption Near Edge Spectroscopy (XANES) analysis to investigate the chemical composition of monoclinic pyrrhotite in both bulk and surface. They found that in the bulk, iron is present as Fe^{2+} and sulfur as S^{2-}. However, after surface formation through cleavage, disulfide (S_2^{2-}) and polysulfide species were detected, indicating a sulfur reconstruction at the mineral surface.

Although similar materials such as pyrite[30], [31], [32], arsenopyrite [31], [32], and chalcopyrite [33], [34] have been extensively studied, there is still a significant lack of detailed investigations specifically addressing the chemical composition of monoclinic pyrrhotite, particularly at the surface level. Environmental impact is expected from the oxidation of pyrrhotite under moist and oxidizing conditions. Therefore, in-depth surface studies are crucial to better understand the chemical and environmental behavior of this material.

The electronic and magnetic properties of troilite have been investigated by Ricci et al. [35] using Density Functional Theory (DFT) based on plane waves. The authors reported that troilite is a semiconductor material with an indirect band gap of 0.49 eV, while the experimentally reported value is only 0.04 eV. This discrepancy was attributed to the exchange-correlation functional used in the calculations, which may underestimate the band gap. Alternatively, the difference between theoretical and experimental values could result from natural samples containing iron vacancies, resembling monoclinic pyrrhotite rather than pure troilite. Their investigation confirmed the antiferromagnetic nature of troilite, in which the iron atoms exhibit alternating spin-up and spin-down orientations along the c-axis, resulting in a net magnetic moment of zero.

Zhao et al. [5] investigated the electronic and magnetic properties of monoclinic pyrrhotite (Fe_7S_8) and hexagonal pyrrhotite (Fe_9S_{10}), the two most abundant forms within the pyrrhotite group. In contrast to troilite, both structures exhibit metallic behavior, with no band gap. Electronic density of states (DOS) calculations revealed spin polarization in monoclinic pyrrhotite, and its magnetic properties were shown to vary with iron vacancy concentration.

Regarding the synthesis of this material, Figueroa et al. [36] explored the hydrothermal synthesis of pyrrhotite nanostructures at 450 K for 48 hours, using $Fe(NO_3)_3 \cdot 9H_2O$ and L-cysteine as iron and sulfur sources. The authors obtained hexagonal pyrrhotite crystals with lattice parameters **a = b = 6.88 Å** and **c= 28.67 Å** and angles **α = β = 90°** and **γ = 120°**, confirming the presence of the Fe_9S_{10} phase through X-ray diffraction, with no evidence of secondary phases such as troilite (FeS), pyrite (FeS_2), or marcasite (FeS_2).

Cantu et al. [37] used solvothermal synthesis to produce monoclinic pyrrhotite nanocrystals for potential application in arsenic removal from contaminated water. During synthesis, two distinct phases were observed: a primary phase corresponding to monoclinic pyrrhotite (Fe_7S_8) and a secondary phase of greigite (Fe_3S_4). The authors suggest that troilite acts as a precursor structure for greigite formation, which may later convert into pyrrhotite or pyrite at temperatures above 570 K [38], [39].

Overall, the synthesis of iron sulfides can lead to a variety of products, with compositions that depend directly on the iron and sulfur source, the synthesis method used, and the reaction temperature [19], [36], [37], [38], [39], [40]. This behavior highlights the structural complexity of pyrrhotite and the need for more detailed studies on its electronic and structural properties.

1.3 Cleavage Surface, Relaxation, and Reconstruction

Some material surfaces may undergo significant changes following the cleavage process. This phenomenon, known as surface relaxation, involves adjustments in the atomic positions to minimize the energy of the exposed surface. In more extreme cases, relaxation can evolve into a process known as reconstruction, in which a substantial reorganization of surface atoms occurs [41]. This modification alters the original atomic structure, directly influencing the chemical reactivity of surface atoms [2].

Surface relaxation and reconstruction become even more relevant when studying oxidative processes occurring on material surfaces. Oxidation can be significantly affected by the atomic configuration of the surface, which is influenced by the atomic relaxation and surface reconstruction process [34], [41]. Therefore, understanding how material surfaces behave after cleavage, and how this process modifies their characteristics, is essential for controlling chemical reactions such as oxidation.

In the case of pyrrhotite, studying the oxidation mechanism is particularly challenging due to the absence of a preferential cleavage plane, which makes it difficult to identify the primary surface where reactions occur. Furthermore, fracturing of the mineral may generate surfaces enriched in sulfur, iron, or a combination of both. Figure 4 schematically illustrates a model of the (001) surface of monoclinic pyrrhotite.

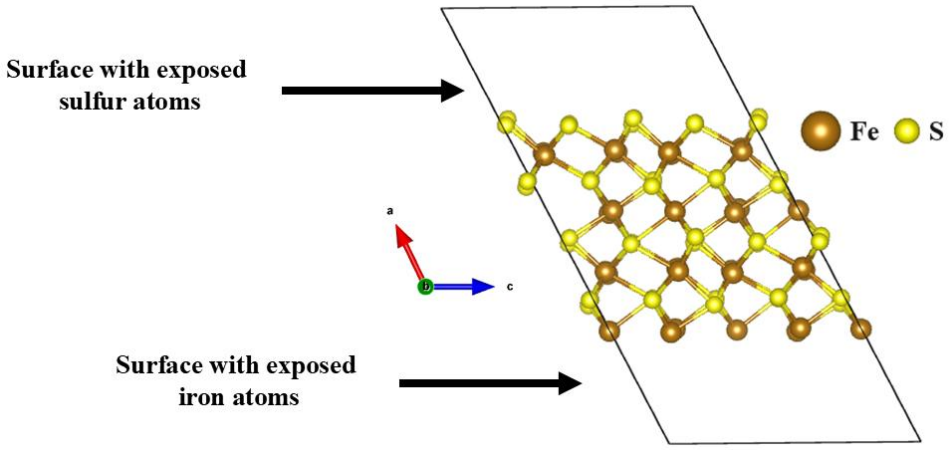

Figure 4: Representation of a model of the pyrrhotite (001) surface.

Chen et al. [2] demonstrated that, following a reconstruction process on the surface of monoclinic pyrrhotite, a significant reorganization of atoms occurred: some sulfur atoms from the layer immediately adjacent to the exposed iron layer migrated to the first surface layer, while the iron atoms shifted to the second layer. Similar observations were made in the present

study, confirming the tendency for atomic rearrangement in this mineral. Further details regarding pyrrhotite reconstruction will be presented in Chapter 5.

Oliveira et al. [34] conducted a study on the reconstruction of different surfaces formed from chalcopyrite bulk using DFT calculations. Their findings revealed a significant surface reconstruction in which sulfur atoms become exposed while the metallic atoms migrate to lower layers, forming a metallic alloy. This behavior appears to be common among sulfide minerals, as it was also observed on the pyrrhotite surface.

Zhao et al. [42] analyzed the stability of various surfaces of monoclinic pyrrhotite, generated from cleavage planes including (001), (010), (100), (101), (011), (110), and (111). They identified that surfaces derived from the (001) plane exhibit the highest stability. In the present study, similar investigations were carried out for the cleavage planes (001), (010), and (100). The results obtained in this work corroborate the findings of Zhao et al. [42], indicating that the surface originating from the (001) cleavage plane is indeed the most stable.

1.4 Oxidation process of monoclinic pyrrhotite

Oxygen is the main oxidizing agent for sulfide minerals when the pH of the medium is above 4. However, when the pH drops below 4, the system dynamics change, and the sulfide minerals become strongly oxidized by Fe^{3+} ions [1]. This behavior is also observed in pyrite, where both oxygen and Fe^{3+} act as oxidizing agents [2], [43]. In a detailed study, Steger [44] investigated the impact of relative humidity on the oxidation rate of pyrrhotite. His results indicated that increasing relative humidity from 35% to 75% significantly accelerates the mineral's oxidation.

The first stage of pyrrhotite oxidation involves its dissolution, resulting in the formation of sulfate ions (SO_4^{2-}), Fe^{2+}, and hydronium ions (H_3O^+) in aqueous solution. When water is present and oxygen acts as the main oxidizing agent, pyrrhotite undergoes oxidation as represented in Eq. (1.1). In this process, sulfur atoms are oxidized from -2 to +6, while iron atoms remain in the +2 oxidation state.

$$Fe_{1-x}S + O_2 \rightarrow (1-x)Fe^{2+} + SO_4^{2-} \quad (1.1)$$

If the environment is sufficiently oxidizing – a condition primarily influenced by the concentration of dissolved oxygen and the pH – some of the Fe^{2+} ions formed may be further oxidized to Fe^{3+}, as described in Eq. (1.2):

$$2Fe^{2+} + \frac{1}{2}O_2 + 2H^+ \rightarrow H_2O + 2Fe^{3+} \quad (1.2)$$

In aqueous solution with a pH lower than 2.2, Fe^{3+} is best represented as the hexaaqua iron (III) species, $[Fe(H_2O)_6]^{3+}$ [45]. As the pH increases, Fe^{3+} ions undergo hydrolysis, leading to the precipitation of $Fe(OH)_3(s)$, which significantly reduces the concentration of Fe^{3+} in solution producing acid, as shown in Eq. (1.3):

$$Fe^{3+} + 3H_2O \rightarrow Fe(OH)_{3(S)} + 3H^+ \quad (1.3)$$

If oxidation occurs under acidic conditions, a significant fraction of Fe^{3+} remains in solution, sustaining the reaction. In this scenario, Fe^{3+} acts as an oxidizing agent in the reaction described by Eq. (1.4):

$$Fe_{1-x}S + 8Fe^{3+} + 4H_2O \rightarrow (9-x)Fe^{2+} + SO_4^{2-} + 8H^+ \quad (1.4)$$

Equations (1.1), (1.2), and (1.4) subsequently describe the acid mine drainage process caused by pyrrhotite. However, in practice, these reactions occur simultaneously. Initially, reaction described by Eq. (1.1) governs the dissolution of pyrrhotite and the formation of Fe^{2+}. Subsequently, Fe^{2+} ions are oxidized to Fe^{3+}, as shown in Eq. (1.2). Finally, as shown in Eq. (1.4), higher concentration of Fe^{3+} accelerate the oxidation of pyrrhotite.

Zhao et al. [12] conducted a detailed investigation of the interaction between oxygen molecules and the surfaces of monoclinic pyrrhotite, pyrite, and marcasite using DFT calculations. In the case of pyrrhotite, they demonstrated that during the adsorption process, the O_2 molecule dissociates, resulting in an adsorption energy of 375.87 KJ/mol. This value indicates a gain in stability and confirms the exothermic nature of the process. Furthermore, a topological analysis of the electron density overlap revealed a strong interaction between the oxygen molecule and the surface of monoclinic pyrrhotite.

Although the literature presents studies on the oxygen adsorption on monoclinic pyrrhotite surfaces [12], as well as investigations related to the adsorption of various collectors aimed at improving the flotation efficiency of the mineral [1], [5], [12], there remains a significant gap in theoretical studies addressing the simultaneous adsorption of water and oxygen. Understanding this process is essential to elucidate the effects of water on the adsorption of other molecules and, consequently, on the overall behavior of pyrrhotite in natural environments and industrial process.

2 OBJECTIVES

The thermodynamic stability and reactivity of minerals are intrinsically linked to their chemical structure and surface configuration, respectively. In this context, the present work aims to investigate, through computational simulations based on Density Functional Theory (DFT), the formation of iron vacancies in the troilite structure, tracking the variation of thermodynamic properties until reaching the chemical composition of monoclinic pyrrhotite with 12.5 % iron vacancies. Additionally, this study seeks to understand the initial stages of the oxidation mechanism of monoclinic pyrrhotite by evaluating the adsorption of oxygen on the mineral surface. The analysis of the process will help elucidate the influence of the electronic structure and surface configuration on pyrrhotite reactivity, providing a basis for understanding the oxidative phenomena that occur in both natural environments and industrial applications.

To achieve the general objectives, the following specific aims were established:

- Establish a calculation protocol capable of accurately reproducing experimental data available in the literature for troilite and monoclinic pyrrhotite;
- Construct iron-deficient structures based on the crystalline structure of troilite;
- Calculate the cohesive energy and the vacancy formation energy for each iron-deficient structure and determine their thermodynamic properties at different temperatures, ranging from 0K to 1000 K;
- Analyze the thermodynamic data and establish the relationship between temperature and iron vacancy concentration;
- Identify the preferential cleavage surface of monoclinic pyrrhotite;
- Assess the reactivity of the pyrrhotite surface in the presence of oxygen.

3 METHODOLOGY

3.1 Computational Chemistry

Computational chemistry is currently an essential tool in the research of materials and crystalline solids. Through physical and mathematical principles, this approach enables the accurate determination of the electronic, mechanical, and thermodynamic properties of materials. To gain a deep understanding of the system's behavior, it is crucial to analyze it at the quantum level, which allows for the capture of interactions and phenomena inaccessible to classical methods.

In this context, first-principle methods – also known as *ab initio* methods – are widely employed to elucidate fundamental properties of crystalline solids, such as band structures, density of states, thermodynamic properties, surface reactivity, and identification of intermediates. Theoretical data obtained through these methods can be correlated with experimental results, enabling a more robust and detailed analysis of the interactions and processes occurring in the investigated materials.

The fundamental equation of computational chemistry is the Schrödinger equation. In 1929, Paul Dirac stated [46]:

"The general theory of quantum mechanics is now complete… The underlying physical laws necessary for the mathematical theory of a large part of physics and the whole of chemistry are thus completely known."

The equation referred to by Dirac in his statement is the Schrödinger equation:

$$\hat{H}\Psi = E\Psi \tag{3.1.1}$$

Where the wave function Ψ is expressed as:

$$\Psi = \Psi(x_1, y, z_1, \omega_1, x_2, y_2, z_2, \omega_2, \dots) \tag{3.1.2}$$

The wave function Ψ it is a complex function consisting of both real and imaginary parts which depends on the coordinates $\vec{r_i}$ of each particle "*i*" and its spin state w_i. The Ψ depends on a large number of variables which makes obtaining an exact solution extremely challenging [47], [48].

The Hamiltonian operator $\hat{H}$ acts on the wave function Ψ, yielding the total energy of the system, which encompasses the kinetic energy of the particles and the potential energy

arising from their interactions. Each nucleus and electron have an associated kinetic energy and interacts via electrostatic forces – known as Coulomb interactions. These include the attraction between nuclei and electrons, as well as electron-electron and nucleus-nucleus repulsions:

$$\hat{H} = -\sum_{A}^{nuc} \frac{\hbar^2}{2M_A} \nabla_A^2 - \frac{\hbar^2}{2m} \sum_{i}^{ele} \nabla_i^2 - \sum_{i}^{ele} \sum_{A}^{nuc} \frac{Z_A \mathrm{e}^2}{4\pi r \varepsilon_0 r_{Ai}} + \sum_{A>B}^{nuc} \frac{Z_A Z_B \mathrm{e}^2}{4\pi r \varepsilon_0 r_{AB}} + \sum_{i>j}^{ele} \frac{\mathrm{e}^2}{4\pi r \varepsilon_0 r_{ij}} \qquad (3.1.3)$$

3.2 Born-Oppenheimer approximation

The Hamiltonian operator can be written in a more compact form by adopting the atomic unit system:

$$\hat{H} = -\sum_{A}^{nuc} \frac{1}{2M_A} \nabla_A^2 - \frac{1}{2} \sum_{i}^{ele} \nabla_i^2 - \sum_{i}^{ele} \sum_{A}^{nuc} \frac{Z_A}{r_{Ai}} + \sum_{A>B}^{nuc} \frac{Z_A Z_B}{r_{AB}} + \sum_{i>j}^{ele} \frac{1}{r_{ij}} \qquad (3.2.1)$$

For further simplification, the Hamiltonian can be decomposed into individual operators:

$$\hat{H} = \widehat{T_N}(R) + \widehat{T_e}(r) + \widehat{V_{eN}}(r,R) + \widehat{V_{NN}}(R) + \widehat{V_{ee}}(r) \qquad (3.2.2)$$

where $\widehat{T_N}(R)$ and $\widehat{T_e}(r)$ are the nuclear and electronic kinetic energy operators, respectively; $\widehat{V_{eN}}(r,R)$, $\widehat{V_{NN}}(R)$, and $\widehat{V_{ee}}(r)$ are the potential energy operators for electron-electron, nucleus-nucleus, and electron-electron interactions, respectively.

The Born-Oppenheimer approximation is based on the large mass difference between nuclei and electrons, considering that nuclei are approximately three orders of magnitude more massive [49], [50]. This implies that electrons move much faster than nuclei, allowing a major simplification: *the assumption that electronic motion occurs instantaneously relative to nuclear motion.*

This approach assume that the motion of electrons and nuclei are not correlated allowing one to treat the nuclei as "fixed", while the electrons adjust to the nuclear configuration. In systems such as molecules and solids, the position of the nuclei is described by a vector ***R***, and that of the electrons by a vector ***r*** [49]. Thus, the nuclear coordinates become fixed parameters,

and the electron-nucleus potential energy depends only on ***r***. Moreover, the nuclear kinetic energy is zero since it is considered fixed and only the nuclei repulsion has to be considered. [49], [51].

With these simplifications, we obtain the electronic Hamiltonian $\widehat{H_{ele}}$, which is responsible for calculating the electronic energy of the system:

$$\hat{H}_{ele} = \hat{T}_e(r) + \hat{V}_{eN}(r;R) + \hat{V}_{NN}(R) + \hat{V}_{ee}(r) \tag{3.2.3}$$

It is worth noticing that the nucleus-nucleus potential energy operator $\widehat{V_{NN}}(R)$ it is still present in the electronic Hamiltonian. However, it is treated as a constant since, in quantum mechanics, the addition of a constant to the operator does not alter its eigenfunction, only shifts its eigenvalues [52]. The electronic energy can be calculated using the Eq. 3.2.4 as follows:

$$\hat{H}_{ele}\Psi_{ele}(\{\vec{r_i}, w_i; \vec{R}\}) = E_{ele}\Psi(\{\vec{r_i}, w_i\}; \{\vec{R}\}) \tag{3.2.4}$$

Therefore, the Ψ is a function of $\{\vec{r_i}, w_i\}$ and is parametric with respect to the $\{\vec{R}\}$.

3.3 Density Functional Theory

The main challenge in the computational treatment of multi-electron systems lies in the fact that such systems are described by many-electron wavefunction, whose high dimensionality makes calculations extremely complex. One of the most important methods for electronic structure calculations is the Hartree-Fock method, in which the wavefunction Ψ is represented as a Slater determinant [51], [53]. This determinant is an antisymmetric product of single-electron wave function:

$$\Psi = \frac{1}{\sqrt{N}}\begin{vmatrix} \chi_1(x_1) & \chi_2(x_1) & \dots & \chi_N(x_1) \\ \chi_1(x_2) & \chi_2(x_2) & \dots & \chi_N(x_2) \\ \vdots & \vdots & \ddots & \vdots \\ \chi_1(x_N) & \chi_2(x_N) & \dots & \chi_N(x_N) \end{vmatrix} \tag{3.3.1}$$

Here, the $\frac{1}{\sqrt{N}}$ term is a normalization constant, and χ represents the single-electron wavefunctions. The variables x_N denote the spatial and spin coordinates of the electrons.

However, a major limitation of the Hartree-Fock method is that it does not account electron correlation, which is crucial for accurately describing the many bodies chemical

system. To address this issue, post-Hartree-Fock methods such as perturbation theory, coupled-cluster methods, and configuration interaction have been developed [51], [54]. Although these methods offer higher accuracy, they are often computationally prohibitive for more complex systems.

In this context, Density functional Theory (DFT) emerges as an alternative approach that focuses not on the wavefunction but on the electronic density, $\rho(r)$. DFT allows the study of multi-electron systems with good accuracy while maintaining computational efficiency [55].

The electronic density is defined by equation 3.3.2, where $\Psi(r_1, r_2, \ldots, r_N)$ corresponds to the ground-state solution of the system's Hamiltonian:

$$\rho(r) = \int \ldots \int \Psi(r_1, r_2, \ldots, r_N)^* \Psi(r_1, r_2, \ldots, r_N) dr_2, \ldots, dr_N \qquad (3.3.2)$$

3.3.1 Hohenberg-Kohn Theorems

In 1964, Pierre Hohenberg and Walter Kohn established the fundamental theorems that form the modern DFT. These theorems legitimize the use of the electron density, $\rho(r)$, as a principal variable to describe any system of N particles subjected to an external potential. In the case of molecules and solids, the external potential is usually generated by the nuclei, denoted as V_{Ne}.

First Theorem: *"The external potential experienced by the electrons is a unique functional of the electronic density."* In other words, a given electronic density determines a unique external potential [56]. The proof of these theorem is provided in section 7.1 of the Appendix of this dissertation.

Second Theorem: *"The ground-state energy $E_0[\rho(r)]$ is minimized by the exact electronic density $\rho(r)$"*. That is, any approximated density that yields the correct number of electrons and originated from an external potential will always give an energy equal to or higher than the true ground-state energy [56].

According to the second theorem, the ground-state density is denoted by ρ_0, and there exists a wavefunction Ψ_0 that yields this density. However, although only one wave function describes the ground state, different wavefunction may lead to the same electron density ρ_0. Thus, the ground state-state energy is defined as:

$$E_0[\Psi] = \langle \Psi_0 | \hat{H} | \Psi_0 \rangle \leq \langle \Psi_{\rho_0} | \hat{H} | \Psi_{\rho_0} \rangle \tag{3.3.3}$$

The Hamiltonian operator $\hat{H}$ can be decomposed into three components: the kinetic energy of the electrons ($\widehat{T_e}$), the electron-electron Coulomb repulsion (V_{ee}), and the external potential, which varies depending on the system. By the first Hohenberg-Kohn theorem, the external potential is a functional of the electronic density. Using the variational principal, the Hamiltonian applied to different wavefunctions can be written as:

$$\langle \Psi_0 | \widehat{T_e} + \hat{V}_{ee} | \Psi_0 \rangle + \int V_{Ne} \rho_0 dr \leq \langle \Psi_{\rho_0} | \widehat{T_e} + \hat{V}_{ee} | \Psi_{\rho_0} \rangle + \int V_{Ne} \rho_0 dr \tag{3.3.4}$$

From this expression, we conclude that among all wavefunctions that yield the ground state electronic density ρ_0, the wavefunction Ψ_0 minimizes the expectations value $\langle \Psi_0 | \widehat{T_e} + \widehat{V_{ee}} | \Psi_0 \rangle$. This value, expressed as a functional, is known as the universal Hohenberg-Kohn functional $F_{HK}[\rho_0]$, given by:

$$F_{HK}[\rho_0] = \langle \Psi_0 | \widehat{T_e} + \hat{V}_{ee} | \Psi_0 \rangle \tag{3.3.5}$$

or, equivalently:

$$F_{HK} = min_{\Psi} \langle \Psi | \widehat{T_e} + \hat{V}_{ee} | \Psi \rangle \tag{3.3.6}$$

The term “universal” indicates that, for a given external potential, the functional $F_{HK}[\rho_0]$ depends only on the electronic density ρ_0, not on the potential itself. Thus, the total energy can be divided into two contributions: one independent of the system’s structure (external potential), $F_{HK}[\rho_0]$, and one that depends on the external potential, $\int V_{Ne} \rho_0 dr$.

The ground-state energy can be expressed as a two-step minimization problem. First, the electronic density that minimizes the energy is determined. Then, for this density, the corresponding ground-state wavefunction that produces it is found. This process can be expressed as:

$$E_0 = min_{\rho} \left[min_{\Psi} \{ \langle \Psi_0 | \hat{T} + \hat{V}_{ee} | \Psi_0 \rangle \} + \int V_{Ne} \rho dr \right] \tag{3.3.7}$$

or, in simplified form:

$$E_0 = min_{\rho} \left[F_{HK}[\rho] + \int V_{Ne} \rho dr \right] \tag{3.3.8}$$

The universal functional F_{HK} is valid for all types of systems. However, despite appearing to offer an ideal solution for many problems, its exact form remains unknown. To date, no analytical expression for F_{HK} has been proposed. In practice, F_{HK} is difficult to approximate, which poses a significant challenge to its application [56], [57], [58].

3.4 Kohn-Sham Formalism (KS-DFT)

In 1965, Walter Kohn and Lu Sham developed a formalism that made the practical implementation of Density Functional Theory (DFT) in computational codes possible. As discussed in section 3.3, the main challenge of DFT lies in the absence of an exact expression for the universal functional F_{HK}. In principle, this functional can be decomposed into three components: the kinetic energy functional $T[\rho]$, the electron-nucleus attraction functional $E_{eN}[\rho]$, and the electron-electron interaction energy $E_{ee}[\rho]$:

$$F_{HK}[\rho] = T[\rho] + E_{ee}[\rho] + E_{eN}[\rho] \tag{3.4.1}$$

One of the key difficulties in formulating DFT precisely is the lack of an exact expression for the kinetic energy functional. Unlike Thomas-Fermi model, which assumes a homogeneous electron gas, the kinetic energy in a real system must account for the correlation between multiples charged particles. Furthermore, another challenge is the absence of an exact formulation for the electron-electron interaction energy functional, which includes both Hartree energy and the exchange energy. The latter is essential for accurately capturing quantum effects in the system's potential energy, yet its exact expression remains unknown [57], [59]. Furthermore, providing an approximate $\rho(r)$ is not trivial, because it has to represent an electronic system. The difficult to propose $\rho(r)$ that satisfy the N-representability, that is, a well-behaved function that goes to zero in the infinity and integrates to the number of electrons is much simpler, but that represent an electronic system subject to an external potential is much more complex and remains up to date an open question.

Kohn and Sham proposed a solution to these limitations by calculating the kinetic energy assuming that the electron density arises from a single Slater determinant wavefunction, as in the restricted-Hartree-Fock method. This approach, known as KS-DFT (Kohn-Sham Density Functional Theory), has become the most widely used framework for theoretical calculations [57], [59].

The central idea of the Kohn-Sham formalism is to replace the real system of interacting electrons with a fictious system of non-interacting electrons that reproduces the same electrons density. Instead of working directly with the exact density, the model employs non-interacting orbitals, from which the electron density can be reconstructed in a tractable way:

$$\rho(r) = \sum_{i=1}^{N} |\phi_i(r_i)|^2 \tag{3.4.2}$$

The kinetic energy of these orbitals is defined as:

$$\hat{T}_S[\rho] = \sum_{i=1}^{N} \langle \phi_i(r_i) \left| -\frac{1}{2}\nabla_i^2 \right| \phi_i(r_i) \rangle \tag{3.4.3}$$

Accordingly, the total energy in the Kohn-Sham approach is expressed as:

$$E_{KS-DFT}[\rho] = T_S[\rho] + E_{eN}[\rho] + J[\rho] + E_{xc}[\rho] \tag{3.4.4}$$

Here, $T_S[\rho]$ is the kinetic energy functional of the non-interacting system, $J[\rho]$ is the classical Hartree repulsion term, $E_{eN}[\rho]$ is the potential energy of electron-external potential interaction, and $E_{xc}[\rho]$ is the exchange-correlation energy functional, which includes the errors in both kinetic and electron-electron interaction energies:

$$J[\rho] = \frac{1}{2}\iint \frac{\rho(r)\rho(r')}{|r-r'|} dr dr' \tag{3.4.5}$$

$$E_{xc}[\rho] = (\hat{T}[\rho] - \hat{T}_S[\rho]) + (E_{ee}[\rho] - J[\rho]) \tag{3.4.6}$$

The main advantage of KS-DFT is that it enables accurate calculation of all energy contributions except the $E_{xc}[\rho]$, making the approximation of this term the central challenge of the methodology. Assuming that $E_{KS-DFT}[\rho]$ is differentiable, the variational principle leads to a minimization subject to the constraint $\int \rho(r)dr = N$, where N is the number of electrons. To determine the orbitals that minimize $G[\rho]$, one takes the variation of the functional with respect to ${\phi_i}^*(r_i)$. Thus, the minimization condition is given by:

$$\frac{\delta G[\rho]}{\delta {\phi_i}^*(r_i)} = \frac{\delta\{E_{KS-DFT}[\rho] - \varepsilon_i[\int \rho(r)dr - N]\}}{\delta {\phi_i}^*(r_i)} = 0 \tag{3.4.7}$$

The individual minimization of each term in the functional $G[\rho]$ yields the following expressions:

1) <u>Kinetic term:</u>

$$\frac{\delta}{\delta {\phi_i}^*}\left(\sum_{i=1}^{N} -\frac{1}{2}\int {\phi_i}^* \nabla_i^2 \phi_i dr_i\right) = -\frac{1}{2}\sum_{i=1}^{N} \nabla_i^2 \phi_i \tag{3.4.8}$$

2) <u>External potential term:</u>

$$\frac{\delta}{\delta {\phi_i}^*}\left(\sum_{i=1}^{N} V_{Ne}\int {\phi_i}^* \phi_i \, dr_i\right) = \sum_{i=1}^{N} V_{Ne}\phi_i \tag{3.4.9}$$

3) <u>Hartree term:</u>

$$\frac{\delta}{\delta {\phi_i}^*}\left(\frac{1}{2}\sum_{i=1}^{N}\iint \frac{{\phi_i}^*\phi_i\rho(r')}{|r-r'|} dr dr'\right) = \sum_{i=1}^{N}\int \frac{\rho(r')}{|r-r'|} dr' \phi_i \; = \sum_{i=1}^{N} V_H \phi_i \tag{3.4.10}$$

4) <u>Exchange-correlation term:</u>

$$\frac{\delta E_{xc}}{\delta \phi_i{}^*} = \sum_{i=1}^{N} V_{xc}\phi_i \tag{3.4.11}$$

5) Constraint term:

$$\frac{\delta}{\delta \phi_i{}^*}\left(\epsilon_i\left[\int \rho(r)dr - N\right]\right) = \sum_{i=1}^{N} \varepsilon_i \phi_i \tag{3.4.12}$$

Substituting all these terms into the minimized functional leads to a Schrödinger equation that defines the energy of each orbital ϕ_i:

$$\sum_{i=1}^{N}\left(-\frac{1}{2}\nabla_i^2 + V_{eN} + V_H + V_{xc}\right)\phi_i(r_i) = \sum_{i=1}^{N}\left(-\frac{1}{2}\nabla^2 + V_{eff}(r)\right) = \sum_{i=1}^{N} \varepsilon_i \phi_i(r_i) \tag{3.4.13}$$

The terms $V_{eN} + V_H + V_{xc}$ define the Kohn-Sham effective potential, $V_{eff}(\vec{r})$, and the eigenvalue ε_i are known as Kohn-Sham eigenvalues, while the non-interacting orbitals ϕ_i are referred to as Kohn-Sham orbitals. It is important to observe that as written the $V_{eff}(\vec{r})$ is a local potential since depends only on the $\vec{r}$, therefore it cannot represent interacting electrons, otherwise, it would be nonlocal potential.

3.5 Solutions of the Kohn-Sham Equations

The minimizations presented in sections 3.4 lead to a set of N equations analogues to the Hartree-Fock equation, known as the Kohn-Sham equations. As in the Hartree-Fock method, these equations must be solved self-consistently, ensuring that the Kohn-Sham orbital ϕ_i reproduces the ground-state electron density according to equation 3.4.2.

To guarantee the antisymmetric of the wavefunction, the Kohn-Sham orbitals must be arranged in a Slater determinant, resulting in the Kohn-Sham wavefunction Ψ_{KS}:

$$\Psi_{KS}(r_1, r_2, \ldots, r_N) = \frac{1}{\sqrt{N}} det(\phi_1(r_1) \ldots \phi_N(r_N)) \tag{3.5.1}$$

The Kohn-Sham equations must be solved self-consistently because the Hartree energy, exchange-correlation potential, and external potential all depend on the electron density, which in tur depend on the Kohn-Sham orbitals, themselves determined by the effective potential. To address this interdependence, the process begins with the initial guess for the electron density. Next, the Hartree potential is calculated, and the Kohn-Sham effective potential is determined.

Using this potential, the Kohn-Sham equations are solved to obtain the orbitals, allowing the construction of a new electron density through equation 3.4.2. This procedure is repeated interactively, comparing the electron densities and the energy values from each step until a convergence criterion is satisfied. This procedure is known as Self-Consistent-Field (SCF) method [57], [59]. Figure 5 illustrates a schematic representation of this process.

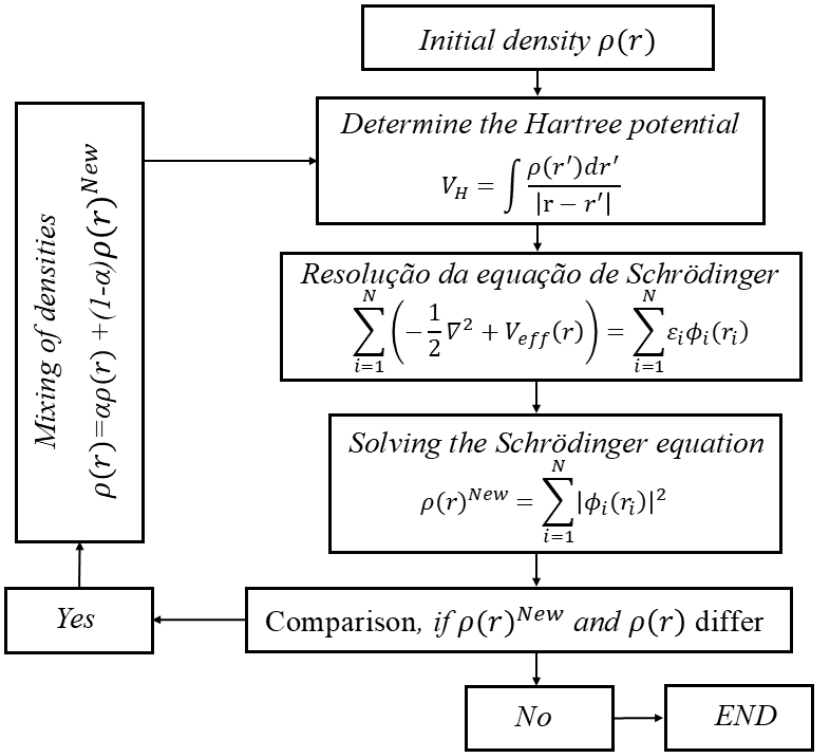

Figure 5: Flowchart of the Kohn-Sham DFT procedure.

During the self-consistent procedure, if the convergence is not achieved, a new SCF cycle is initiated. To avoid numerical instability, the new electron density $\rho(r)^{New}$ is mixed with the previous one using a weighted average, generating an updated density for the new cycle [52], [60].

3.6 Exchange-Correlation Potential

In KS-DFT, all terms in the functional $E_{KS-DFT}[\rho]$ can be explicitly calculated, except for the exchange-correlation term. Although DFT is, in principle, exact, the need for approximations to this functional makes KS-DFT an approximate approach. The exchange-

correlation functional can be decomposed into two distinct contributions: exchange and correlation:

$$E_{xc}[\rho] = E_x[\rho] + E_c[\rho] \quad (3.6.1)$$

The Exchange energy $E_x[\rho]$ arise from the Pauli exclusion principle, which imposes antisymmetry of the wavefunction for fermions under the exchange of two particles. On the other hand, the correlation energy $E_c[\rho]$ accounts for additional electrons interactions effects beyond exchange.

The simplest approximations for the exchange-correlation functional is the *Local Density Approximation* (LDA), in which the exchange-correlation functional expression was obtained using the results of a gas of electrons. Then, this expression is used locally obtained the E_{xc} for each $\delta\vec{r}$ and integrated for all space.

Although LDA was the first approximation used, it has limitations in many chemical applications, typically overestimating binding energies by approximately 30 kcal/mol. Nevertheless, it has proven effective in systems where exchange and correlation effects are predominantly short-range, such as metallic solids, whose properties closely resemble those of the homogeneous electron gas [61].

A significant improvement came with the Generalized Gradient Approximation (GGA) functionals, which incorporate not only the electron density but also its spatial gradient – the rate at which the density changes in space. This adds more information to the functional and subsequently reduces errors in the dissociation energies while improving the description of energy barriers for the transition states. The GGA functional is a class of XC functional that uses the gradient and reinforce many of the XC functional properties that are known such as scaling properties. The class of GGA functionals that do not use any empirical parameters can be still considered as an ab initio or first principle calculations. The most important are the PBE e PW91. Some other use empirical parameters such as BLYP, BP86 and P86P86, which kept some empirical parameters fitted by experimental data, while remaining some of the properties of the XC functionals. We should say that the arising of the GGA XC functionals in 1986 with the first GGA functional proposed by Perdew lead the DFT to the chemistry field.

Another widely used class is the hybrid functionals, which the exchange term is a linear combination of the exact exchange from Hartree-Fock theory and the GGA exchange functional, added by the GGA correlation functionals. The hybrid functionals such as B3LYP much improved the results for organic molecules but bring into the DFT some of the limitations of the Hartree-Fock such as the bias to favor higher multiplicities and the spin contamination

for open shell systems. Therefore, hybrid methods find the treatment of the transition metal complexes its most challenging systems [61].

3.7 Periodic Systems

The periodic arrangement of atoms in a crystal is mathematically described by the smallest repeating unit of the system, known as unit cell, which is associated with a lattice of points that remain invariant under translational operations. These points can be located in space using vectors defined by equation 3.7.1.1:

$$R = n_1 a_1 + n_2 a_2 + n_3 a_3 \tag{3.7.1.1}$$

where n_1, n_2, and n_3 are integers (positive or negative), and e a_1, a_2 and a_3 are the primitive vectors that define the unit cell, and consequently, the volume of the cell Ω [62]. Each unit cell may contain one or more atoms, whose specific arrangement is referred to as basis.

In solid-state physics, a fundamental concept is the reciprocal lattice, a mathematical construction that reflects the periodicity of the crystal in reciprocal space. Just like real-space lattice, the reciprocal lattice is also defined by a unit cell composed of three vectors. In this context, however, the unit cell is referred to as the First Brillouin zone [62], [63].

Analogous to vector **R**, which describes the position of lattice points in real space, a vector **G** can be defined for the reciprocal lattice. This vector represents points that are invariant under translational within the first Brillouin zone and is defined by equation 3.7.1.2:

$$G = m_1 b_1 + m_2 b_2 + m_3 b_3 \tag{3.7.1.2}$$

where m_1, m_2, and m_3 are integer (positive or negative), and b_1, b_2 and b_3 are the primitive vectors of the reciprocal lattice. According to Ashcroft and Mermin [64], the vectors are derived from the primitive vectors in the real-space lattice (a_1, a_2, and a_3), using the following expressions:

$$b_1 = \frac{2\pi(a_2 \times a_3)}{a_1(a_2 \times a_3)} \quad b_2 = \frac{2\pi(a_3 \times a_1)}{a_2(a_3 \times a_1)} \quad b_3 = \frac{2\pi(a_1 \times a_2)}{a_3(a_1 \times a_2)} \tag{3.7.1.3}$$

The dot product between **R** and **G** results in $R.G = 2\pi l$, where l is an integer given by $l = n_1 m_1 + n_2 m_2 + n_3 m_3$. This relationship implies that the function e^{iGR} is always equal to 1, that is:

$$e^{iGR} = 1 \tag{3.7.1.4}$$

This property is essential for describing the periodicity and symmetry of electronic states in crystalline solids [62], [63], [65].

3.8 Bloch's Theorem

Bloch's theorem state that: "The eigenstate $\Psi_{nk}(r)$ of the Hamiltonian associated with a periodic potential $U(r) = U(r + R)$, where **R** is any Bravais lattice vector, can be written as a plane wave multiplied by a function with the same periodicity as the Bravais lattice $(u_{nk}(r))$ [49], [62]." This property is mathematically expressed by equation 3.8.1:

$$\Psi_{nk}(r) = e^{ikr}u_{nk}(r) \tag{3.8.1}$$

To constructively demonstrate Bloch's theorem as described in the book by Ashcroft and Mermin [64], we start with the application of Fourier series theory. Periodic boundary conditions, known as Born-von Karman boundary conditions, are imposed. These assume that the crystal is large enough for edge effects to be negligible. Thus, the wavefunction must also be periodic and can be expanded as a Fourier series [62], represented by equation 3.8.2:

$$\Psi(r) = \sum_{q} C_q e^{iqr} \tag{3.8.2}$$

The effective potential within the unit cell is also periodic and can likewise be expanded in a Fourier series using reciprocal lattice vectors, as shown in equation 3.8.3:

$$U(r) = \sum_{G} U_G e^{iGr} \; onde \;\; U_G = \frac{1}{v}\int dr e^{-iGr}U(r) \tag{3.8.3}$$

Here, U_G is the Fourier coefficients obtained by integrating the potential over the volume V of the unit cell [60], [62], [64].

By inserting the proposed wavefunction $\Psi(r)$ and the potential $U(r)$ into the time-independent Schrödinger equation:

$$\left[-\frac{\hbar^2}{2m}\nabla^2 + \; U(r)\right]\Psi(r) \; = \varepsilon\Psi(r) \tag{3.8.4}$$

By substituting their respective Fourier series forms, the result is obtained:

$$\left(-\frac{\hbar^2}{2m}\nabla^2 + \sum_G U_G e^{iGr}\right)\sum_q C_q e^{iqr} = \varepsilon \sum_q C_q e^{iqr} \tag{3.8.5}$$

Applying the operator and rearranging terms gives:

$$\sum_q \left(-\frac{\mathrm{q}^2\hbar^2}{2m} - \varepsilon\right) C_q e^{iqr} + \sum_{G,q} U_G C_q e^{i(G+q)r} = 0 \tag{3.8.6}$$

Now, redefining $q' = q + G$, and using the fact that the sums over q and q' span the same wavevector space, we combine the sums as:

$$\sum_q \left\{\left(-\frac{\mathrm{q}^2\hbar^2}{2m} - \varepsilon\right) C_q + \sum_G U_G C_{q-G}\right\} e^{iqr} = 0 \tag{3.8.7}$$

Since plane waves, e^{iqr}, are linearly independent, the coefficient must vanish individually:

$$\left(-\frac{\mathrm{q}^2\hbar^2}{2m} - \varepsilon\right) C_q + \sum_G U_G C_{q-G} = 0 \tag{3.8.8}$$

This result is a system of equations that can be used to determine the coefficients C_q for the wavefunction expansion. Rather than solving the Schrödinger equation directly, the problem is reduced to solving this linear system.

Now, we redefine $q = k + G'$, where G' is a reciprocal lattice vector and k lies within the first Brillouin zone. The equation becomes:

$$\left(-\frac{|k - G'|^2\hbar^2}{2m} - \varepsilon\right) C_{k-G'} + \sum_G U_G C_{k-G'-G} = 0 \tag{3.8.9}$$

Equation 3.8.9 shows that, for a fixed k in the first Brillouin zone, only the coefficient C_k, C_{k-G}, $C_{k-G'}$, etc., are coupled – that is, the coefficients associated with plane waves whose wavevector differ from k by a reciprocal lattice vector.

The original problem of determining the wavefunction expansion coefficients is thus transformed into independent problems, each corresponding to a single allowed value of k in the first Brillouin zone.

This construction provides a constructive proof of Bloch's theorem. By rewriting the wavevector as $\mathrm{k}, \mathrm{k} + \mathrm{G}', \mathrm{k} + \mathrm{G}'', \ldots$, the wavefunction can be expressed as:

$$\Psi_k(r) = \sum_G C_{k-G} e^{i(k-G)r} \quad \rightarrow \quad \Psi_k(r) = e^{ikr}\left(\sum_G C_{k-G} e^{-iGr}\right) \tag{3.8.10}$$

The function $\Psi_k(r)$ in equation 3.8.10 is exactly of the Bloch form in equation 3.8.1, with the term $\sum_G C_{k-G} e^{iGr}$ identified as the periodic part $u_{nk}(r)$. To verify its periodicity, we apply translation by a Bravais lattice vector R:

$$u_{nk}(r+R) = \left(\sum_G C_{k-G} e^{-iG(r+R)}\right) = e^{iGR}\left(\sum_G C_{k-G} e^{-iGr}\right) \tag{3.8.11}$$

Since $e^{iGR} = 1$ for all reciprocal lattice vectors G and direct lattice vectors R, we find:

$$u_{nk}(r+R) = u_{nk}(r) \tag{3.8.12}$$

Therefore, the solution of Schrödinger equation with periodic potential – also called the Bloch function – is given by a plane wave multiplied by a periodic function.

3.8.1 Consequences of Bloch's Theorem

Bloch's theorem introduces the concept of the wavevector k. Unlike the wavevector k in the Thomas-Fermi model, which is directly related to the momentum of free particles, in the context of Bloch's theorem k acts as a quantum number that labels the electronic states.

The wavevector k can always be restricted to the first Brillouin zone due to the periodicity of the Bloch function in the reciprocal space. This implies that states differing by a reciprocal lattice vector represent the same physical state.

Another important consequence is the emerging of energy levels. This energy levels can be derived by inserting the Bloch wavefunction into the Schrödinger equation:

$$\left(-\frac{\hbar^2}{2m}\nabla^2 + U(r)\right) e^{ikr} u_{nk}(r) = \varepsilon e^{ikr} u_{nk}(r) \tag{3.8.1.1}$$

Applying the operator:

$$\begin{aligned} -\frac{\hbar^2}{2m}\left(-\mathrm{k}^2 e^{ikr} u_{nk}(r) + e^{ikr}\nabla^2 u_{nk}(r) + 2ik\nabla u_{nk}(r) e^{ikr}\right) \\ + U(r)\left(e^{ikr} u_{nk}(r)\right) = \varepsilon e^{ikr} u_{nk}(r) \end{aligned} \tag{3.8.1.2}$$

Factoring out the common exponential e^{ikr}:

$$\begin{aligned} e^{ikr}\left(-\frac{\hbar^2}{2m}(-\mathrm{k}^2 u_{nk}(r) + \nabla^2 u_{nk}(r) + 2ik\nabla u_{nk}(r)) + U(r)(u_{nk}(r))\right) \\ = \varepsilon e^{ikr} u_{nk}(r) \end{aligned} \tag{3.8.1.3}$$

Rewriting the operator in perfect square form, we find that the periodic part ($u_{nk}(r)$) satisfies:

$$\left(\frac{\hbar^2}{2m}\left(\frac{\nabla}{i} + \mathrm{k}\right)^2 + U(r)\right) u_{nk}(r) = \varepsilon u_{nk}(r) \tag{3.8.1.4}$$

Now, expanding $u_{nk}(r)$ as a Fourier series (as in equation 3.8.11):

$$\left(\frac{\hbar^2}{2m}|k+G|^2+U(r)\right)\sum_G C_{k,n}(G)e^{-iGr}=\varepsilon_{n,k}\sum_G C_{k,n}(G)e^{-iGr} \qquad (3.8.1.5)$$

Thus, the periodic function $u_{nk}(r)$ satisfies an eigenvalue equation similar to the Schrödinger equation, yielding discrete eigenvalue $\varepsilon_{nk}(r)$, with the periodic boundary condition $u_{nk}(r)=u_{nk}(r+R)$.

This periodicity confines the problem to the primate cell, effectively turning it into a quantum confined problem, naturally leading to a discrete energy spectrum – hence the quantum number *n*.

The wavevector k appears as a continuous parameter. Therefore, the eigenvalues ε_{nk} vary continuously with k, forming the so-called energy bands. For each n, the function $\varepsilon_n(k)$ defines a distinct energy band in the solid.

3.8.2 Plane-wave Expansion Method

The plane-wave expansion method consists of expressing the electronic wavefunction as a linear combination of basis function of the form e^{iGr}, where G are reciprocal lattice vectors. This approach is especially well-suited for periodic systems. Equation 3.8.1.5 represents the Schrödinger equation in matrix form within the plane-wave basis.

The number of plane waves used in the expansion determines the number of orbitals included in the calculation and is controlled by a parameter called the cutoff energy E_{cutoff}, which defines the maximum kinetic energy allowed for the states considered:

$$E_{cutoff}=\frac{\hbar^2}{2m_e}G_{cutoff}^2 \quad onde \quad G_{cutoff}>|G+k| \qquad (3.8.2.1)$$

Choosing an appropriate E_{cutoff} is essential for achieving a good balance between accuracy and computational cost. Convergence tests are usually performed to check the stability of the total energy of the system with respect to different values of E_{cutoff}.

Additionally, core orbitals exhibit highly oscillatory behavior, especially near the nucleus, requiring a large number of plane waves for accurate description. To address this, the

concept of pseudopotential is employed. These pseudopotentials replace the true nuclear potential with a smoothed version, allowing only valence electrons to be treated explicitly.

3.9 Pseudopotential

The Physical and chemical properties of materials and molecules are primarily determined by the valence electrons of the constituent atoms. Core electrons, in contrast, remain largely unaffected during chemical bonding and are typically inert in solid-state and molecular systems. Additionally, their wavefunctions are highly oscillatory near the nucleus, making them computationally expensive to describe using plane waves [62].

To address this challenge, the pseudopotential method was developed. This approach removes the core electrons from the calculations and replaces the true all-electron potential with a smoother pseudopotential that acts only on the valence electrons. Since the core electrons experience a much stronger coulomb attraction due to their proximity to the nucleus, they do not actively participate in the bonding, making this approximation both reasonable and efficient.

Figure 6 illustrates the concept behind the method by comparing the true valence wavefunction with its corresponding pseudo wavefunction. Near the nucleus, the true wavefunction becomes complex and sharply varying, making it difficult to represent numerically. The pseudopotential replaces this complex behavior with a smooth pseudopotential that is easier to handle, while still matching the true wavefunction beyond a certain cutoff radius (r_c).

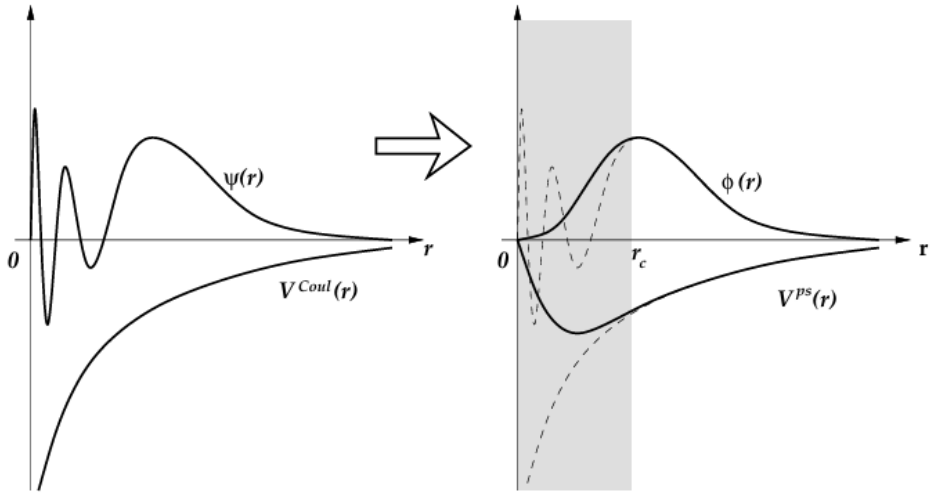

Figure 6: Schematic representation of a real function $\Psi(r)$ with Coulomb potential $V^{coul}(r)$ on the left, and its pseudo wavefunction $\phi(r)$ with pseudopotential $V^{ps}(r)$ on the right [62].

Pseudopotentials are constructed through self-consistent calculations for each element of interest. For each valence state, the radial wavefunction is calculated, and a cutoff radius (r_c) is chosen. Inside this radius, the true potential is replaced with a smoother version, while outside

it, the pseudopotential and pseudo wavefunction matches the real one. This effectively "freezes" the core orbitals, which are assumed to remain unchanged during bonding [66].

One of the most commonly used types of pseudopotentials is the ultrasoft pseudopotential [66]. This method allows the wavefunction to be even smother near the nucleus, which reduces the number of plane waves needed in the calculation. As a result, the simulations become faster and less computationally expensive, while still providing accurate results for the electronic structure.

3.10 Bader Theory: Quantum Theory of Atoms in molecules (QTAIM)

The Quantum Theory of Atoms in Molecules (QTAIM), developed by Richard Bader, provides a rigorous framework for topological analysis of the electron density obtained through Kohn-Sham Density Functional Theory (KS-DFT). This theory allows for the integration of the electronic density associated with a given atom within a molecule or crystalline structure, offering a quantitative description of local electronic properties [67].

The distribution of electronic density in a molecule or solid is shaped by the attractive forces exerted by the nuclei, which influences its spatial arrangement. Most of the electronic density tends to concentrate near the nuclei, and the boundaries defining individual atoms emerge from the balance of attractive forces exerted by neighboring nuclei [67], [68].

Within the QTAIM formalism, so-called *critical points* of the electronic density are defined as regions in space where the gradient of electronic density is zero – where the first derivative of the density vanishes. There are four main types of critical points, nuclear critical points (NCP), bond critical points (BCP), ring critical points (RCP), and cage critical points (CCP). These points play a key role in defining the electronic topology of the system [68], [69].

The spatial division between atoms is determined by surfaces known as *zero-flux surfaces*, which delineate regions referred to as *atomic basins*. On these zero-flux surfaces, the gradient vector of the electronic density is perpendicular to the surface normal vector, such that their dot products are zero:

$$\nabla\rho(r) \cdot \hat{n}(r) = 0 \qquad (3.10.1)$$

Equation 3.10.1 mathematically defines the boundaries of atomic basins, each of which contains a nucleus and its associated electronic density. The total number of electrons assigned to an atom can be obtained by integrating the density within its respective basin:

$$N(\Omega) = e \int \rho(r)\, dr \tag{3.10.2}$$

where $N(\Omega)$ represents the electronic charge in the basin Ω, $\rho(r)$ is the electronic density, and e is the elementary charge.

When two atomic basins are separated by a zero-flux surface, the corresponding nuclei are connected by a gradient path of the electronic density. This path is associated with the presence of a chemical bond between atoms and contains a saddle-type critical point known as a *bond critical point* (BCP). The presence of a BCP indicates a region of electron density accumulation between the atoms and is interpreted as evidence of chemical bond formation [67], [68].

3.11 Electron Localization Function (ELF)

The Electron Localization Function (ELF) is a theoretical tool that enables the visualization of regions with high electron concentration in molecules and solids, providing a detailed interpretation of the nature of chemical bonding. When used in combination with QTAIM, ELF offers a powerful approach for characterizing the electronic distribution and the nature of chemical interactions in different systems [70].

ELF is a dimensionless quantity that compares the real kinetic energy density of electrons to that of a homogeneous electron gas:

$$ELF = \frac{1}{1 + \chi^2(r)} \quad onde\ \chi(r) \quad = \frac{t(r)}{t_h(r)} \tag{3.11.1}$$

In equation 3.11.1, $t(r)$ represents the real kinetic energy density of electrons at a given point *r*, while $t_h(r)$ corresponds to the kinetic energy density of a homogeneous electron gas with the same local electron density [70], [71] given by the equations:

$$t(r) = -\frac{1}{2}\nabla^2 \tag{3.11.2}$$

$$t_h(r) = \frac{3}{10}(3\pi^2)^{\frac{2}{3}}\rho(\boldsymbol{r})^{\frac{5}{4}} \tag{3.11.3}$$

The comparison between $t(r)$ and $t_h(r)$ is fundamental for understanding the nature of the electronic distribution. When $t(r)$ is significantly lower than $t_h(r)$, electrons are more efficiently organized than in homogeneous gas, forming well-defined regions of electrons accumulation. This behavior is characteristic of covalent bonds and strongly localized electron pairs. On the other hand, when $t(r)$ and $t_h(r)$ are comparable, the electronic distribution resembles that of the homogeneous electron gas, as seen in free electrons in metals of in regions with weak bond interactions [70], [72].

In this context, ELF values provide a direct interpretation of the degree of the electron localization. High ELF values (close to 1) indicate strong electron localization, such as in covalent bonds, lone pairs, or regions near atomic nuclei. Low ELF values (close to 0) indicate areas of significant electron delocalization or negligible density such as in regions with weak electronic interactions. When ELF is close to 0.5, this suggests that $t(r) \approx t_h(r)$, indicating a diffuse electronic behavior similar to that of a homogeneous electron gas such as in metallic systems.[70], [71], [72].

Thus, ELF not only helps in identifying and characterizing chemical bonds but also offers a detailed view of the spatial arrangement of electrons, making it an essential tool for studying electronic properties in both molecular and solid-state systems.

3.12 Density of States and Band structure

An effective way to assess the electronic properties of a material is through the study of the electronic density of states (DOS). The DOS represents the number of available electronic states within an energy range between $E\ e\ E + dE$ [62], [63], [64]. As discussed in section 3.8 of this dissertation, in crystalline systems, the electronic states are characterized by the quantum numbers *k* and *n*, which determine their respective energies. Therefore, all states within a given energy range contribute to the density of states in that region.

Once the electronic density and the wavefunction have been obtained through the Kohn-Sham formalism, it becomes possible to calculate the band structure, which describes how the electronic energies vary as a function of the wave vector *k* in the crystal. In crystalline materials,

electrons occupy energy levels organized into bands, and within each band, the energy varies with *k*, as shown by equation 3.8.1.5. These energies levels are organized into bands and are labeled by the quantum number *n*, which distinguishes different bands for given wave vector *k*. Thus, for each point *k* within the first Brillouin zone, several distinct electronic states may exist, each corresponding to a different value of *n* and representing a different energy level [62]. Within each band, the energy varies continuously as a function of *k*, forming the characteristic dispersion relation of the electronic structure.

The conduction band consist of unoccupied energy levels and the valence band, on the other hand, are occupied energy levels. Between these bands, there may exist a region with no accessible electronic states, known as the band gap. Material with large band gap (greater than 3 eV), such as insulators, exhibit low electrical conductivity, whereas materials with small (up to 3 eV) or nonexistent band gap are classified as semiconductors or conductors, respectively [60], [62].

The band structure is obtained by varying the wave vector *k* along a high-symmetry path in the first Brillouin zone, allowing the dispersion of electronic energies across the bands to be traced [73].

The project density of states (PDOS) is an essential tool for understanding the contribution of different atoms and orbitals to the band structure of the material. While the total DOS provides an overview of the distribution of electronic states as a function of energy, the PDOS enables the identification of which atomic orbitals dominate in specific regions of the band structure [62], [74].

Mathematically, the PDOS is obtained by projecting the electronic states Ψ_{kn} onto representative atomic orbital functions ϕ_{α}, as shown in the equation below:

$$\Psi_{kn} = \sum_{kn} \left|\langle \phi_{\alpha} | \Psi_{kn} \rangle\right|^2 \delta(\mathrm{E} - E_{kn}) \tag{3.12.1}$$

In Equation 3.12.1, $|\langle \phi_{\alpha} | \Psi_{kn} \rangle|^2$ represents the weight of the contribution of orbital ϕ_{α} to the electronic state Ψ_{kn}, ranging from 0 to 1. This value indicates the fraction of the total wavefunction described by the projected orbital.

PDOS is widely used in the analysis of the nature of electronic bands, enabling the identification of the atomic origin of the states located in the valence and conduction bands.

3.13 Computational Details

The structural, electronic, thermodynamic, and reactivity properties of troilite (FeS) and monoclinic pyrrhotite (Fe_7S_8) were investigated based on Density Functional Theory (DFT), as implemented in the Quantum ESPRESSO package (version 7.3) [75]. This software is designed for periodic systems and employs plane-waves as basis functions, with the size of the basis controlled by the wavefunction energy cutoff parameter (*ecutwfc*). For all simulations, the Generalized Gradient Approximation (GGA) was adopted, using the Perdew-Burke-Ernzerhof (PBE) exchange-correlation functional [76].

Core electrons were described by ultrasoft pseudopotentials (PBE) proposed by Vanderbilt [66], and the valence electron configurations considered were Fe $3d^6 4s^2$ and S $3s^2 3p^4$. The Brillouin zone was sampled using the Monkhorst-Pack scheme [77]. During structural optimization, k-point meshes of $1 \times 2 \times 1$ for troilite and $2 \times 4 \times 2$ for pyrrhotite were adopted. For the calculation of electronic properties, the density of the k-point mesh was doubled. The Kohn–Sham orbitals were expanded in plane waves with cutoff energies of 50 Ry for troilite and 60 Ry for pyrrhotite, ensuring total energy convergence within $10^{-3}\,Ry$. Convergence tests for the cutoff energy and k-point meshes are presented in Figures A1 and A2 of the Appendix.

Geometry optimization was performed using the BFGS algorithm, with both atomic positions and lattice parameters allowed to relax. The convergence criteria required that the maximum force on each atom be below $10^{-3}\,Ry$ eV/Å and the residual pressure below 0.5 kbar.

To better describe the localized Fe 3d electrons, the Hubbard correction was applied using an effective Hubbard term ($U_{eff} = U - J$), with values of 1 eV for monoclinic pyrrhotite and 2 eV for troilite. These corrections were applied uniformly to all Fe atoms in each structure [78], [79], [80]. The influence of different U values is illustrated in Table A1 of the Appendix.

The thermodynamic properties associated with iron vacancy formation were evaluated for both materials. For troilite, phonon calculations were performed using a q-point mesh of $2 \times 4 \times 2$, a cutoff energy of 50 Ry, and a self-consistent field (SCF) convergence threshold of 10^{-10} Ry. For monoclinic pyrrhotite, the calculations employed a q-point mesh of $1 \times 1 \times 1$, the same cutoff energy of 50 Ry, and an identical SCF convergence threshold. The resulting vibrational density of states was used to compute interatomic force constants and derive

thermodynamic quantities such as vibrational energy, free energy, and entropy via the quasi-harmonic approximation [81].

For the vacancy calculations in troilite, a 48-atom supercell ($Fe_{24}S_{24}$) was constructed by duplicating the conventional unit cell, which contains 12 iron and 12 sulfur atoms, as illustrated in Figure 7. Iron vacancies were introduced according to the general formula $Fe_{24-n}S_{24}$, where *n* represents the number of iron atoms removed.

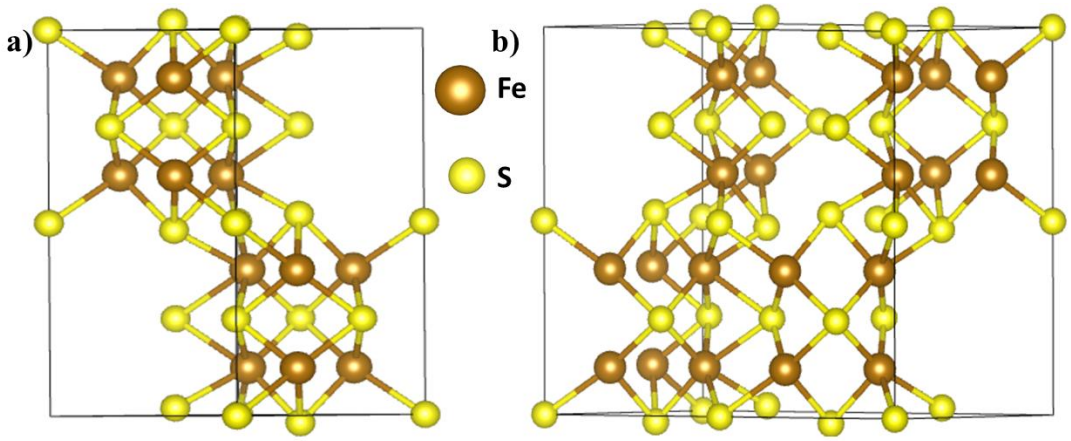

Figure 7: Unit cell of troilite (a) (FeS) and 1x2 supercell (b) ($Fe_{24}S_{24}$) used for Fe vacancy calculations in FeS structure. Sulfur atoms are in yellow and iron atoms are in brown.

In the case of monoclinic pyrrhotite, which naturally presents iron vacancies, the vacant sites were initially filled to create a reference structure ($Fe_{32}S_{32}$). The vacancies were then introduced by removing the same iron atoms that had been added, reproducing the original stoichiometry of monoclinic pyrrhotite with formula $Fe_{28}S_{32}$. The crystal structure used to perform the thermodynamic analysis is shown in Figure 8.

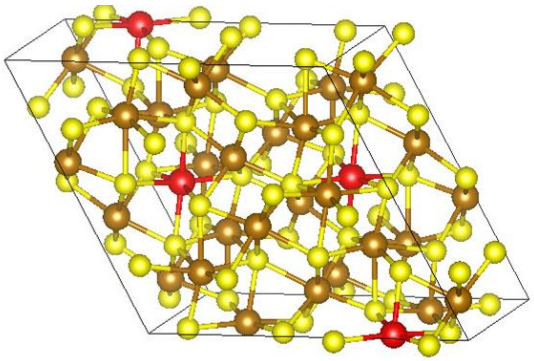

Figure 8: Unit cell of stoichiometric monoclinic pyrrhotite ($Fe_{32}S_{32}$). Red spheres indicate the iron atoms added to complete the structure.

Further details on the thermodynamic equations used to calculate vacancy formation energies are presented and discussed in Chapter 4.

The oxidation process of monoclinic pyrrhotite was investigated using a surface (slab) model composed of six atomic layers. The surface was oriented parallel to the *xy*-plane, with a

vacuum region of 10 Å introduced along the *z*-direction to prevent spurious interactions between periodic images. All slab models were constructed from the optimized (1×1) bulk structure of monoclinic pyrrhotite.

Because pyrrhotite has no natural cleavage plane, surfaces derived from the (001), (010), and (100) directions were evaluated. Their relative stability was assessed in two stages. First, the energy required to create each ideal (unrelaxed) surface was determined. Second, the additional stabilization gained after atomic relaxation was calculated. The surface with the lowest combined energy was selected for the adsorption study. The precise expressions used in these steps, together with the numerical results, are provided in Chapter 5.

Oxygen adsorption was then examined on the optimized surface. Adsorption energies were obtained within the same theoretical framework adopted for the bulk and surface calculations; the exact formulae and computational details appear in Chapter 5, where the oxidation mechanism is discussed in full.

All atomic structures and charge-density maps were visualized with VESTA (Visualization for Electronic and Structural Analysis).

4 VACANCY FORMATION[1]

4.1 Vacancy Formation Energy

After optimizing the crystalline structure and establishing the computational protocol for an accurate structural description, the study proceeded to investigate the formation of iron vacancies in troilite structure.

The formation of defects in troilite is challenging to analyze due to the extreme environmental conditions under which these phenomena typically occur [82], [83]. To investigate the thermodynamic process, we followed the methodology proposed by Oliveira et al. [84], which involves multiples computational steps. Initially, single-point calculations were carried out for the removal of one iron atom from each nonequivalent site; second, the most stable structure was identified to perform full geometry and lattice optimization and to calculate thermodynamic properties; third, calculations were conducted for the removal of the second iron atom from the remaining nonequivalent sites, and again the most stable structure was fully optimized and used to determine thermodynamic properties. Throughout the dissertation, the optimized structures containing one to six iron vacancies are referred to here as Vac1, Vac2, Vac3, Vac4, Vac5, and Vac6. The total electronic energies corresponding to all tested configurations are presented at Figure A3 of the Appendix.

The vacancy formation energy for the most stable configuration was calculated using equation 4.1.1:

$$E^{vac} = \frac{(E^{0}_{Free} - E^{n}_{defect} - nE^{Isolated}_{Fe})}{n} \quad (4.1.1)$$

where E^{0}_{Free} is the electronic of the troilite supercell free of vacancies, E^{n}_{defect} is the energy of the supercell with n vacancies, and $E^{isolated}_{Fe}$ is the total energy of the isolated iron atom, calculated using the unit cell of the same size of the bulk. The variable n represents the number of vacancies. The values obtained for the formation energy of iron vacancies are compiled in Table 2.

[1] The results of this chapter were accepted for publication at the J. Phys. Chem. C.

Table 2: Concentration of iron vacancies (x), cohesive energy (in eV/atom), vacancy formation energy for each molar fraction (in eV/atom), optimized lattice constants (a, b, c in Å), volume of the super cell after the optimization (in Å^3).

x	a	b	c	V	$\mathbf{E^{cohesive}}$	$\mathbf{E^{vac}}$
0.000	11.446	5.986	10.482	607.32	-6.171	-
0.042	11.720	5.717	10.549	606.04	-6.144	7.439
0.083	11.545	5.734	10.564	606.10	-6.106	7.665
0.125	11.569	5.737	10.477	600.37	-6.067	7.718
0.167	11.533	5.731	10.396	593.43	-6.036	7.649
0.208	11.510	5.693	10.245	580.23	-5.993	7.696
0.250	11.312	5.617	10.368	571.80	-5.892	8.121

As the number of vacancies increase from one to six, the vacancy formation energy ranges from 7.44 eV/atom to 8.12 eV/atom, confirming the endothermic nature of the process. Such defect formation may occur during synthesis or as a consequence of thermal treatments [80], [83]. This aligns with geological observations, where monoclinic pyrrhotite (Fe_7S_8) and hexagonal pyrrhotite (Fe_9S_{10}) are more abundant then stoichiometric troilite, likely due to the high temperatures condition in which these minerals typically form [82], [83].

The impact of the defects on the equilibrium volume of the unit cell is shown in Figure 9a. Initially, as defects are introduced and the cell structure is relaxed, the unit cell volume shows minimal changes. However, starting from the third vacancy, the unit cell volume decreases by approximately 4.4 % with the addition of up to three iron vacancies. The contraction in the unit cell volume is attributed to the charge imbalance caused by the removal of Fe^{2+} ions, which is compensated by the oxidation of neighboring Fe^{2+} to Fe^{3+}. The increase in vacancies raises the number of Fe^{3+} ions, thereby enhancing coulombic attraction within the unit cell and reducing the equilibrium volume.

The cohesive energy, calculated using equation 4.1.2, represents the estimated energy required to dissociate a solid into its isolated atoms [85]. E^n_{defect} is the electronic energy of the troilite supercell with *n* defects, N_{Fe} denotes the number of iron atoms, N_S represents the number of sulfur atoms in the respective unit cell, $E_S^{isolated}$ and $E_{Fe}^{isolated}$ are the total energy of the sulfur and iron atom, calculated using the unit cell of the same size of the bulk.

$$E^{cohesive} = \frac{(E^n_{defect} - N_{Fe}E_{Fe}^{isolated} - N_S E_S^{isolated})}{N_{Fe} + N_S} \quad (4.1.2)$$

Figure 9b presents the cohesive energy of the unit cell as a function of the number of vacancies. A linear regression with $R^2 = 0.9969$ suggests that the energy required to form a vacancy remains nearly constant regardless of the number of existing defects within the range

studied. This linear behavior indicates that the components of the free energy can be considered additive under these conditions.

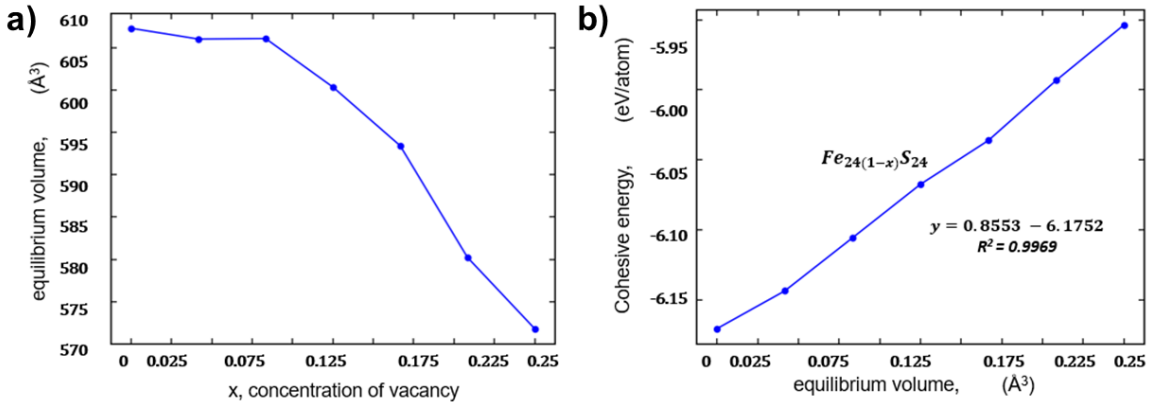

Figure 9: Equilibrium volume (Å^3) related to the concentration of iron vacancies (a). Cohesive energy of the solid as a function of the number of vacancies (b).

4.2 Density of States of troilite and its defect structures

Each created iron vacancy induces to the oxidation of two iron atoms, changing their oxidation states from $Fe^{2+}$to Fe^{3+} to maintain charge neutrality. Figure 10 shows the project density of states (PDOS) for troilite structure from zero to five vacancies within the range of -8 eV to 2 eV. The new electronic states arising between the valence and conduction band indicates the presence Fe^{3+} in the structure, resulting from the formation of vacancy-induced electronic states [80], [86].

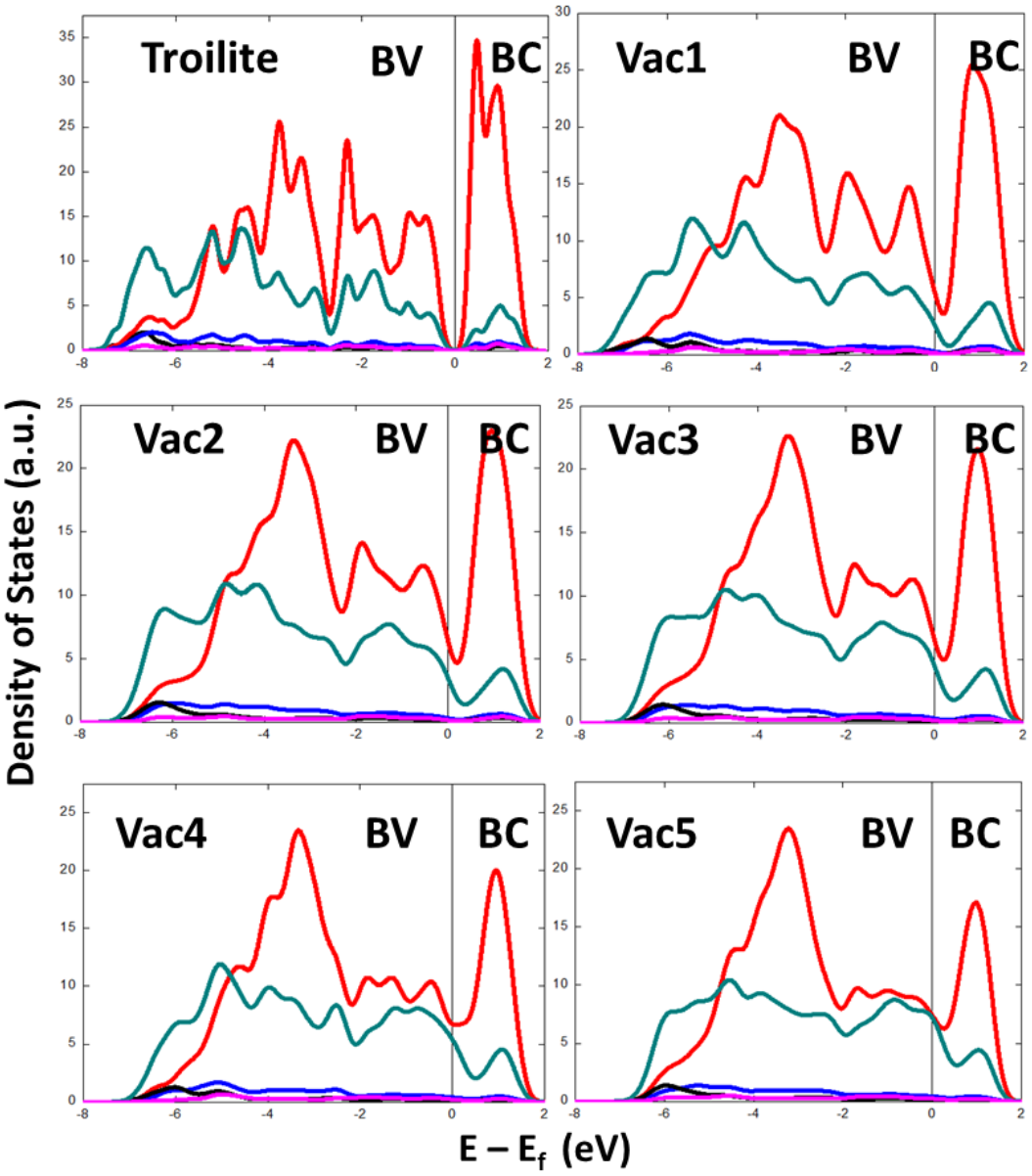

Figure 10: Projected density of states for troilite with different number of iron vacancies obtained with GGA + U = 2. Red line: Fe 3d orbitals; Green line: S 3p orbitals, blue line: Fe 4s orbitals; Pink line: S 3s orbitals.

Troilite is a semiconductor material with a narrow-gap of 0.04 eV [87], [88]. Figure 11 presents the band structure and the project density of states calculations obtained through DFT, showing a theoretical band gap of 0.12 eV, which is larger than the experimental value, but smaller than other DFT/Plane Waves calculations, which reported values around 0.49 eV [35]. Figure A4 of the Appendix shows the band structure of troilite within the range of -8 eV to 2 eV, along with the project density of states, highlining the orbital contributions to the band structure. The presence of Fe^{3+} in the electronic structure of troilite significantly alters its conduction properties. Vacancies in the structure act as recombination sites for charge carriers or introduce defect energy levels, which serve as intermediate electronic states [86], [87]. These defect energy levels appear near the Fermi level, associated with the generation of vacancies, and can lead to notable changes in the properties of the material [86]. For instance, the band gap disappears immediately after the formation of the first vacancy. As more vacancies are introduced, new electronic states forms near the Fermi level, tranforming the troilite structure into a conductor.

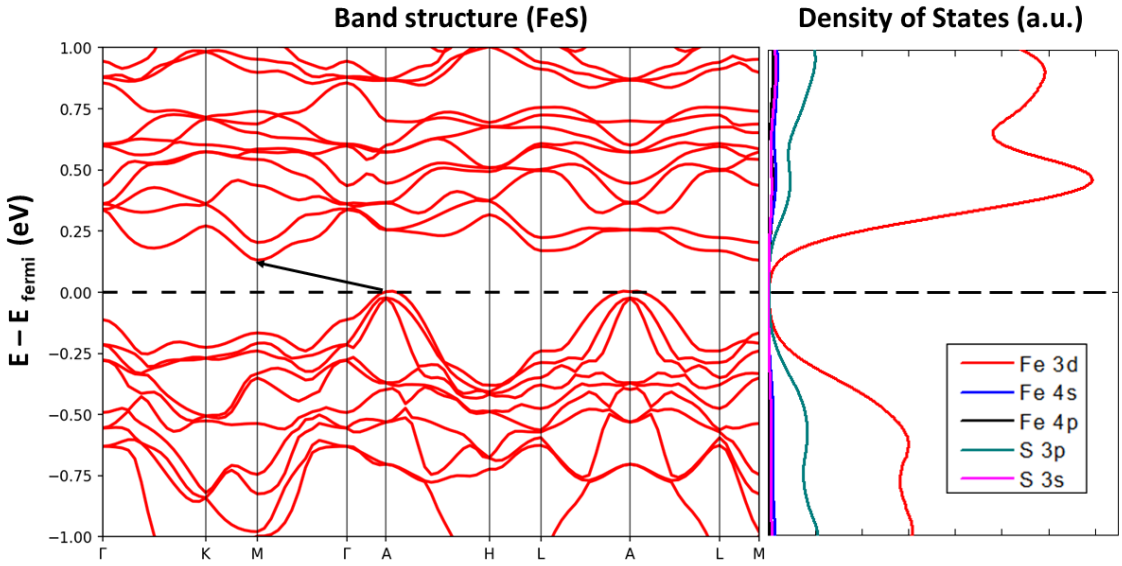

Figure 11: Band structure and projected density of states of troilite showing an indirect band gap of 0.12 eV.

The changes in the electronic properties of troilite after the vacancy formation are interesting yet expected. Troilite belongs to the pyrrhotite group, where, except for troilite, all other members are non-stoichiometric variations with varying numbers of vacancies [4], [16]. Monoclinic pyrrhotite, the most abundant non-stoichiometric variant, differs from troilite in being magnetic and exhibiting conductive properties with no band gap [20]. Additionally, it is speculated that, in monoclinic pyrrhotite, maintaining charge balance in the valence states of

Fe and S requires the oxidation of some Fe^{2+}species to Fe^{3+}. This hypothesis has been confirmed by photoemission spectroscopy [28].

Our results on the formation of iron electronic states in the conduction band align with previous investigations regarding the presence of Fe^{3+} in monoclinic pyrrhotite. The observed changes in electronic behavior — from semiconductor to conductor — reinforce the formation of defect energy levels within the energy gap region.

4.3 Helmholtz free energy of the formation for troilite native vacancies

The structural stability of troilite and its defect structures were investigated through a thermodynamic approach based on the global reaction described in equation 4.3.1, where *n* represent the number of iron atoms removed from the pristine $Fe_{24}S_{24(s)}$ lattice**:**

$$Fe_{24}S_{24(s)} \rightarrow Fe_{24-n}S_{24(s)} + nFe_{(s)} \quad 4.3.1$$

As iron vacancies are introduced, various nonstoichiometric structures are formed, culminating in the formation of monoclinic pyrrhotite (Fe_7S_8). To determine the relative stability of troilite and its defect structures with varying vacancy concentrations, we evaluated the changes in the Helmholtz free energy (ΔF), as defined in equation 4.3.2:

$$\Delta F(N_{vac}) = \Delta U(N_{vac}) - T\Delta S(N_{vac}) \quad 4.3.2$$

In this expression, T is the absolute temperature, while $\Delta U(N_{vac})$ and $\Delta S(N_{vac})$ are the internal-energy and entropy associated to the formation of vacancies, respectively. The internal energy $\Delta U(N_{vac})$ can be described according to equation 4.3.3, which includes two components: the electronic energy $\Delta E^{elec}(N_{vac})$ and the vibrational internal energy $\Delta E^{vib}(N_{vac})$.

$$\Delta U(N_{vac}) = \Delta E^{elec}(N_{vac}) + \Delta E^{vib}(N_{vac}) \quad 4.3.3$$

The electronic component, $\Delta E^{elec}(N_{vac})$, can be calculated as the difference between the electronic energy of the pristine $Fe_{24}S_{24}$ troilite bulk and that of the defective structure, including the contribution from the removed iron atoms, which is referenced as the electronic energy per atom of the bulk iron, as expressed in equation 4.3.4:

$$\Delta E^{elec}(N_{vac}) = E^{ele}_{total}(N_{vac}) + N_{vac}E^{ele}_{Fe} - E^{ele}_{total}(0) \quad 4.3.4$$

Here, $E^{ele}_{total}(N_{vac})$ is the total electronic energy of the structure with N_{vac} iron vacancies , $E^{ele}_{total}(0)$ is the total electronic energy of the pristine $Fe_{24}S_{24}$ structure, and E^{ele}_{Fe} is the electronic energy per atom of bulk iron metal using the Fe α-bcc phase as reference.

The vibrational energy component, $\Delta E^{vib}(N_{vac})$, was estimated based on the vibrational energy of the pristine $Fe_{24}S_{24}$ structure. Assuming an equipartition of vibrational contributions across atoms, the energy associated with each removed atom was calculated by dividing the total vibrational energy by the number of atoms in the unit cell, as expressed in equation 4.3.5

[89], [90]. Thus, the contribution due to N_{vac} vacancies can be calculated according to equation 4.3.6:

$$E_{atom}^{vib} = \frac{E_{total}^{vib}}{N_{atom}} \quad 4.3.5$$

$$\Delta E^{vib}(N_{vac}) = N_{vac} E_{atom}^{vib} \quad 4.3.6$$

Here, E_{total}^{vib} is the total vibrational energy of the unit cell, and N_{atom} is the number of atoms in the unit cell.

The variation of entropy $\Delta S(N_{vac})$ is decomposed into two distinct terms, as proposed by Lucas et al. [91]: the variation of vibrational entropy $\Delta S^{vib}(N_{vac})$ and the conformational entropy $\Delta S^{conf}(N_{vac})$:

$$\Delta S(N_{vac}) = \Delta S^{vib}(N_{vac}) + \Delta S^{conf}(N_{vac}) \quad 4.3.7$$

The conformational entropy variation, $\Delta S^{conf}(N_{vac})$, arise from the distribution of vacancies within the structure and was modeled by considering the system as an ideal binary mixture of vacancies and iron atoms [90], [91]. This contribution is described by equation 4.3.8, where N_{site} represents the number of sites available for vacancy formation in the unit cell, that is 24 for the model used, k_b is the Boltzmann constant, and *x* is the molar fraction of vacancies, given by equation 4.3.9:

$$\Delta S^{conf}(N_{vac}) = -N_{site} k_b [x ln(x) + (1-x) ln(1-x)] \quad 4.3.8$$

$$x = \frac{N_{vac}}{N_{site}} \quad 4.3.9$$

The vibrational entropy, $\Delta S^{vib}(N_{vac})$, was estimated analogously to the vibrational energy term, assuming equipartition of entropy per atom. The entropy contribution per atom was obtained from the total vibrational entropy of the pristine $Fe_{24}S_{24}$ structure, as described by equation 4.3.10. The overall change in the vibrational entropy resulting from the formation of N_{vac} vacancies was then calculated using equation 4.3.11:

$$S_{atom}^{vib} = \frac{S_{total}^{vib}}{N_{atom}} \quad 4.3.10$$

$$\Delta S^{vib}(N_{vac}) = N_{vac} S_{atom}^{vib} \quad 4.3.11$$

S_{total}^{vib} is the total vibrational energy of the $Fe_{24}S_{24}$ unit cell, and N_{atom} is the number of atoms in the unit cell.

Figure 12a and 12b present the Helmholtz free energy and its individual contributions as a function of the iron vacancy concentration, evaluated at 750 K and 800 K, respectively. The minimum Helmholtz free energy is observed around at x = 0.11 (750K) and x = 0.13 (800K).

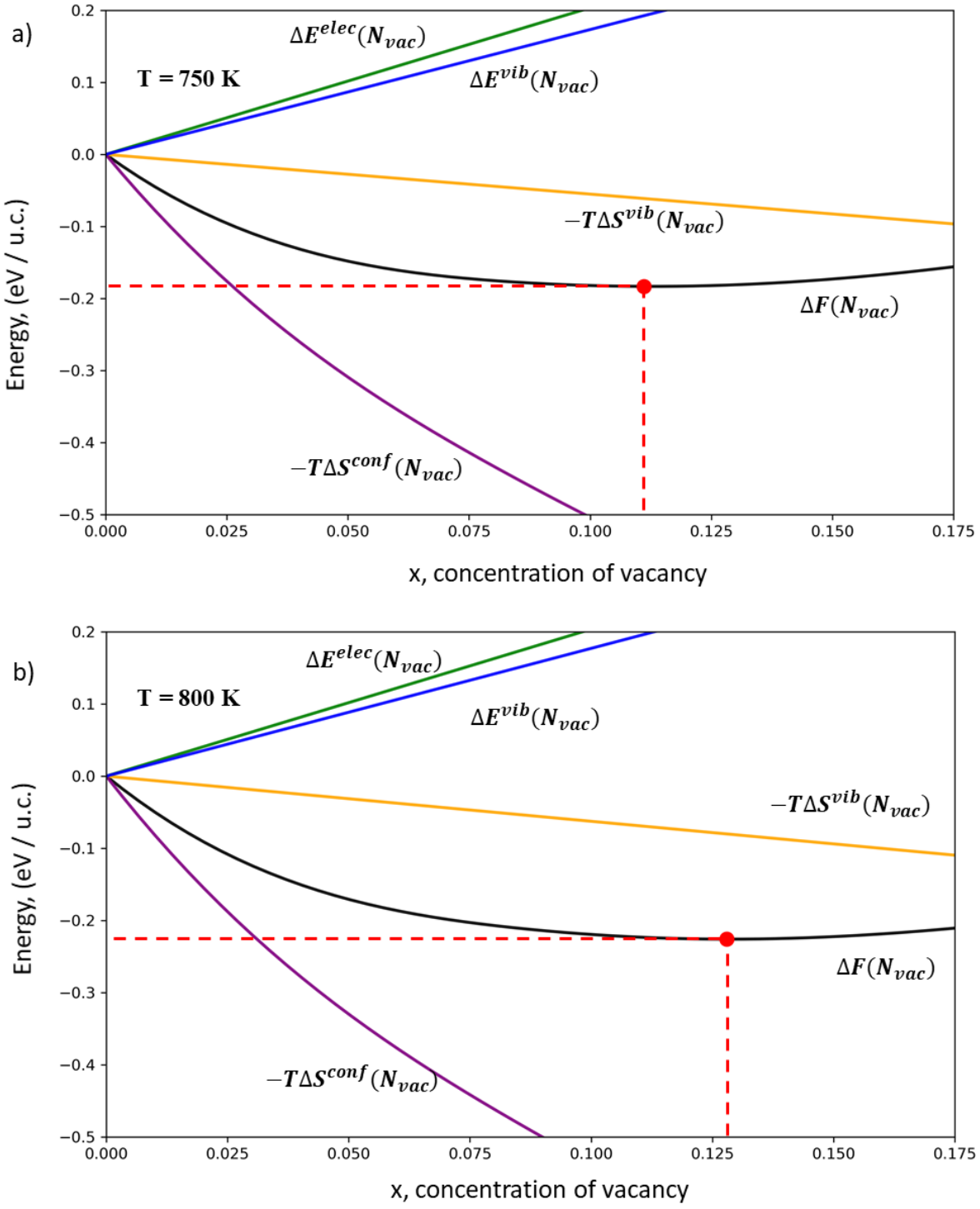

Figure 12: Variation in Helmholtz free energy per unit cell (u.c.) and its partial components for iron vacancies in the troilite structure at a) 750K and b)800 K. Red point indicate the minimum free energy.

Figure 13 illustrates the variation of the Helmholtz free energy per unit cell as a function of both temperature and vacancy concentration. The transition from stoichiometric troilite to nonstoichiometric pyrrhotite phases becomes favorable as the temperature rises, with vacancy concentration surpassing 12.5% - a concentration of defects of monoclinic pyrrhotite structure [2], [28]. According to the Fe-S phase diagram reported by Chen et al. [39], once all

nonstoichiometric pyrrhotite structures derived from troilite have formed, a mixture of pyrite and pyrrhotite is observed between 700 K and 1000 K. The date used to construct these curves are presented in Table A2 of the appendix.

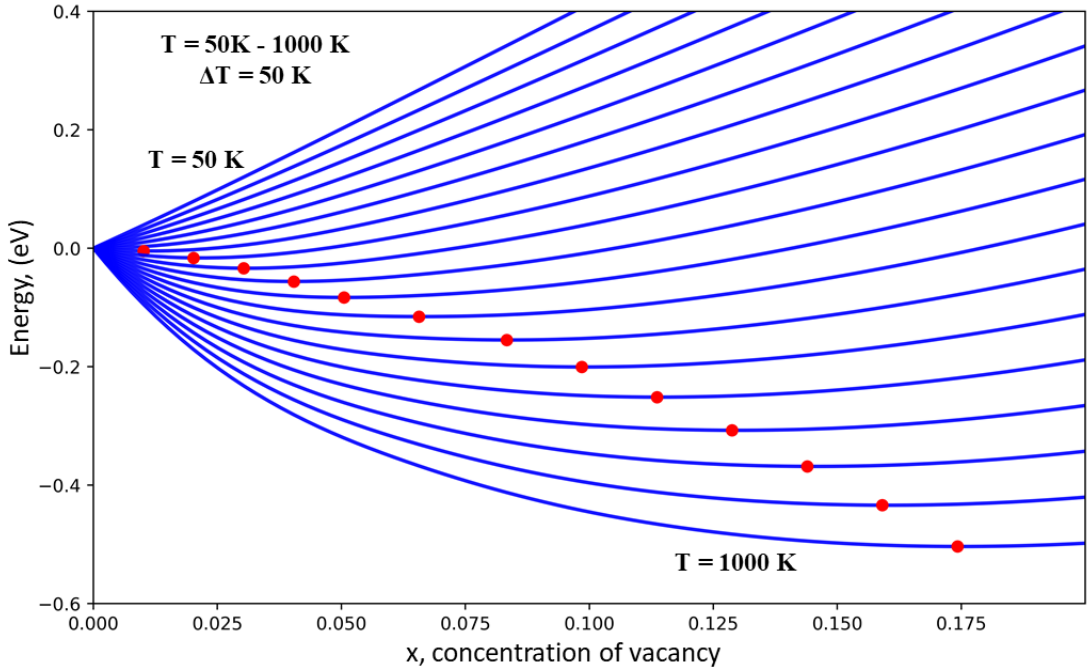

Figure 13: Variation in Helmholtz free energy per unit cell (u.c.) as a function of vacancy concentration in the troilite structure at different temperatures. Red points indicate the minimum energy for each curve.

4.4 From monoclinic pyrrhotite to hexagonal pyrrhotite

The synthesis of materials belonging to the pyrrhotite family are generally obtained at temperatures close to 500 K, under such conditions, the so-called 4C or monoclinic pyrrhotite is the predominant phase obtained under these conditions [37], [38], [39], [40]. However, the thermodynamic analysis presented at Figures 12 and 13 suggests a different behavior: Instead of jumping straight to the monoclinic configuration, phases with intermediated concentrations of iron vacancies are formed initially and only between 750 K and 800 K does the system accumulate the 12.5% deficit of iron that defines the monoclinic structure. This theoretical result contrasts with experimental observations, where the monoclinic phase is commonly synthesized at temperatures near 500 K [37], [39], [40]. Therefore, the troilite thermodynamic model alone does not fully explain why the formation of the monoclinic structure with 12.5 % vacancies is favored over the hexagonal phases with intermediate levels of iron defects.

To investigate this issue and better understand the energetic preference for the monoclinic symmetry in the presence of iron vacancies, we built an artificial, vacancy-free monoclinic cell by filling all empty sites in the fully relaxed monoclinic pyrrhotite. This approach enabled the generation of a stoichiometric pyrrhotite while preserving the monoclinic symmetry. Starting from this stoichiometric structure, iron atoms were removed one by one following the same procedure previously applied to the troilite structure described in section 4.1 for troilite. The crystallographic details for the artificial monoclinic pyrrhotite are provided in Figure A5 of the appendix.

Figure 14 shows the variation of the Helmholtz free energy per unit cell, along with its electronic, vibrational, and entropic components, as a function of vacancy concentration at 500 K. The minimum Helmholtz free energy is found near x = 0.125. These temperatures are in agreement with experimental observations, where monoclinic pyrrhotite is typically synthesized around 500 K. The date used to construct these curves are presented in Table A3 of the appendix. Additionally, the equipartition of energy was applied in the thermodynamic analysis of the stoichiometric monoclinic pyrrhotite, and the cohesive energy date used in this approach are presented in Table A4 of the appendix.

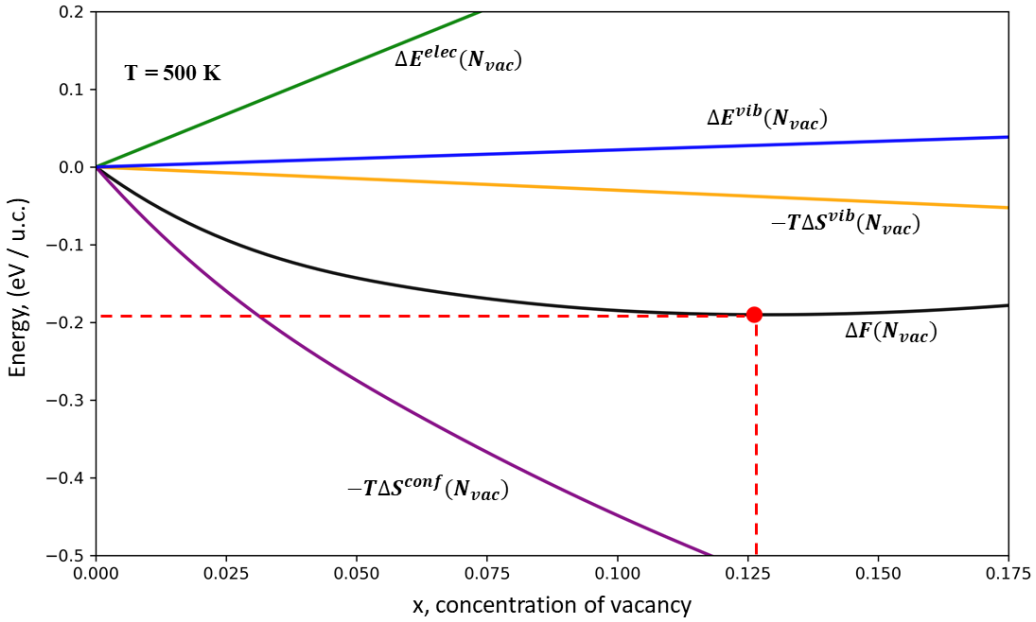

Figure 14: Variation in Helmholtz free energy per unit cell (u.c.) and its partial components for iron vacancies in the monoclinic pyrrhotite structure at 500 K.

Figure 15 compares how the Helmholtz free energy changes with temperature for two structural models with the same defect concentration: one based on the monoclinic symmetry and the other from the hexagonal structure. Despite methodological limitations, particularly for

the thermodynamic treatment of systems with high number of vacancies, this analysis still gives valuable information. Below 700 K, the monoclinic pyrrhotite with 12.5 % iron vacancies has the lower Helmholtz free energy, making it thermodynamically more stable than the hexagonal counterparts. In other words, the monoclinic phase is favored at lower temperatures. However, as the temperature increases, the hexagonal configuration becomes the stable one, with the crossover occurring around 700 K.

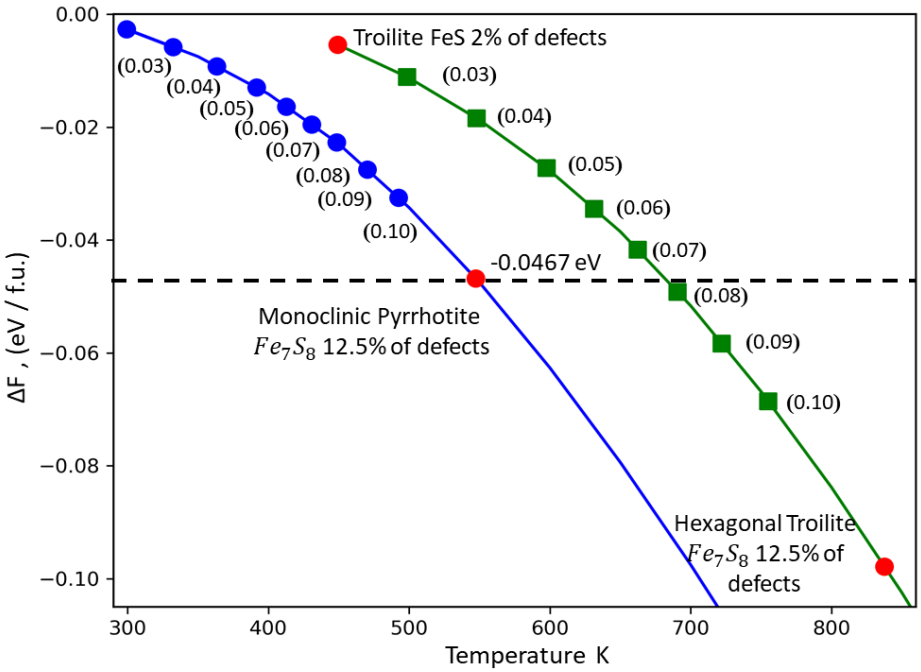

Figure 15: Helmholtz free energy per formula unit (f.u.) vs. temperature for defective structures of the pyrrhotite based on monoclinic (blue) and hexagonal (green) symmetries. The numbers alongside the curves indicate the percentage of iron vacancies in each structure.

These findings agree with the experimental results by Moreau et al. [19]. In their work, pyrite (FeS_2) was heated to 1023-1073 K in an inert atmosphere to synthesize pyrrhotite phase, then reheated to 1498-1598 K so that the melt could crystallize into stoichiometric high-purity troilite. Notably, the authors' observation of temperature-induced transformation from monoclinic pyrrhotite to hexagonal troilite supports our thermodynamic predictions. The significant energy difference observed in the results around 500 K offers a clear thermodynamic rationale for the experimental stabilizations of monoclinic phase at these temperatures. At moderated temperatures, the monoclinic Fe_7S_8 structure with 12.5% iron vacancies is favored. However, further heating promotes symmetry changes and defect reorganization, eventually producing stoichiometric troilite [19].

It is important to note that a meaningful comparison between monoclinic and hexagonal models requires the same number of atoms per formula unit. The monoclinic structure contains 64 atoms, while the hexagonal structure has 48. To enable direct comparison, the Helmholtz

free energy of the monoclinic structure was divided by four, and that of the hexagonal structure by three, giving a common formula unit of 16 atoms for both structures. This normalization ensures a consistent basis for comparing the relative energetic stability of the two symmetries.

4.5 Bonding properties of Nonstoichiometric and Stoichiometric pyrrhotite

It has been observed that the formation of vacancies in the troilite unit cell results in a decrease of the troilite unit cell volume. This contraction indicates that the structure exhibits some ionic character. As more vacancies are created, Coulomb forces grow increase leading to the contraction of the unit cell, which acts to mitigate the rising electrostatic forces within the structure.

To explore the electronic structure and the bonding properties, both the Electron Localization Function (ELF) [70] and the Quantum Theory of Atom in Molecules (QTAIM) [67] were applied to pristine troilite and the defective models. The ELF values range from 0 to 1, where a value of 1 represents localized electron density, indicating a high probability of finding an electron in a specific region, while a value near 0 implies a low probability of finding an electron in that region, whereas a value close to 0.5 indicates a region where electrons behave like free-electron gas [70], [71], [72]. As shown in Figure 16b, the iron vacancies in the troilite structure with three vacancies are characterized by a complete lack of electron density, with the ELF approaching zero in the vacancy regions. Such empty sites can act as electron acceptors, a useful feature for heterogeneous catalysis [86]. Figure 16b also shows that the electrons left when Fe^{2+} oxidizes to Fe^{3+} are not trapped inside the vacancies.

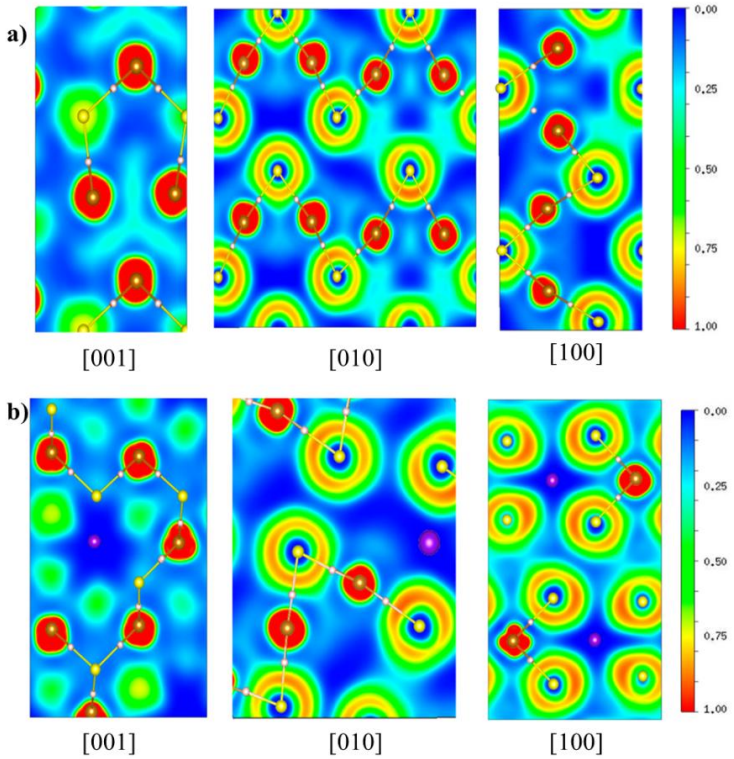

Figure 16: Electron localization function for the a) troilite supercell and b) three-iron vacancy (Vac3) structure. The purple dots represent the position of the vacancy. White dots along the chemical bonds refers to the bond critical points (BCPs).

The QTAIM describes bonds by the electron density ($\rho(r_c)$ (in e/bohr^3 units)) along side with the gradient and Laplacian ($\nabla^2\rho(r_c)$ (in e/ bohr^5 units)) at each bond critical point (BCP) [67], [68]. A positive Laplacian points to an ionic bond, while a negative Laplacian indicates a covalent bond [67], [68], [69]. In addition to the ELF analysis, Figure 16a and 16b illustrates the BCPs as small white dots along the chemical bonds. In troilite and its defect structures, the Fe-S show density values ranging from 0.083 to 0.079 a.u. (atomic units) and the Laplacian values ranging from 0.150 to 0.123 a.u, values typical of ionic bonding. When comparing the electron density of troilite to other sulfide minerals, the As-S BCP in arsenopyrite ($AsFeS$) exhibit a density of 0.0828 a.u. and Laplacian of -0.0075, indicating a covalent character [92]. Aray et al. [93] reported a density of 0.079 a.u. for pyrite (FeS_2) Fe-S bonds, while chalcopyrite ($CuFeS_2$) is displays strong covalent bond character [94]. Among the sulfide materials, both troilite (FeS) and covellite (CuS) exhibit similar characteristics in terms of bond properties. Covellite displays a more ionic character in the *Cu-S* bond, with a charge density at the bond critical point (BCP) of 0.076 a.u. and a Laplacian of 0.166 a.u, indicating a similar ionic character with the *Fe-S* bond in troilite structure [95]. Table 6.9 lists the charge density and the Laplacian values at the bond critical point for the structures and their respective bonds discussed above.

Regions where the gradient of the electron density is zero are known as zero-flux surfaces. These regions divided the crystal into distinct atomic basins. The integration of the charge density inside these basins gives the number of electrons associate with each atom. Using those charges, the degree of ionicity, *c*, was calculated using equation 4.5.1:

$$c = \frac{1}{N}\sum_{i}^{N}\frac{Q(\Omega_i)}{QI(\Omega_i)} \tag{4.5.1}$$

In this equation, $Q(\Omega)$ is the Bader charge, $QI(\Omega)$ is the formal oxidation state, and *N* the number of atoms in the cell [96], [97]. The *c* value lies between 0 (covalent) and 1 (fully ionic). For troilite and its vacancies models, c-value ranges from 0.466 to 0.434, taking Fe^{2+} and S^{2-}oxidation states as reference, suggesting a solid with partially ionic character. The c value for troilite and its defect structures are about twice as large as that of arsenopyrite, which is reported to be 0.205 [92].

Metal oxides are usually more ionic than metal sulfides. For instance, Guimarães et al. [98] reported c-values of 0.59 for hematite, 0.97 for corundum, 0.63 for goethite, and 0.85 for diaspore, indicating a highly ionic character in these oxyhydroxides. Additionally, the positive Laplacian of these oxides confirm their ionic nature. Ionicity and Laplacian values for all systems discussed are collected in Table 6.9.

Table 3: Bond critical points in QTAIM analysis and degree of ionicity (c).

Phase	Charge Density $\rho(r_c)$	Laplacian $\nabla^2\rho(r_c)$	c	Chemical meaning
FeS (Troilite)	0.083	0.150	0.47	$Fe-S$
Vac1	0.083	0.133	0.46	$Fe-S$
Vac2	0.081	0.131	0.46	$Fe-S$
Vac3	0.081	0.126	0.46	$Fe-S$
Vac4	0.080	0.125	0.45	$Fe-S$
Vac5	0.079	0.123	0.44	$Fe-S$
CuS [99]	0.078	0.101	0.32	$Cu-S$
	0.135	0.079		$S-S$
FeS_2 [93]	0.079			$Fe-S$
	0.132			$S-S$
FeS_2 [100]	0.115	-0.015		$S-S$
FeS_2 [100]	0.126	-0.043		$S-S$
$FeAsS$ [92]	0.083	-0.008	0.21	$As-S$
	0.073	0.049		$Fe-As$
$\alpha-FeOOH$ [98]	0.091	0.011	0.63	$Fe-O$
$\alpha-Fe_2O_3$ [98]	0.061	0.014	0.59	$Fe-O$
$\alpha-Al_2O_3$ [98]	0.052	0.010	0.97	$Al-O$
$\alpha-AlOOH$ [98]	0.072	0.015	0.85	$Al-O$

5 OXIDATION MECHANISM OF MONOCLINIC PYRRHOTITE

5.1 Slab model and vacuum size

To simulate reactions occurring on surfaces, it is necessary to develop a model that represents one of the crystallographic directions of the materials. In solid-state computational chemistry, a widely used approach for this purpose is the slab model. A slab is essentially a unit cell cleaved along a specific crystallographic direction. After cleaving, a vacuum region is introduced between the periodic images of the slab, thereby creating a surface [101]. Figure 17a illustrates an example of a slab model.

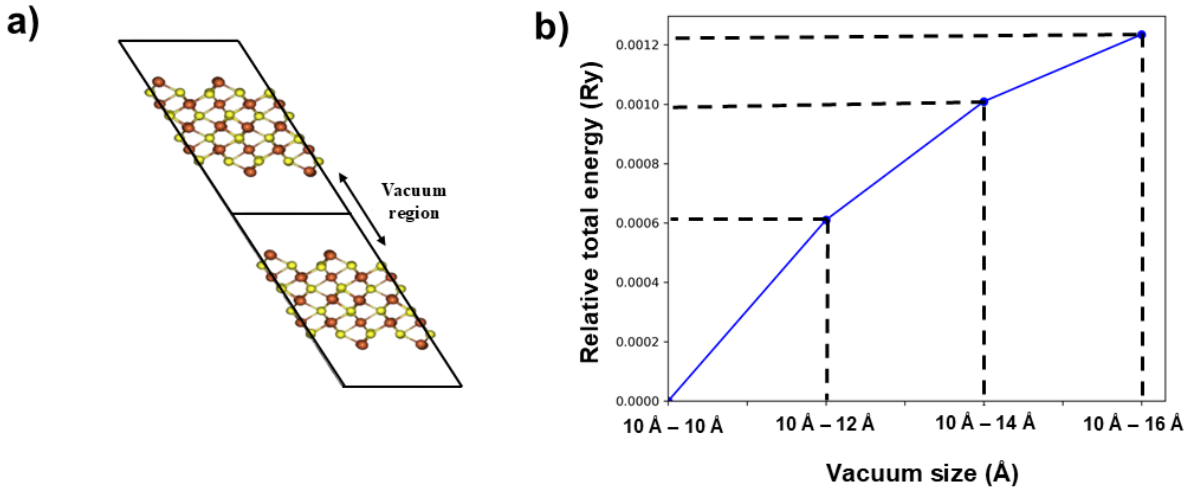

Figure 17: (a) Slab model; (b) Variation of the relative total energy as a function of vacuum thickness along the crystallographic c-direction.

Due to the material's periodic nature, a vacuum must be added between the periodic images to avoid unwanted interactions between them [101]. To ensure both accuracy and computational efficiency, we analyzed the effect of vacuum thickness by varying it to 10, 12, 15, 18 and 20 Å, performing single-point energy calculations for each case. Based on a convergence criterion of $10^{-3}\ Ry$, we found that a vacuum thickness of 10 Å is sufficient to avoid significant interactions between slabs, while keeping the model computationally efficient. Figure 17b shows how the total energy varies with the vacuum size.

Base on this analysis, Table 4 summarizes the parameters used to describe surface reactions in all subsequent calculations. The energy cut-off, k-points mesh, Hubbard U parameter, and magnetization settings were kept the same as those used for the bulk calculations. The choice of the 001-cleavage plane is discussed in detail in the next section.

Table 4: Simulation parameters used for the (001) surface.

Parameter	(0 0 1) Surface
Plane-wave cutoff energy	60 Ry
k-points mesh	1x2x1
Hubbard U for Fe^{2+} and Fe^{3+}	1 eV
Magnetization	Ferromagnetic
Vacuum thickness	10 Å

5.2 Definition of the preferential surface

Monoclinic pyrrhotite does not exhibit a preferential cleavage plane, making it necessary to determine the most favorable surface for modeling. Zhao et al. [42], based on DFT calculations, indicates that the (001) plane is the most likely cleavage surface.

Chen et al. [1], based on DFT calculations, investigated the surface reconstruction of monoclinic pyrrhotite. In their work, they observed a significant surface relaxation. Specifically, some sulfur atoms from the second layer moved to the first layer, while some iron atoms in the topmost layer shifted down to the second layer. Based on their results, we aimed to investigate a surface that undergoes a similar reconstruction process.

To identify the most favorable surface, we calculated the cleavage surface energy for the (001), (010), and (100) planes. Figure 18 shows the different cleavage planes investigated, each leading to distinct surfaces terminations.

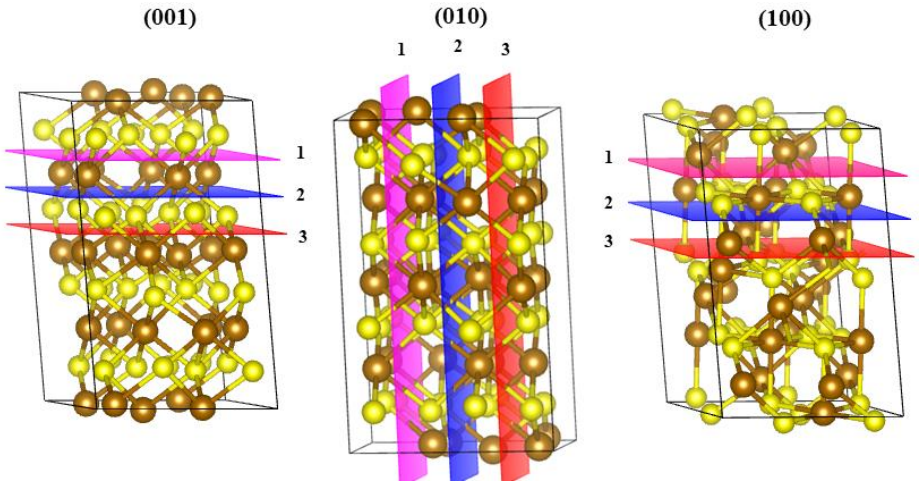

Figure 18: Cleavage planes and surface terminations analyzed in this study; Iron atoms are shown in brown, and sulfur atoms in yellow.

Cleavage process involves two main steps: (1) the braking of chemical bonds and (2) the relaxation or reconstruction of the surface, during which atoms reorganize to minimize the surface energy. The first step in the analysis is to calculate the energy required to break the chemical bonds, referred to as the non-relaxed cleavage energy (γ_{nre}). Lower positive values indicate surfaces with higher probability of formation [34], [42], [95], [102]. This energy is calculated using equation 5.2.1:

$$\gamma_{nre} = \frac{E_{Snre} - E_B}{2A} \tag{5.2.1}$$

where, E_{Snre} is the energy of the unrelaxed surface, E_B is the energy of the optimized bulk, and A is the surface area. The factor of 2 accounts for the creation of two surfaces – top and bottom – during cleavage process [102]. Table 5 presents the cleavage surface energy calculated for 9 surfaces generated using the (001), (010), and (100) cleavage planes. Among the surfaces analyzed, those derived from the (001) cleavage plane exhibits the lowest cleavage energy, indicating that their formation is energetically the most favorable [95]. Since less energy is required to create surfaces using the (001) plane, we performed the second step – the relaxation or reconstruction – only for the surfaces derived from this cleavage plane. The bulk energy, along with surface area, and energy of the unrelaxed surface, are presented in the Table A5 of the appendix.

Table 5: Non-relax cleavage surface energy calculated for 9 surfaces generated using the (001), (010), and (100) cleavage planes.

Surface	Non-relaxed cleavage energy ($\gamma_{nre}; eV/\text{Å}^2$)		
	(001)	(010)	(100)
1	0.104	0.162	0.261
2	0.087	0.155	0.253
3	0.119	0.162	0.237

With all the surfaces generated from the (001) cleavage plane, we proceeded to the next step: calculating the surface relaxation energy (S_{re}) for the three resulting surfaces. The relaxation energy corresponds to the energy released during the surface reconstruction process and can be calculated using equation 5.2.2:

$$S_{re} = \frac{E_{Sre} - E_{Snre}}{2A} \tag{5.2.2}$$

where E_{Sre} is the energy of the relaxed surface, E_{Snre} is the energy of the unrelaxed surface, and A is the surface area. It is important to note that the top and bottom surfaces must be relaxed independently, as each may undergo a distinct reconstruction. Figure 19 illustrates a schematic representation of the three relaxation steps: in Figure 19a, only the top surface is relaxed while the bottom is kept fixed, allowing the calculation of the relaxation energy of the top termination (S_{re-top}); in Figure 19b, the bottom surface is relaxed with the top fixed, enabling the calculation of the relaxation energy of the bottom termination ($S_{re-bottom}$); and Figure 19c, both terminations remain fixed, corresponding to the calculation of the unrelaxed cleavage energy (γ_{nre}).

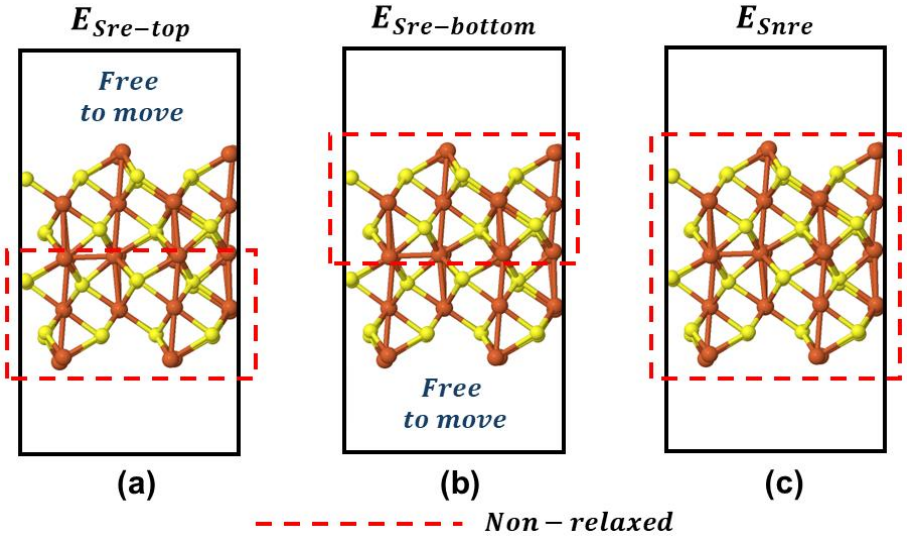

Figure 19: Relaxation scheme of the slab terminations during the reconstruction process: (a) bottom surface fixed, (b) top surface fixed, and (c) both surfaces fixed.

After accounting for both cleavage and relaxation process, the total cleavage surface energy (γ) is calculated using equation 5.2.3:

$$\gamma = \gamma_{nre} + S_{re-top} + S_{re-bottom} \quad (5.2.3)$$

Table 6 presents the calculated cleavage surface energy (γ), and the surface relaxation energies for the top (S_{re-top}) and bottom ($S_{re-bottom}$) terminations.

Table 6: Energies associated with the surfaces generated along the (001) cleavage plane.

Surface	γ_{nre}	S_{re-top}	$S_{re-bottom}$	γ
(001)-1	0.104	-0.022	-0.021	0.061
(001)-2	0.087	-0.009	-0.033	0.046
(001)-3	0.119	-0.018	-0.028	0.073

The value of S_{re-top} , $S_{re-bottom}$, γ_{nre}, and γ are presented in $eV/Å^2$, and the bond lengths are given in Å.

After the relaxation of all surfaces generated from the (001) cleavage plane, the surface labeled (001)-2 exhibited the lowest cleavage energy, indicating that it is the most likely to form during the cleavage of monoclinic pyrrhotite. Figures 20a and 20b show the relaxed structures of the two terminations of the (001)-2. In the (001)-2-bottom surface, the outermost layer consists of sulfur atoms, all coordinated to adjacent iron atoms. In contrast, the (001)-2-top surface undergoes significant reconstruction: after relaxation, sulfur atoms from the second layer move to the first layer, while iron atoms originally at the surface migrate to the second

layer. This substantial atomic rearrangement indicates strong surface relaxation. These findings align with previous DFT studies, which reported that the most stable surface of the monoclinic pyrrhotite often experience notable reconstruction, with sulfur and iron atoms exchanging positions [1], [12], [42].

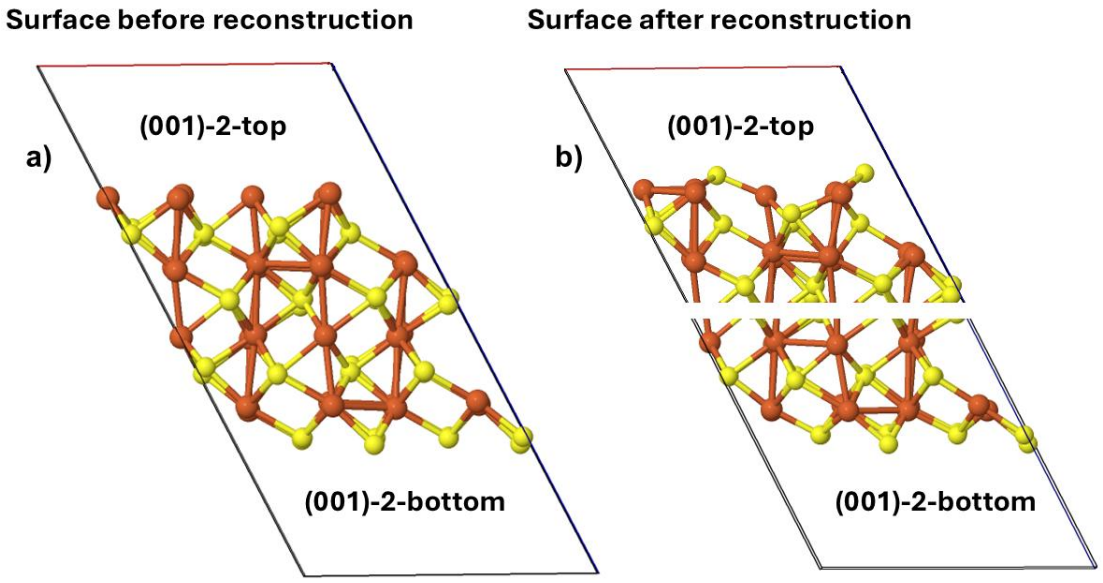

Figure 20: Optimized slab models of (001)-2-top and (001)-2-bottom terminations of monoclinic pyrrhotite surface

Based on these results, the (001)-2-top surface was selected for the next step of the study, which involves investigating the adsorption of oxygen to understand the oxidation process.

5.3 Oxygen adsorption

Oxygen adsorption on the (001)-2-top surface of monoclinic pyrrhotite was investigated through three different mechanisms. In the first (MD1), the O_2 molecule adsorbers simultaneously onto both iron (Fe) and sulfur (S) atoms on the surface. In the second mechanism (MD2), adsorption occurs only on the exposed Fe atoms, while in the third (MD3), interaction happens exclusively with an exposed sulfur atom. These configurations were used as initial geometries to determine the most stable adsorption mechanism. A schematic representation of the three adsorption models is shown in Figure 21.

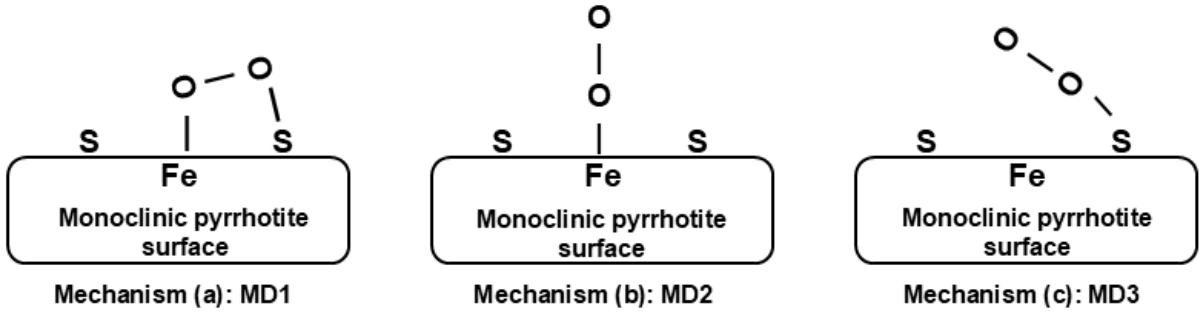

Figure 21: Schematic representation of the adsorption mechanism of O_2 molecule on the monoclinic pyrrhotite surface.

The adsorption of oxygen molecules was obtained by:

$$\mathrm{E}_{ads,O_2} = \mathrm{E}_{slab,O_2} - (\mathrm{E}_{slab,relax} + \mathrm{n}_{O_2}\mathrm{E}_{O_2}) \quad (5.3.1)$$

Among the three models, MD3 was found to be the most stable, being approximately 125.9 and 113.2 kJ/mol more stable than MD1 and MD2, respectively. Figure 22a shows the optimized structure of the MD3 mechanism. In this configuration, the oxygen molecule approaches an exposed sulfur atom, and after adsorption, the $O-O$ bond is broken, leading to the formation of $O-S$ and $O-Fe$ bonds. One oxygen atom (O1) forms a bridge between the sulfur atom and a nearby Fe atom $S-O-Fe$, while the second oxygen atom (O2) binds to three different Fe atoms on the surface, resulting in a tridentate coordination. The $O-S$ bond length is 1.57 Å, and the O–Fe bonds vary between 1.93 and 1.97 Å.

The high adsorption energy calculated for MD3 (–438.71 kJ/mol) indicates that this process cannot be classified as physisorption. Instead, it represents a chemical adsorption mechanism characterized by significant charge transfer and bond rearrangement on the surface, including the complete dissociation of the $O-O$ bond.

Further insights into the nature of the chemical interactions were obtained through Electron Localization Function (ELF) analysis, shown in Figure 22b. The ELF map reveals a strong electron localization between the O1 and S atoms, indicating a covalent character for the $O-S$ bond. In contrast, the bonds between O2 and Fe atoms ($O2-Fe2$, $O2-Fe3$, and $O2-Fe4$) do not exhibit significant electron localization in the bonding region, suggesting a predominantly ionic character.

To quantify the charge transfer during the adsorption, Bader charge along with project density of states analysis were performed. The Bader charge distribution before and after O_2 adsorption is presented in Table 7. The sulfur atom S1 shows a significant loss of +1.41 *e*, indicating oxidation as it donates electrons to the adsorbed oxygen. The oxygen atom O1, which forms the $S-O-Fe$ bridge, gains –1.71 *e*, confirming a strong reduction process. This charge accumulation results from both the electron donation from S1 and additional charge acquired through bonding with a nearby Fe atom. The second oxygen atom, O2, gains –1.25 *e* and interacts with three iron atoms (Fe2, Fe3, and Fe4), each of which loses between +0.30 and +0.40 *e*, indicating mild oxidation.

Despite this charge redistribution, the ELF analysis confirms that the bonding between O2 and the Fe atoms remains predominantly ionic, as there is no significant electron density accumulation between them. This reinforces the idea that while O1 forms a strong covalent bond with sulfur, O2 interacts with Fe through ionic-type bonding, supported mainly by electrostatic interactions.

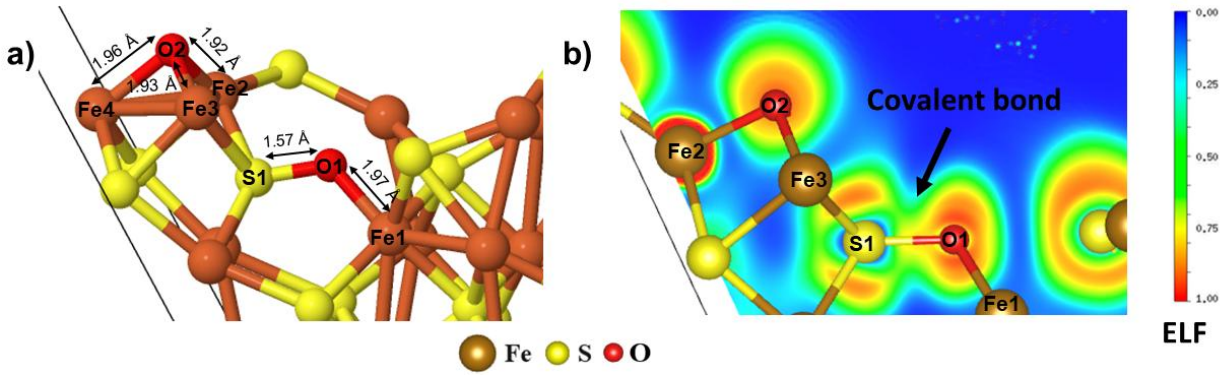

Figure 22: Optimized structure of the MD3 oxygen adsorption on the (001)-3-bottom surface. (a) Geometric configuration showing the O_2 dissociation and formation of S–O and O–Fe bonds. (b) ELF map indicating a covalent S–O bond and predominantly ionic O–Fe interactions.

Table 7: Bader charge (*e*) of atoms involved in the adsorption of oxygen

Atom	Fe_7S_8 (001)-3	$Fe_7S_8 + O_2$ (001)-3	Charge diference
Fe28	7.17	6.79	+0.38
Fe25	7.20	6.88	+0.31
Fe23	7.18	6.78	+0.40
Fe22	6.94	6.87	+0.07
S29	7.03	5.62	+1.41
O1	--	7.72	-1.71
O2	--	7.24	-1.25

Figure 23 shows the projected density of states (PDOS) for the interaction between O1 and S1. The PDOS reveals a significant hybridization between the O1 2p orbitals and the S1 3p orbitals in the energy range from approximately –9 eV to 0 eV. This strong orbital overlap near the Fermi level indicates the formation of molecular orbitals, suggesting the establishment of chemical bonding between oxygen and sulfur. From the PDOS perspective, this is characteristic of a covalent interaction, where the electron density is shared between the atoms, as also evidenced by the ELF distribution shown in Figure 22b. Covalent bonds are typically associated with broad and overlapping peaks in the PDOS, reflecting delocalized electrons and the mixing of electronic states.

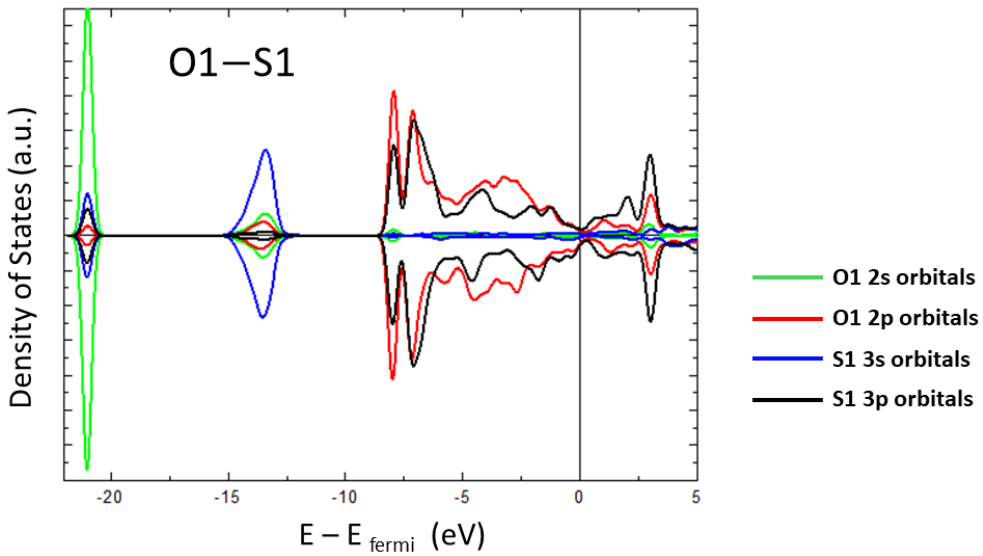

Figure 23: Projected density of states (PDOS) of O1 and S1 atoms, showing strong hybridization between O1 2p and S1 3p orbitals, indicating covalent bonding.

Figure 24 presents the projected density of states (PDOS) for the interaction between oxygen and iron atoms, revealing a predominantly ionic character. This is evidenced by the clear separation between the electronic states of iron (3d, 4p, and 4s) and those of oxygen (2s and 2p), with no significant overlap in the energy range. The lack of orbital overlap means that no molecular orbitals are formed between these atoms. From the PDOS point of view, this is typical of ionic bonds, where electrons are not shared but transferred from one atom to another. In this case, iron loses electrons to oxygen, and the electronic states remain localized, appearing as sharp and well-defined peaks in the PDOS. This observation is also supported by the ELF result, which shows low electron density between oxygen and iron, confirming that there is no electron sharing, as happens in covalent bonds.

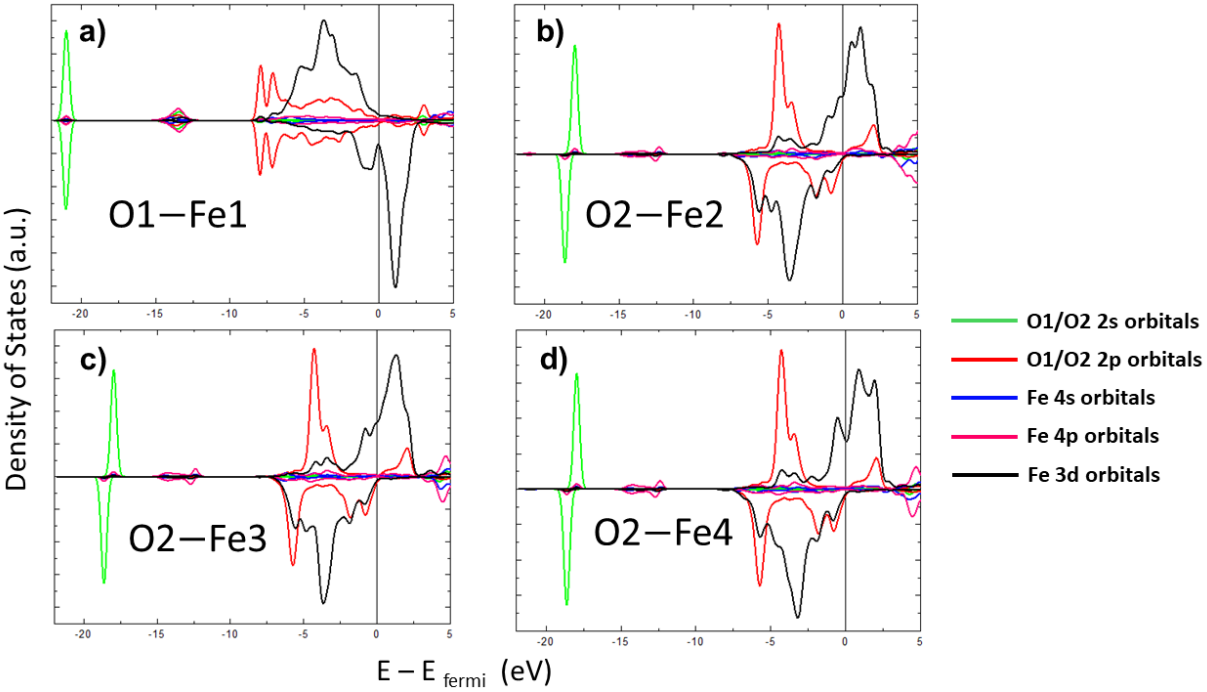

Figure 24: PDOS for the O–Fe interaction, showing ionic character with no orbital overlap and electron transfer from Fe to O, as confirmed by ELF.

In summary, the MD3 mechanism is the most stable pathway for oxygen adsorption on the (001)-3-bottom surface of monoclinic pyrrhotite. The process involves the dissociation of the O_2 molecule, the formation of a covalent S–O bond, and ionic interactions between oxygen and iron atoms, accompanied by substantial charge transfer between the adsorbate and the surface atoms. These findings are consistent with the high adsorption energy observed and provide valuable insights into the initial steps of the oxidation process of monoclinic pyrrhotite.

6 CONCLUSION

This work presented a theoretical investigation on the thermodynamic formation of iron vacancies in troilite and monoclinic pyrrhotite, as well as the initial stages of oxidation on the most stable surface of monoclinic pyrrhotite. All results were obtained through first-principle calculations using Density Functional Theory (DFT), allowing for the evaluation of structural, thermodynamic, and electronic properties with high accuracy. The main objective was to understand how the presence of iron vacancies influences the stability of these materials at different temperatures and how this affects their transformation within the pyrrhotite family.

From the optimized bulk structure of troilite a supercell was constructed to simulate defective systems with varying concentration of iron vacancies. The Helmholtz free energy was calculated for each configuration, considering electronic energy, vibrational energy, vibrational entropy, and configurational entropy. The thermodynamic analysis showed that increasing temperature favors the formation of iron vacancies. Around 500 K, the monoclinic structure with 12.5% of iron vacancies is more stable than all other configurations with lower vacancy concentration and hexagonal symmetry. A crossover in energetic stability is observed near 700 K, beyond which the hexagonal structure of troilite becomes more favorable. These results agree with experimental findings and support the idea that the transformation from monoclinic pyrrhotite to troilite is a gradual, temperature-dependent process, and not an abrupt transition.

The presence of vacancies was also shown to have an important effect on the electronic structure of the material. The removal of iron atoms causes a local imbalance in charge, leading to the oxidation of Fe^{2+} to Fe^{3+} to restore neutrality. This process results in the appearance of new unoccupied states near the Fermi level, changing troilite from a semiconductor to a metallic conductor. These findings help explain the metallic behavior often observed in natural non-stoichiometric pyrrhotite samples.

The analysis of surfaces was also an important part of this study. Several surface terminations generated from different cleavage planes were evaluated, and the most stable one was identified based on cleavage and relaxation energies. The (001)-3-bottom surface showed the lowest total energy after atomic rearrangement and was selected for adsorption studies. The interaction of molecular oxygen with this surface was explored through different adsorption configurations. The results showed that when oxygen adsorbs on exposed sulfur atoms, strong chemical interactions occur, including electron transfer and the formation of covalent bonds. These findings were supported by projected density of states (PDOS), Electron Localization

Function (ELF), and Bader charge analysis. In contrast, other configurations, such as tridentate coordination involving iron atoms, showed weak charge transfer and chemical bonds with strong ionic character.

Based on the results obtained in this work, there are several directions for future research. One important possibility is the investigation of different collector molecules interacting with the (001)-3-bottom surface of monoclinic pyrrhotite. By evaluating how these molecules adsorb and transfer charge, it may be possible to improve flotation processes involving pyrrhotite, which is a secondary mineral commonly associated with sulfide ores and often considered difficult to recover.

Improving its flotation is relevant for mineral processing, especially considering that monoclinic pyrrhotite is one of the main sources of acid mine drainage due to its tendency to oxidize. Therefore, a complete study of the oxidation mechanism—including the co-adsorption of water and oxygen and the subsequent formation of sulfates—could contribute to a better understanding of its environmental impact.

In summary, this work contributes to the understanding of how troilite can transform into other members of the pyrrhotite family through the formation of iron vacancies, and how temperature controls the thermodynamic stability of each phase. It also sheds light on the early stages of oxidation on the monoclinic surface, providing a solid foundation for future studies focused on improving mineral flotation, understanding environmental behavior, and exploring surface reactivity of iron sulfides under different conditions.

REFERENCES

[1] X. Tang e Y. Chen, “A review of flotation and selective separation of pyrrhotite: A perspective from crystal structures”, *Int J Min Sci Technol*, vol. 32, nº 4, p. 847–863, jul. 2022, doi: 10.1016/J.IJMST.2022.06.001.

[2] N. Belzile, Y. W. Chen, M. F. Cai, e Y. Li, “A review on pyrrhotite oxidation”, *J Geochem Explor*, vol. 84, nº 2, p. 65–76, set. 2004, doi: 10.1016/J.GEXPLO.2004.03.003.

[3] H. A. Duarte, E. C. Dos Santos, J. C. De Mendonça Silva, G. F. De Lima, e H. A. De Abreu, “Modeling the oxidation mechanism of pyrite and arsenopyrite – connection to acid rock drainage”, *Spectroscopic Properties of Inorganic and Organometallic Compounds*, vol. 14, p. 162–194, 2018, doi: 10.1039/9781788010719-00162.

[4] D. J. Vaughan e C. L. Corkhill, “Mineralogy of Sulfides”, *Elements*, vol. 13, nº 2, p. 81–87, abr. 2017, doi: 10.2113/GSELEMENTS.13.2.81.

[5] C. hua Zhao, B. zeng Wu, e J. hua Chen, “Electronic structure and flotation behavior of monoclinic and hexagonal pyrrhotite”, *J Cent South Univ*, vol. 22, nº 2, p. 466–471, fev. 2015, doi: 10.1007/S11771-015-2544-4.

[6] A. Akcil e S. Koldas, “Acid Mine Drainage (AMD): causes, treatment and case studies”, *J Clean Prod*, vol. 14, nº 12–13, p. 1139–1145, jan. 2006, doi: 10.1016/J.JCLEPRO.2004.09.006.

[7] C. M. Martins, “Rastreamento geoquímico de possíveis contaminações remanescentes de minerações de pirita no município de Ouro Preto, Quadrilátero Ferrífero, Minas Gerais”, Universidade Federal de Ouro Preto, Ouro Preto, 2005.

[8] L. Q. Lei, C. A. Song, X. L. Xie, Y. H. Li, e F. Wang, “Acid mine drainage and heavy metal contamination in groundwater of metal sulfide mine at arid territory (BS mine, Western Australia)”, *Transactions of Nonferrous Metals Society of China*, vol. 20, nº 8, p. 1488–1493, ago. 2010, doi: 10.1016/S1003-6326(09)60326-5.

[9] E. Dinelli, F. Lucchini, M. Fabbri, e G. Cortecci, “Metal distribution and environmental problems related to sulfide oxidation in the Libiola copper mine area (Ligurian Apennines, Italy)”, *J Geochem Explor*, vol. 74, nº 1–3, p. 141–152, dez. 2001, doi: 10.1016/S0375-6742(01)00180-7.

[10] P. J. Sullivan e J. L. Yelton, “An evaluation of trace element release associated with acid mine drainage”, *Environmental Geology and Water Sciences*, vol. 12, nº 3, p. 181–186, dez. 1988, doi: 10.1007/BF02574730.

[11] M. C. Colin Baird, *N. Colin Baird - N. Colin Baird - Biography - Chemistry - Western University Environmental Chemistry*. 2005.

[12] C. H. Zhao, J. H. Chen, Y. Q. Li, Y. Chen, e W. Z. Li, “First-principle calculations of interaction of O2 with pyrite, marcasite and pyrrhotite surfaces”, *Transactions of Nonferrous Metals Society of China*, vol. 26, nº 2, p. 519–526, fev. 2016, doi: 10.1016/S1003-6326(16)64141-9.

[13] J. M. Nieto *et al.*, “Acid mine drainage pollution in the Tinto and Odiel rivers (Iberian Pyrite Belt, SW Spain) and bioavailability of the transported metals to the Huelva Estuary”, *Environ Int*, vol. 33, nº 4, p. 445–455, maio 2007, doi: 10.1016/J.ENVINT.2006.11.010.

[14] J. Riera, C. R. Cánovas, e M. Olías, “Characterization of Main AMD Inputs to the Odiel River Upper Reach (SW Spain)”, *Procedia Earth and Planetary Science*, vol. 17, p. 602–605, jan. 2017, doi: 10.1016/J.PROEPS.2016.12.161.

[15] J. S. España, E. L. Pamo, E. Santofimia, O. Aduvire, J. Reyes, e D. Barettino, “Acid mine drainage in the Iberian Pyrite Belt (Odiel river watershed, Huelva, SW Spain): Geochemistry, mineralogy and environmental implications”, *Applied Geochemistry*, vol. 20, nº 7, p. 1320–1356, jul. 2005, doi: 10.1016/J.APGEOCHEM.2005.01.011.

[16] D. J. Vaughan, “MINERALS | Sulphides”, *Encyclopedia of Geology*, p. 574–586, jan. 2005, doi: 10.1016/B0-12-369396-9/00276-8.

[17] F. Li, “Studies of structures and phase transitions in pyrrhotite”, Iowa State University, Ames, 1997.

[18] R.T. SHUEY, Org., “Pyrrhotite - Fe1−xS”, em *Semiconducting Ore Minerals*, vol. 4, nº C, Salt Lake City: Elsevier, 1975, 15, p. 290–303. doi: 10.1016/B978-0-444-41357-4.50020-6.

[19] J. G. Moreau *et al.*, “Bulk synthesis of stoichiometric/meteoritic troilite (FeS) by high-temperature pyrite decomposition and pyrrhotite melting”, *Meteorit Planet Sci*, vol. 57, nº 3, p. 588–602, mar. 2022, doi: 10.1111/MAPS.13782.

[20] A. Rohrbach, J. Hafner, e G. Kresse, “Electronic correlation effects in transition-metal sulfides”, *Journal of Physics: Condensed Matter*, vol. 15, nº 6, p. 979, fev. 2003, doi: 10.1088/0953-8984/15/6/325.

[21] R. Skála, I. Císařová, e M. Drábek, “Inversion twinning in troilite”, *American Mineralogist*, vol. 91, nº 5–6, p. 917–921, maio 2006, doi: 10.2138/AM.2006.1999.

[22] “Troilite: Mineral information, data and localities.” Acessado: 14 de junho de 2025. [Online]. Disponível em: https://www.mindat.org/min-4029.html

[23] M. Tokonami, K. Nishiguchi, e N. Morimoto, “Crystal Structure of a Monoclinic Pyrrhotite (Fe7S8)”, 1972.

[24] J. P. R. De Villiers, D. C. Liles, e M. Becker, “The crystal structure of a naturally occurring 5C pyrrhotite from Sudbury, its chemistry, and vacancy distribution”, *American Mineralogist*, vol. 94, nº 10, p. 1405–1410, out. 2009, doi: 10.2138/AM.2009.3081.

[25] A. V. Powell, P. Vaqueiro, K. S. Knight, L. C. Chapon, e R. D. Sánchez, “Structure and magnetism in synthetic pyrrhotite Fe7S 8: A powder neutron-diffraction study”, *Phys Rev B Condens Matter Mater Phys*, vol. 70, nº 1, p. 014415, jul. 2004, doi: 10.1103/PHYSREVB.70.014415/FIGURES/11/THUMBNAIL.

[26] “Pyrrhotite: Mineral information, data and localities.” Acessado: 14 de junho de 2025. [Online]. Disponível em: https://www.mindat.org/min-3328.html

[27] M. Weller, M. Weller, J. Rourke, F. Armstrong, e T. Overton, *Inorganic Chemistry*. Oxford, 2014.

[28] A. R. Pratt, I. J. Muir, e H. W. Nesbitt, “X-ray photoelectron and Auger electron spectroscopic studies of pyrrhotite and mechanism of air oxidation”, *Geochim Cosmochim Acta*, vol. 58, nº 2, p. 827–841, jan. 1994, doi: 10.1016/0016-7037(94)90508-8.

[29] Z. E. Pettifer, J. S. Quinton, e S. L. Harmer, “Reconstruction of pyrrhotite fracture surfaces”, *Miner Eng*, vol. 184, p. 107666, jun. 2022, doi: 10.1016/J.MINENG.2022.107666.

[30] H. W. Nesbitt, “Sulfur and iron surface states on fractured pyrite surfaces”, *American Mineralogist*, vol. 83, nº 9–10, p. 1067–1076, set. 1998, doi: 10.2138/AM-1998-9-1015.

[31] G. Ferreira de Lima, H. Avelino de Abreu, e H. Anderson Duarte, “Surface reactivity of the sulfide minerals”, p. 153–182, out. 2013, doi: 10.1039/9781849737241-00153.

[32] S. L. Harmer e H. W. Nesbitt, “Stabilization of pyrite (FeS2), marcasite (FeS2), arsenopyrite (FeAsS) and loellingite (FeAs2) surfaces by polymerization and auto-redox reactions”, *Surf Sci*, vol. 564, nº 1–3, p. 38–52, ago. 2004, doi: 10.1016/J.SUSC.2004.06.199.

[33] S. L. Harmer, A. R. Pratt, W. H. Nesbitt, e M. E. Fleet, “Sulfur species at chalcopyrite (CuFeS2) fracture surfaces”, *American Mineralogist*, vol. 89, nº 7, p. 1026–1032, jul. 2004, doi: 10.2138/AM-2004-0713.

[34] C. De Oliveira, G. F. De Lima, H. A. De Abreu, e H. A. Duarte, “Reconstruction of the chalcopyrite surfaces-A DFT study”, *Journal of Physical Chemistry C*, vol. 116, nº 10, p. 6357–6366, mar. 2012, doi: 10.1021/JP300713Z.

[35] F. Ricci e E. Bousquet, “Unveiling the Room-Temperature Magnetoelectricity of Troilite FeS”, *Phys Rev Lett*, vol. 116, nº 22, p. 227601, jun. 2016, doi: 10.1103/PHYSREVLETT.116.227601.

[36] L. Argueta-Figueroa *et al.*, “Hydrothermal synthesis of pyrrhotite (Fex-1S) nanoplates and their antibacterial, cytotoxic activity study”, *Progress in Natural Science: Materials International*, vol. 28, nº 4, p. 447–455, ago. 2018, doi: 10.1016/J.PNSC.2018.06.003.

[37] J. Cantu *et al.*, “Removal of arsenic from water using synthetic Fe7S8 nanoparticles”, *Chemical Engineering Journal*, vol. 290, p. 428–437, abr. 2016, doi: 10.1016/J.CEJ.2016.01.053.

[38] T. Liao, W. Wang, Y. Song, X. Wang, Y. Yang, e X. Liu, “HMTA-assisted One-pot Synthesis of Greigite Nano-platelet and Its Magnetic Properties”, *J Mater Sci Technol*, vol. 31, nº 9, p. 895–900, set. 2015, doi: 10.1016/J.JMST.2015.07.006.

[39] Y. H. Chen *et al.*, “Using the high-temperature phase transition of iron sulfide minerals as an indicator of fault slip temperature”, *Scientific Reports 2019 9:1*, vol. 9, nº 1, p. 1–6, maio 2019, doi: 10.1038/s41598-019-44319-8.

[40] N. M. Pedoussaut e C. Lind, “Facile synthesis of troilite”, *Inorg Chem*, vol. 47, nº 2, p. 392–394, jan. 2008, doi: 10.1021/IC701636H.

[41] V. Pontikis, “Surface Reconstruction”, em *Encyclopedia of Materials: Science and Technology*, Elsevier, 2001, p. 9052–9057. doi: 10.1016/B0-08-043152-6/01633-8.

[42] C. Zhao, J. Chen, Y. Li, D. W. Huang, e W. Li, “DFT study of interactions between calcium hydroxyl ions and pyrite, marcasite, pyrrhotite surfaces”, *Appl Surf Sci*, vol. 355, p. 577–581, nov. 2015, doi: 10.1016/J.APSUSC.2015.07.081.

[43] E. C. Dos Santos, J. C. De Mendonça Silva, e H. A. Duarte, “Pyrite Oxidation Mechanism by Oxygen in Aqueous Medium”, *Journal of Physical Chemistry C*, vol. 120, nº 5, p. 2760–2768, fev. 2016, doi: 10.1021/ACS.JPCC.5B10949.

[44] H. F. Steger, “Oxidation of sulfide minerals: VII. Effect of temperature and relative humidity on the oxidation of pyrrhotite”, *Chem Geol*, vol. 35, nº 3–4, p. 281–295, abr. 1982, doi: 10.1016/0009-2541(82)90006-7.

[45] H. A. Duarte, “FERRO - UM ELEMENTO QUÍMICO ESTRATÉGICO QUE PERMEIA HISTÓRIA, ECONOMIA E SOCIEDADE”, *Quim Nova*, vol. 42, nº 10, p. 1146–1153, fev. 2020, doi: 10.21577/0100-4042.20170443.

[46] P. A. M. D. Irac, “Quantum mechanics of many-electron systems”, *Proceedings of the Royal Society of London. Series A, Containing Papers of a Mathematical and Physical Character*, vol. 123, nº 792, p. 714–733, abr. 1929, doi: 10.1098/RSPA.1929.0094.

[47] I. N. . Levine, *Quantum chemistry*. Pearson, 2014.

[48] E. B. W. Linus Pauling, “Introduction to Quantum Mechanics with Applications to Chemistry”.

[49] S. Vianna A.; Canuto, *Teoria quântica de moléculas e sólidos : simulação computacional*. Livraria da Física, 2004.

[50] M. Born e R. Oppenheimer, “Zur Quantentheorie der Molekeln”, *Ann Phys*, vol. 389, nº 20, p. 457–484, jan. 1927, doi: 10.1002/ANDP.19273892002.

[51] N. S. O. Attila Szabo, “Modern Quantum Chemistry: Introduction to Advanced Electronic Structure Theory”.

[52] K. Burke, “The ABC of DFT”, 2007, *University of California, Department of Chemistry, University of California, Irvine, CA 92697*.

[53] D. R. Hartree, “The Wave Mechanics of an Atom with a Non-Coulomb Central Field. Part I. Theory and Methods”, *Mathematical Proceedings of the Cambridge Philosophical Society*, vol. 24, nº 1, p. 89–110, 1928, doi: 10.1017/S0305004100011919.

[54] N. H. & C. K. Morgon, *Métodos de Química Teórica E Modelagem Molecular*. São Paulo: Livraria da Física, 2007.

[55] H. A. Duarte e W. R. Rocha, “Teoria do Funcional de Densidade”, em *Métodos de Química Teórica e Modelagem Molecular*, São Paulo, 2007, Capítulo 3, p. 73–111.

[56] P. Hohenberg e W. Kohn, “Inhomogeneous electron gas”, *Physical Review*, vol. 136, nº 3B, p. B864, nov. 1964, doi: 10.1103/PHYSREV.136.B864.

[57] Y. W. Robert G. Parr, *Density Functional Theory of Atoms and Molecules*. 1994.

[58] E. Engel e R. M. Dreizler, “Density Functional Theory: An Advanced Course”, em Theoretical and Mathematical Physics. , Berlin, Heidelberg: Springer Berlin Heidelberg, 2011, Capítulo 2.

[59] W. Kohn e L. J. Sham, “Self-consistent equations including exchange and correlation effects”, *Physical Review*, vol. 140, nº 4A, p. A1133, nov. 1965, doi: 10.1103/PHYSREV.140.A1133.

[60] Nguyen Tuan Hung, Riichiro Saito, e Ahmad Nugraha, *Quantum ESPRESSO Course for Solid-state Physics*. Jenny Stanford, 2022.

[61] D. Rappoport, N. R. M. Crawford, F. Furche, e K. Burke, “Which functional should I choose?”, 2008.

[62] Efthimios. Kaxiras, *Atomic and electronic structure of solids*, 1st edition. Cambridge : Cambridge University Press, 2007.

[63] Ivan Oliveira e Vitor de Jesus, *Introdução à Física do Estado Sólido* , 2ª edição. 2011.

[64] P. Kratzer e J. Neugebauer, “The basics of electronic structure theory for periodic systems”, *Front Chem*, vol. 7, nº MAR, p. 436184, mar. 2019, doi: 10.3389/FCHEM.2019.00106.

[65] N. Ashcroft, *Solid State Physics* , 1ª edição. Brooks/Cole, 1976.

[66] D. Vanderbilt, “Soft self-consistent pseudopotentials in a generalized eigenvalue formalism”, *Phys Rev B*, vol. 41, nº 11, p. 7892, abr. 1990, doi: 10.1103/PhysRevB.41.7892.

[67] R. F. W. Bader, “A Quantum Theory of Molecular Structure and Its Applications”, *Chem Rev*, vol. 91, nº 5, p. 893–928, jul. 1991, doi: 10.1021/CR00005A013.

[68] C. F. Matta e R. J. Boyd, “An Introduction to the Quantum Theory of Atoms in Molecules”, *The Quantum Theory of Atoms in Molecules: From Solid State to DNA and Drug Design*, p. 1–34, abr. 2007, doi: 10.1002/9783527610709.CH1.

[69] A. Otero-De-La-Roza, E. R. Johnson, e V. Luaña, “Critic2: A program for real-space analysis of quantum chemical interactions in solids”, *Comput Phys Commun*, vol. 185, nº 3, p. 1007–1018, mar. 2014, doi: 10.1016/J.CPC.2013.10.026.

[70] A. Savin, R. Nesper, S. Wengert, e T. F. Fässler, “ELF: The Electron Localization Function”, *Angewandte Chemie International Edition in English*, vol. 36, nº 17, p. 1808–1832, set. 1997, doi: 10.1002/ANIE.199718081.

[71] A. Ormeci, H. Rosner, F. R. Wagner, M. Kohout, e Y. Grin, “Electron localization function in full-potential representation for crystalline materials”, *Journal of Physical Chemistry A*, vol. 110, nº 3, p. 1100–1105, fev. 2006, doi: 10.1021/JP054727R.

[72] A. D. Becke e K. E. Edgecombe, “A simple measure of electron localization in atomic and molecular systems”, *J Chem Phys*, vol. 92, nº 9, p. 5397–5403, maio 1990, doi: 10.1063/1.458517.

[73] W. Setyawan e S. Curtarolo, “High-throughput electronic band structure calculations: Challenges and tools”, *Comput Mater Sci*, vol. 49, nº 2, p. 299–312, ago. 2010, doi: 10.1016/J.COMMATSCI.2010.05.010.

[74] C. H. Priyadarshini, V. Sudha, e S. Harinipriya, “Computational mechanistic insights on Ag2O as a host for Li in lithium-ion batteries”, *Physical Chemistry Chemical Physics*, vol. 24, nº 26, p. 16112–16124, jul. 2022, doi: 10.1039/D2CP01674E.

[75] P. Giannozzi *et al.*, “QUANTUM ESPRESSO: a modular and open-source software project for quantumsimulations of materials”, *Journal of Physics: Condensed Matter*, vol. 21, nº 39, p. 395502, set. 2009, doi: 10.1088/0953-8984/21/39/395502.

[76] J. P. Perdew, K. Burke, e M. Ernzerhof, “Generalized Gradient Approximation Made Simple”, *Phys Rev Lett*, vol. 77, nº 18, p. 3865, out. 1996, doi: 10.1103/PhysRevLett.77.3865.

[77] H. J. Monkhorst e J. D. Pack, “Special points for Brillouin-zone integrations”, *Phys Rev B*, vol. 13, nº 12, p. 5188, jun. 1976, doi: 10.1103/PhysRevB.13.5188.

[78] V. I. Anisimov, J. Zaanen, e O. K. Andersen, “Band theory and Mott insulators: Hubbard *U* instead of Stoner *I*”, *Phys Rev B*, vol. 44, nº 3, p. 943, jul. 1991, doi: 10.1103/PhysRevB.44.943.

[79] C. E. Patrick e F. Giustino, “GW quasiparticle bandgaps of anatase TiO 2 starting from DFT+U”, *Journal of Physics Condensed Matter*, vol. 24, nº 20, maio 2012, doi: 10.1088/0953-8984/24/20/202201,.

[80] N. S. Portillo-Vélez, O. Olvera-Neria, I. Hernández-Pérez, e A. Rubio-Ponce, “Localized electronic states induced by oxygen vacancies on anatase TiO2 (101) surface”, *Surf Sci*, vol. 616, p. 115–119, out. 2013, doi: 10.1016/J.SUSC.2013.06.006.

[81] S. Baroni, P. Giannozzi, e E. Isaev, “Density-Functional Perturbation Theory for Quasi-Harmonic Calculations”, *Rev Mineral Geochem*, vol. 71, nº 1, p. 39–57, jan. 2010, doi: 10.2138/RMG.2010.71.3.

[82] G. Yang, M. Xiong, Y. Zhou, X. Tao, Q. Peng, e Y. Ouyang, “The effects of temperature and pressure on the physical properties and stabilities of point defects and defect complexes in B1-ZrC”, *Comput Mater Sci*, vol. 198, p. 110694, out. 2021, doi: 10.1016/J.COMMATSCI.2021.110694.

[83] J. hua CHEN, Y. CHEN, e Y. qiong LI, “Effect of vacancy defects on electronic properties and activation of sphalerite (110) surface by first-principles”, *Transactions of Nonferrous Metals Society of China*, vol. 20, nº 3, p. 502–506, mar. 2010, doi: 10.1016/S1003-6326(09)60169-2.

[84] C. De Oliveira, D. R. Salahub, H. A. De Abreu, e H. A. Duarte, “Native defects in α-Mo2C: Insights from first-principles calculations”, *Journal of Physical Chemistry C*, vol. 118, nº 44, p. 25517–25524, nov. 2014, doi: 10.1021/JP507947B.

[85] R. Dovesi, B. Civalleri, C. Roetti, V. R. Saunders, e R. Orlando, “Ab Initio Quantum Simulation in Solid State Chemistry”, p. 1–125, abr. 2005, doi: 10.1002/0471720895.CH1.

[86] L. Sun *et al.*, “Recent advances of metal vacancies in energy and environmental catalysis: Synthesis, characterization, and roles”, *Green Energy & Environment*, vol. 10, nº 1, p. 84–108, jan. 2025, doi: 10.1016/J.GEE.2024.02.005.

[87] K. Shimada *et al.*, “Spin-integrated and spin-resolved photoemission study of Fe chalcogenides”, *Phys Rev B*, vol. 57, nº 15, p. 8845, abr. 1998, doi: 10.1103/PhysRevB.57.8845.

[88] J. R. Gosselin, M. G. Townsend, e R. J. Tremblay, “Electric anomalies at the phase transition in FeS”, *Solid State Commun*, vol. 19, nº 8, p. 799–803, jul. 1976, doi: 10.1016/0038-1098(76)90922-4.

[89] D. G. Fedorov, “Partitioning of the Vibrational Free Energy”, *Journal of Physical Chemistry Letters*, vol. 12, nº 28, p. 6628–6633, jul. 2021, doi: 10.1021/ACS.JPCLETT.1C01823.

[90] J. Rogal *et al.*, “Perspectives on point defect thermodynamics”, *physica status solidi (b)*, vol. 251, nº 1, p. 97–129, jan. 2014, doi: 10.1002/PSSB.201350155.

[91] M. S. Lucas *et al.*, “Effects of vacancies on phonon entropy of B2 FeAl”, *Phys Rev B Condens Matter Mater Phys*, vol. 80, nº 21, p. 214303, dez. 2009, doi: 10.1103/PHYSREVB.80.214303.

[92] J. C. M. Silva, H. A. De Abreu, e H. A. Duarte, “Electronic and structural properties of bulk arsenopyrite and its cleavage surfaces – a DFT study”, *RSC Adv*, vol. 5, nº 3, p. 2013–2023, dez. 2014, doi: 10.1039/C4RA13807D.

[93] Y. Aray, J. Rodriguez, D. Vega, e E. N. Rodriguez-Arias, “Correlation of the topology of the electron density of pyrite-type transition metal sulfides with their catalytic activity in hydrodesulfurization”, *Angewandte Chemie - International Edition*, vol. 39, nº 21, p. 3810–3813, nov. 2000, doi: 10.1002/1521-3773(20001103)39:21<3810::AID-ANIE3810>3.0.CO;2-N.

[94] C. De Oliveira e H. A. Duarte, “Disulphide and metal sulphide formation on the reconstructed (0 0 1) surface of chalcopyrite: A DFT study”, *Appl Surf Sci*, vol. 257, nº 4, p. 1319–1324, dez. 2010, doi: 10.1016/J.APSUSC.2010.08.059.

[95] A. L. Soares, E. C. Dos Santos, Á. Morales-García, H. A. Duarte, e H. A. De Abreu, “The Stability and Structural, Electronic and Topological Properties of Covellite (001) Surfaces.”, *ChemistrySelect*, vol. 1, nº 11, p. 2730–2741, jul. 2016, doi: 10.1002/SLCT.201600422.

[96] P. Mori-Sánchez, A. Martín Pendás, e V. Luaña, “A classification of covalent, ionic, and metallic solids based on the electron density”, *J Am Chem Soc*, vol. 124, nº 49, p. 14721–14723, dez. 2002, doi: 10.1021/JA027708T.

[97] W. G. Guimarães, G. Ferreira de Lima, e H. A. Duarte, “Probing the Local Environment of Al-Substitution into Ferrihydrite Using DFT + U Calculations”, *Journal of Physical Chemistry C*, vol. 127, nº 6, p. 3285–3294, fev. 2023, doi: 10.1021/ACS.JPCC.2C08276.

[98] W. G. Guimarães, G. F. de Lima, e H. A. Duarte, “Comparative DFT study of the oxy(hydr)oxides of iron and aluminum – structural, electronic and surface properties.”, *Surf Sci*, vol. 708, p. 121821, jun. 2021, doi: 10.1016/J.SUSC.2021.121821.

[99] A. Morales-García, A. Lenito Soares, E. C. Dos Santos, H. A. de Abreu, e H. A. Duarte, “First-Principles Calculations and Electron Density Topological Analysis of Covellite (CuS)”, 2014, doi: 10.1021/jp4114706.

[100] M. S. Schmøkel *et al.*, “Atomic properties and chemical bonding in the pyrite and marcasite polymorphs of FeS 2 : a combined experimental and theoretical electron density study †”, 2014, doi: 10.1039/c3sc52977k.

[101] W. Sun e G. Ceder, “Efficient creation and convergence of surface slabs”, *Surf Sci*, vol. 617, p. 53–59, nov. 2013, doi: 10.1016/J.SUSC.2013.05.016.

[102] A. K. Mishra, A. Roldan, e N. H. De Leeuw, “CuO Surfaces and CO2 Activation: A Dispersion-Corrected DFT+U Study”, *Journal of Physical Chemistry C*, vol. 120, nº 4, p. 2198–2214, fev. 2016, doi: 10.1021/ACS.JPCC.5B10431.

APPENDIX A – Results and complementary demonstrations

The proof of the first Hohenberg-Kohn theorem can be constructed using *reduction ad absurdum*, that is, by assuming that the statement of the theorem is false and showing that this assumption leads to a contradiction.

Assume the existence of two distinct external potentials, $V_1 \neq V_2$, that produce the same ground-state electron density $\rho(r)$. Since the Hamiltonian of the system depends on the external potential, this assumption implies the existence of two Hamiltonians:

$$\widehat{H_1} \neq \widehat{H_2} \tag{6.1.1}$$

Consequently, the ground-state wave functions associated with these Hamiltonians must also be different:

$$\Psi_1 \neq \Psi_2 \tag{6.1.2}$$

Moreover, the corresponding ground-state energies must also differ:

$$E_1 \neq E_2 \tag{6.1.3}$$

According to the variational principle, the energy of a system is minimized by its own ground-state wavefunction, which leads to the following inequalities:

$$E_1 = \langle \Psi_1 | \widehat{H_1} | \Psi_1 \rangle < \langle \Psi_2 | \widehat{H_1} | \Psi_2 \rangle \tag{6.1.4}$$

$$E_2 = \langle \Psi_2 | \widehat{H_2} | \Psi_2 \rangle < \langle \Psi_1 | \widehat{H_2} | \Psi_1 \rangle \tag{6.1.5}$$

The " $<$ " sing applies because non-degenerated states are considered.

Given that $\widehat{H_1} = \widehat{H_2} + (\widehat{H_1} - \widehat{H_2})$ and $\widehat{H_2} = \widehat{H_1} + (\widehat{H_2} - \widehat{H_1})$, and summing the two expressions above, the following inequalities is obtained:

$$E_1 + E_2 < \langle \Psi_1 | \widehat{H_1} | \Psi_1 \rangle + \langle \Psi_1 | \widehat{H_2} - \widehat{H_1} | \Psi_1 \rangle + \langle \Psi_2 | \widehat{H_2} | \Psi_2 \rangle + \langle \Psi_2 | \widehat{H_1} - \widehat{H_2} | \Psi_2 \rangle \tag{6.1.6}$$

This expression can be simplified by canceling out the ground-state energy terms and isolating the difference between the Hamiltonians acting on Ψ_1 *and* Ψ_2:

$$\langle \Psi_1 | \widehat{H_1} - \widehat{H_2} | \Psi_1 \rangle < \langle \Psi_2 | \widehat{H_1} - \widehat{H_2} | \Psi_2 \rangle \tag{6.1.7}$$

In this inequality, the only difference between the Hamiltonians lies in the external potential, as the kinetic and electron-electron repulsion terms remain unchanged. By separating the Hamiltonians, the following is obtained:

$$\langle \Psi_2 | \widehat{H_1} - \widehat{H_2} | \Psi_2 \rangle = \int [V_1(r_i) - V_2(r_i)] dr \left[N \int \Psi_2^2 dr \right] \; onde \; N \int \Psi_2^2 dr \; = \; \rho(r) \tag{6.1.8}$$

$$\langle \Psi_2 | \widehat{H_1} - \widehat{H_2} | \Psi_2 \rangle = \int dr [V_1 - V_2] \, \rho(r) \tag{6.1.9}$$

Similarly, applying the same procedure for Ψ_1:

$$\langle \Psi_1 | \widehat{H_1} - \widehat{H_2} | \Psi_1 \rangle = \int [V_1(r_i) - V_2(r_i)] dr \left[N \int \Psi_1^2 dr \right] \; onde \; N \int \Psi_1^2 dr \; = \; \rho(r) \tag{6.1.10}$$

$$\langle \Psi_1 | \widehat{H_1} - \widehat{H_2} | \Psi_1 \rangle = \int dr [V_1(r_i) - V_2(r_i)] \, \rho(r) \tag{6.1.11}$$

Returning to the inequality $\langle \Psi_1 | \widehat{H_1} - \widehat{H_2} | \Psi_1 \rangle < \langle \Psi_2 | \widehat{H_1} - \widehat{H_2} | \Psi_2 \rangle$ and substituting the expressions above leads to the contradiction, as the same integral cannot be simultaneously less than and equal to itself:

$$\int dr_i [V_1(r_i) - V_2(r_i)] \, \rho(r) < \int dr_i [V_1(r_i) - V_2(r_i)] \, \rho(r) \tag{6.1.12}$$

The only possible conclusion to resolve this contradiction is that the initial assumption is incorrect. Therefore, no two distinct external potentials can result in the same ground-state electron density. This confirms the validity of the first Hohenberg-Kohn theorem.

The first step involved evaluating the plane-wave cutoff energy. All calculations were performed using a Gamma-point k-point mesh. The total energies obtained are presented as relative values, referenced to the energy calculated with a cutoff of 10 Ry. For monoclinic pyrrhotite, the energy difference between cutoff values of 60 Ry and 70 Ry was approximately 0.0003 Ry, indicating good convergence. In the case of troilite, the energy difference between 40 Ry and 50 Ry was around 0.0003 Ry. Based on these convergence tests, cutoff energies of 60 Ry and 50 Ry were selected for monoclinic pyrrhotite and troilite, respectively.

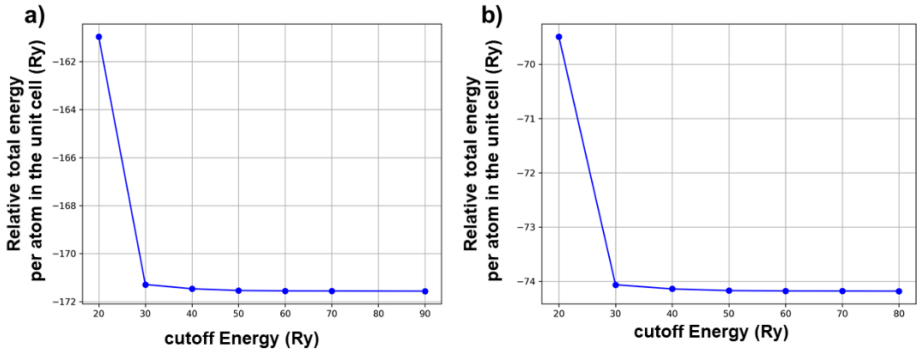

Figure A1: Convergence test for the plane-wave cutoff energy using the bulk structures of monoclinic pyrrhotite (a) and troilite (b).

The second step consisted of evaluating the convergence with respect to the k-point mesh. The total energies obtained are presented as relative values, referenced to the energy calculated with k-point mesh 1×1×1. In the convergence plots, the x-axis represents the different k-point meshes tested, while the y-axis shows the corresponding relative differences in total energy. For monoclinic pyrrhotite, the energy difference between the 2×4×2 and 3×6×3 meshes was approximately 0.001 Ry, indicating that the 2×4×2 mesh provides sufficient accuracy. In the case of troilite, the energy variation between the 1×2×1 and 2×4×2 meshes was about 0.001 Ry. Considering these results, the k-point meshes adopted for subsequent calculations were 2×4×2 for monoclinic pyrrhotite and 1×2×1 for troilite.

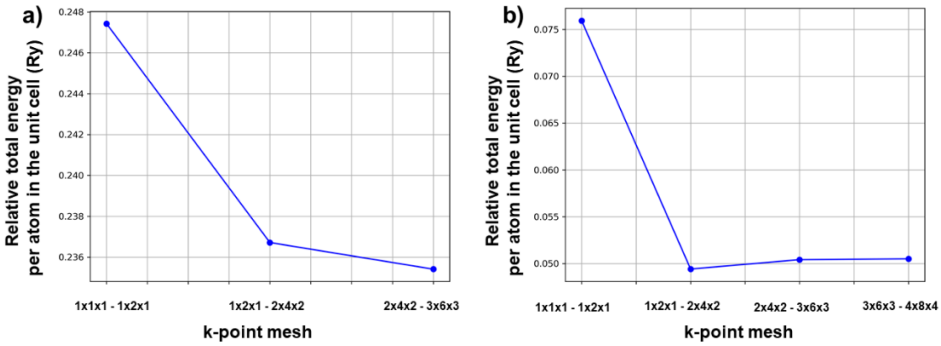

Figure A2: Convergence test for the k-point mesh used in the calculations of monoclinic pyrrhotite (a) and troilite (b).

Figures and Tables A3 and A1 present the results of the optimization for the troilite supercell with Hubbard *U* values ranging from 0 to 3 eV, and for monoclinic pyrrhotite with values ranging from 0 to 4 eV. The results indicate that a Hubbard correction of 2 eV for troilite and 1 eV for monoclinic pyrrhotite is necessary to accurately describe their crystal structures and electronic properties.

Table A1: Hubbard Correction ranging from 0 to 3 eV: Evaluation of its impact on the Lattice Parameters and the band-gap of Troilite.

U (eV)	Lattice parameters (Å)			Band gap (eV)
	a	c	c/a	
0	5.869 (0.089)	10.892 (0.848)	1.86 (0.11)	No band gap
1	5.971 (0.013)	11.693 (0.047)	1.96 (0.01)	No band gap
2	6.039 (0.081)	11.796 (0.056)	1.95 (0.02)	0.12
3	5.895 (0.063)	11.025 (0.715)	1.87 (0.1)	0.20
Experimental	5.965	11.757	1.97	0.04

Besides the crystal structure, troilite also exhibits an experimental band gap of 0.04 eV. To reproduce this minimum band gap, a Hubbard correction of 2 eV is required. This value is consistent with the optimization of the lattice parameters. Figure X presents the band gap as determined from the analysis of the density of states.

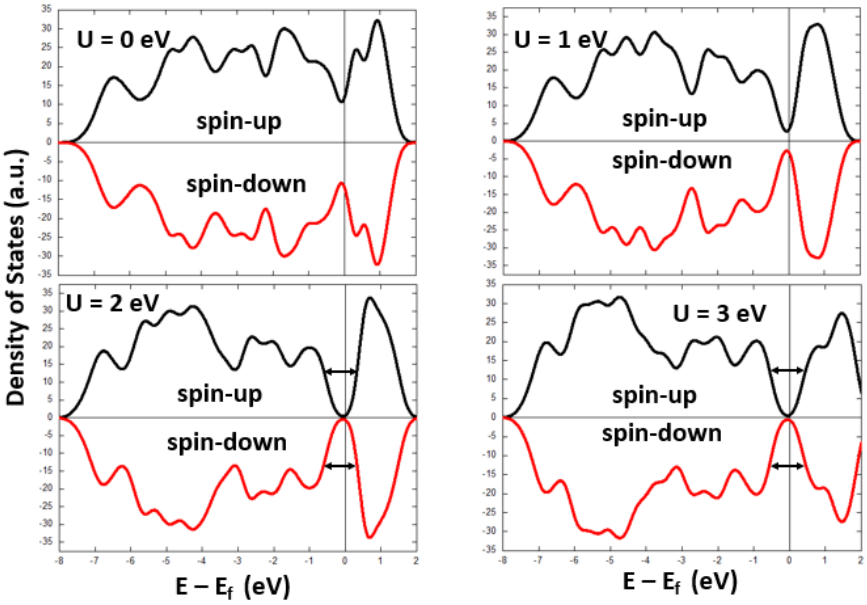

Figure A3: Density of states with various Hubbard corrections applied illustrating the effects of the Hubbard parameter on the band gap of troilite.

Table A2: Hubbard Correction ranging from 0 to 4 eV: Evaluation of its impact on the Lattice Parameters of monoclinic pyrrhotite.

U (eV)	Lattice parameters (Å)			
	a	b	c	c/a
0	11,241 (0,656)	6,688 (0,171)	11,464 (1,427)	1,02 (0,06)
1	11,767 (0,130)	6,795 (0,064)	12,570 (0,321)	1,07 (0,01)
2	12,060 (0,163)	7,000 (0,141)	13,031 (0,140)	1,08 (0,00)
3	12,271 (0,374)	7,048 (0,189)	13,041 (0,150)	1,06 (0,02)
4	12,377 (0,480)	7,113 (0,254)	13,165 (0,274)	1,06 (0,02)
Experimental	11,897	6,8586	12,891	1,08

During the vacancy formation process in the troilite structure, the iron atoms that were removed are highlighted in red in the respective unit cell, clearly indicating their original positions prior to removal.

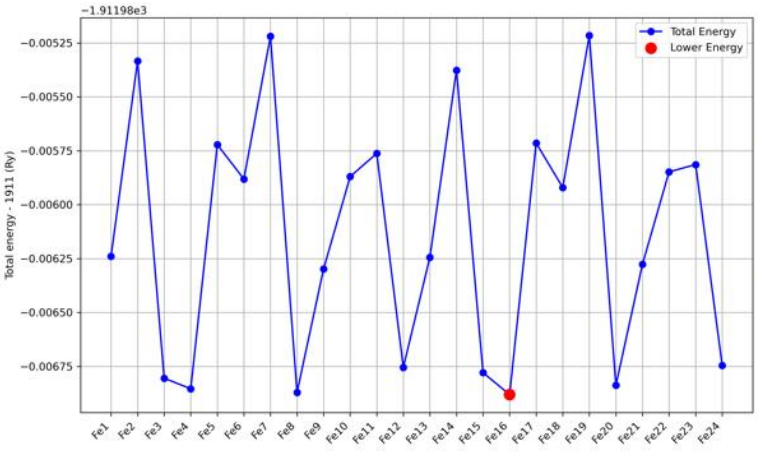

First iron atom removed

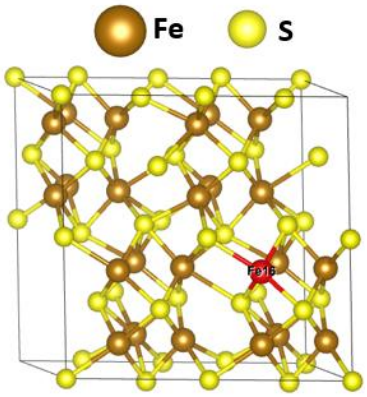

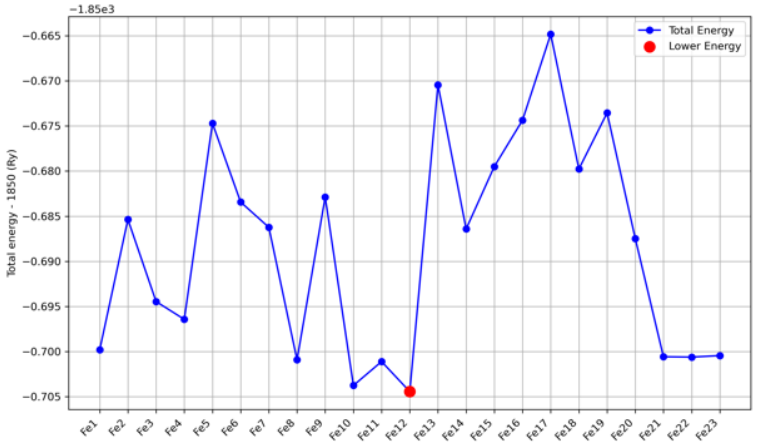

Second iron atom removed

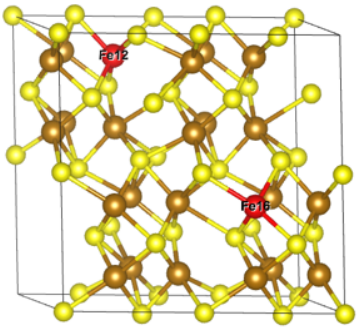

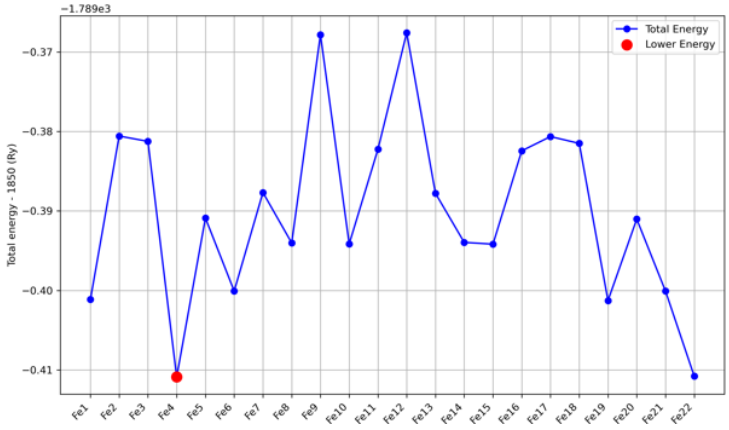

Third iron atom removed

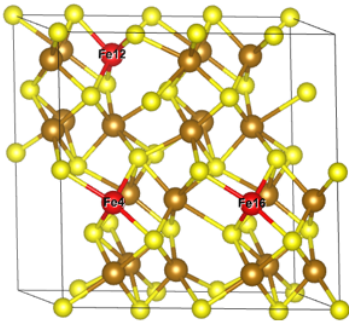

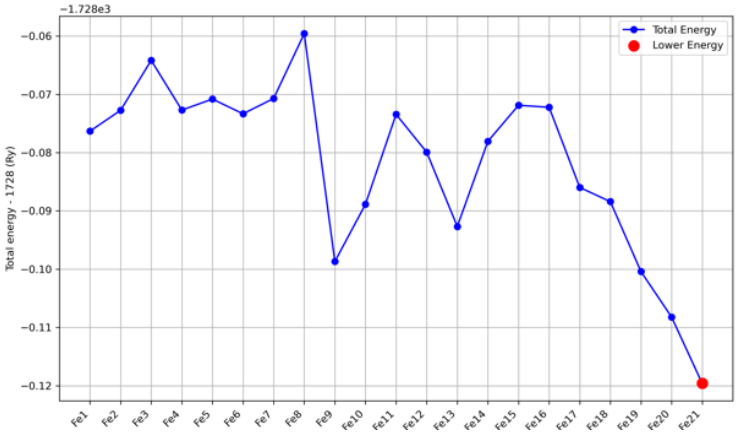

Fourth iron atom removed

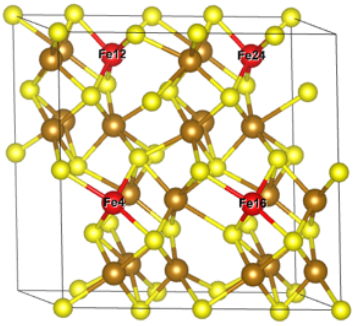

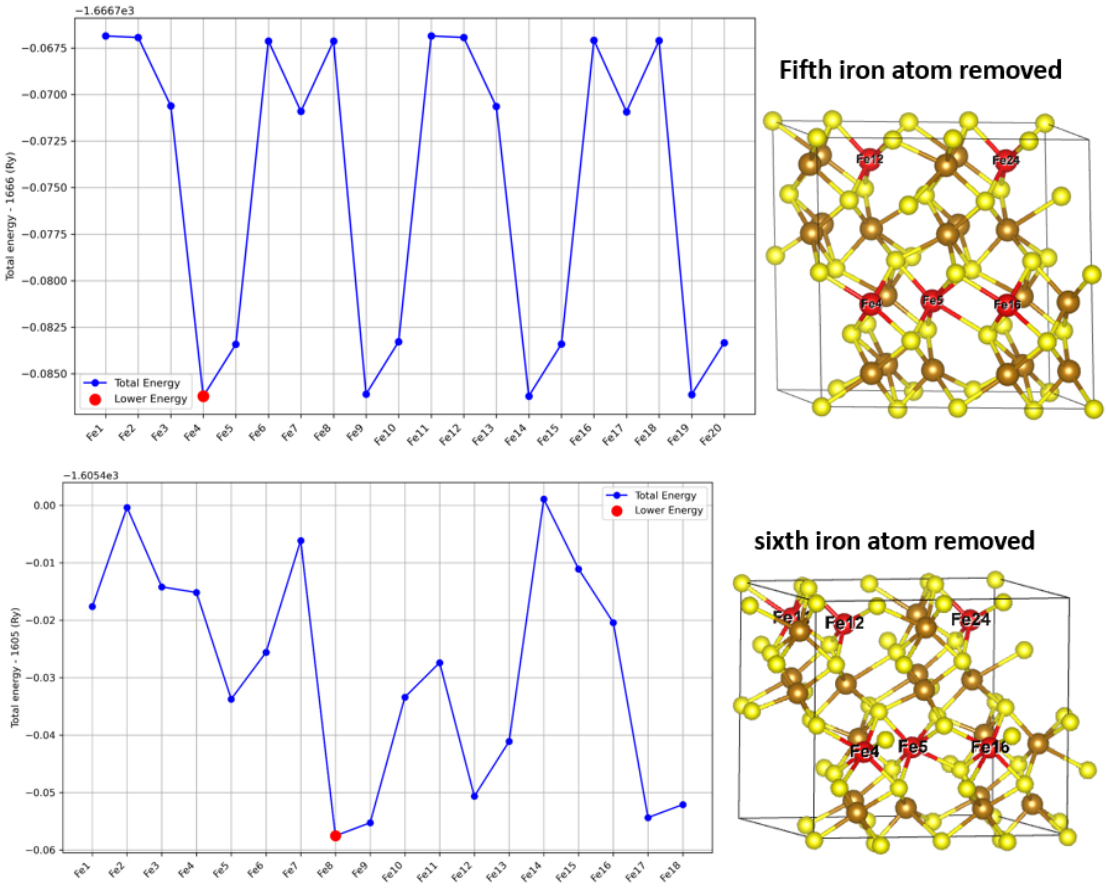

Figure A4: Total energy of different configurations for the first six iron vacancies. In red is represented the vacancy for the most stable configuration.

Band structure of troilite within the range of -8 eV to 2 eV, along with the project density of states, highlining the orbital contributions to the band structure.

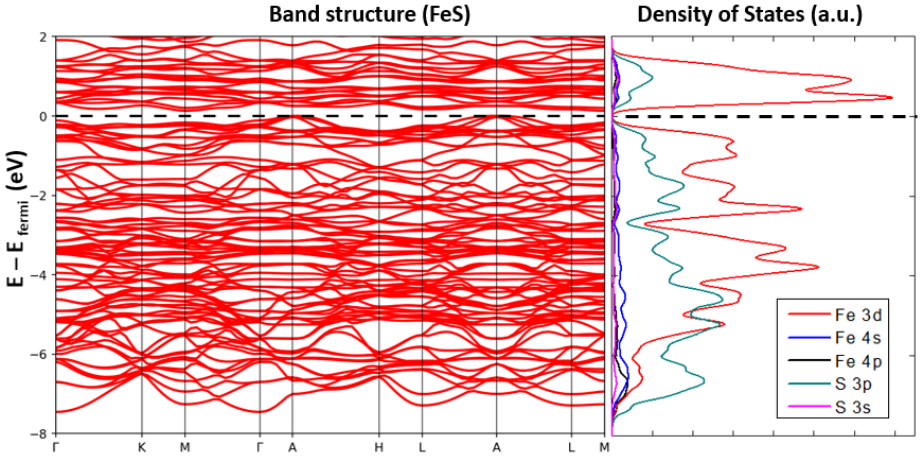

Figure A5: Band Structure and Projected Density of States of Troilite highlighting the orbital contributions (-8 eV to 2 eV).

Table A3: Thermodynamic values, including the Helmholtz vibrational free energy, vibrational entropy, and vibrational entropy calculated per atom for the pristine troilite structure ($Fe_{24}S_{24}$).

	$Fe_{24}S_{24(s)}$		
Temperature K	F vibrational (eV)	S vibrational (eV)	E vibrational (eV)
0	0.1205174	0.0000009	0.0602587
50	0.1204325	0.0000017	0.0603013
100	0.1201721	0.0000034	0.0604262
150	0.1197320	0.0000054	0.0606739
200	0.1191066	0.0000071	0.0609705
250	0.1182892	0.0000091	0.0614122
300	0.1172734	0.0000111	0.0619531
350	0.1160527	0.0000133	0.0626891
400	0.1146221	0.0000153	0.0634336
450	0.1129776	0.0000176	0.0643971
500	0.1111162	0.0000198	0.0654789
550	0.1090365	0.0000218	0.0665224
600	0.1067378	0.0000241	0.0678250
650	0.1042208	0.0000264	0.0692451
700	0.1014865	0.0000283	0.0705849
750	0.0985371	0.0000306	0.0722282
800	0.0953750	0.0000326	0.0737651
850	0.0920032	0.0000349	0.0756365
900	0.0884252	0.0000368	0.0773765
950	0.0846445	0.0000388	0.0792135
1000	0.0806644	0.0000408	0.0811493

Unit cell and structural data for the stoichiometric monoclinic pyrrhotite.

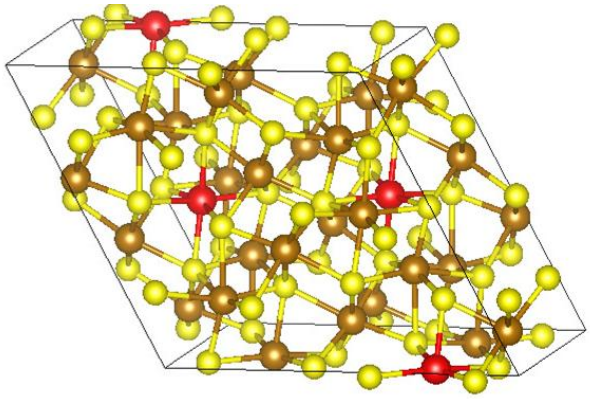

Lattice constant	
A (Å)	1.12769e+01
B (Å)	6.76632e+00
C (Å)	1.23595e+01
α (Degree)	8.98088e+01
β (Degree)	1.16482e+02
γ (Degree)	9.07581e+01

Figure A6: Unit cell and lattice parameters of stoichiometric monoclinic pyrrhotite ($Fe_{32}S_{32}$). Red spheres indicate the iron atoms added to complete the structure. The atomic coordinates are provided in the XYZ below.

64

Fe32 S32

Fe	-0.058703	4.609677	3.087801
Fe	-0.022758	2.148205	9.285640
Fe	5.032490	1.226807	0.562239
Fe	4.979584	5.530960	6.782588
Fe	8.875502	1.285980	-4.259030
Fe	1.091498	1.335969	5.411407
Fe	1.136617	5.471800	11.603778
Fe	8.920596	5.421688	1.933298
Fe	3.784176	4.668759	-1.733456
Fe	6.094032	4.718860	2.908367
Fe	6.227732	2.088866	9.078145
Fe	3.918351	2.038838	4.436181
Fe	7.920020	0.709340	5.423635
Fe	2.176918	0.875751	8.096087
Fe	2.092088	6.048352	1.921175
Fe	7.835486	5.882551	-0.751273
Fe	2.828778	4.092046	7.949190
Fe	7.179199	4.258330	5.593059
Fe	7.183276	2.665481	-0.604473
Fe	2.833074	2.499710	1.751756
Fe	6.173039	0.707911	3.153105
Fe	3.928232	0.671894	10.338167
Fe	3.839124	6.049832	4.191687
Fe	6.083614	6.085607	-2.993139
Fe	1.081812	4.090706	5.678607
Fe	8.930665	4.054808	7.835149
Fe	8.930392	2.666974	1.666044
Fe	1.081273	2.702835	-0.490071
Fe	4.971814	3.944954	0.583311
Fe	5.040364	2.812898	6.761335
Fe	10.063024	0.562107	-1.942257
Fe	-0.050870	6.195835	9.287014

S	7.772846	0.901259	-2.212857
S	2.295366	0.883313	3.458845
S	2.239194	5.856536	9.557491
S	7.716832	5.874478	3.885836
S	2.681682	4.284186	0.312851
S	7.297772	4.266131	0.955807
S	7.330424	2.473618	7.031928
S	2.714392	2.491639	6.388655
S	10.050921	0.786280	6.071676
S	0.031613	0.810301	7.435480
S	-0.038778	5.971511	1.273151
S	9.980687	5.947625	-0.090654
S	4.959681	4.169020	8.597198
S	5.033979	4.193073	4.932384
S	5.052401	2.588616	-1.252424
S	4.978297	2.564775	2.412305
S	5.430653	0.656336	5.322184
S	4.686796	0.694796	8.176983
S	4.581524	6.101411	2.022659
S	5.325194	6.062834	-0.832089
S	0.339469	4.039224	7.847731
S	9.689282	4.077688	5.674028
S	9.672666	2.718525	-0.503011
S	0.322818	2.680056	1.670928
S	7.318620	0.960224	0.961856
S	2.729014	0.909034	0.127267
S	2.693542	5.797496	6.382838
S	7.283060	5.848765	7.217794
S	2.227405	4.343098	3.487471
S	7.731426	4.291883	-2.375802
S	7.784768	2.414678	3.857256
S	2.280708	2.466044	9.720942

Table A4: Thermodynamic values, including the Helmholtz vibrational free energy, vibrational entropy, and vibrational entropy calculated per atom for the defect free monoclinic pyrrhotite ($Fe_{32}S_{32}$).

	$Fe_{32}S_{32}$		
Temperature K	F vibrational (eV)	S vibrational (eV)	E vibrational (eV)
0	0.0028327	0.0000000	0.0028327
50	0.0027864	0.0000009	0.0028290
100	0.0026345	0.0000030	0.0029321
150	0.0023603	0.0000055	0.0031894
200	0.0019628	0.0000079	0.0035359
250	0.0014501	0.0000102	0.0040012
300	0.0008334	0.0000123	0.0045324
350	0.0001234	0.0000142	0.0051086
400	-0.0006703	0.0000159	0.0057074
450	-0.0015396	0.0000174	0.0063050
500	-0.0024776	0.0000187	0.0068764
550	-0.0034783	0.0000200	0.0075125
600	-0.0045369	0.0000213	0.0082184
650	-0.0056489	0.0000223	0.0088603
700	-0.0068107	0.0000232	0.0094099
750	-0.0080188	0.0000242	0.0101576
800	-0.0092704	0.0000251	0.0107980
850	-0.0105630	0.0000259	0.0114825
900	-0.0118943	0.0000266	0.0120220
950	-0.0132622	0.0000274	0.0127906
1000	-0.0146648	0.0000281	0.0133970

Table A5: Concentration of iron vacancies (x), cohesive energy (in eV/atom), vacancy formation energy for each molar fraction (in eV/atom), optimized lattice constants (a, b, c in Å) for the defect free monoclinic pyrrhotite ($Fe_{32}S_{32}$).

x	**a**	**b**	**c**	$\mathbf{E^{cohesive}}$	$\mathbf{E^{vac}}$
0.00000	11.277	6.766	12.360	-6.166	0.000
0.03125	11.118	6.620	11.877	-6.149	7.217
0.06250	11.114	6.472	12.213	-6.131	7.250
0.09375	11.144	6.462	12.156	-6.112	7.250

Table A6: Bulk energy, surface area, and energy of the nine unrelaxed surface generated by the cleavage planes (001), (010), and (100).

Cleavage plane (001)			
Surface	Slab energy (eV)	Area $Å^2$	$\gamma_{nre}\ (eV/Å^2)$
1º	-32431.35	75.96	0.104
2º	-32434.01		0.087
3º	-32428.69		0.121
Cleavage plane (010)			
Surface	Slab energy (eV)	Area $Å^2$	$\gamma_{nre}\ (eV/Å^2)$
1º	-32405.27	131.58	0.162
2º	-32407.22		0.155
3º	-32405.26		0.162
Cleavage plane (100)			
Surface	Slab energy (eV)	Area $Å^2$	$\gamma_{nre}\ (eV/Å^2)$
1º	-32403.41	85.42	0.261
2º	-32404.75		0.253
3º	-32407.42		0.237
The bulk energy is -32447.99 eV.			

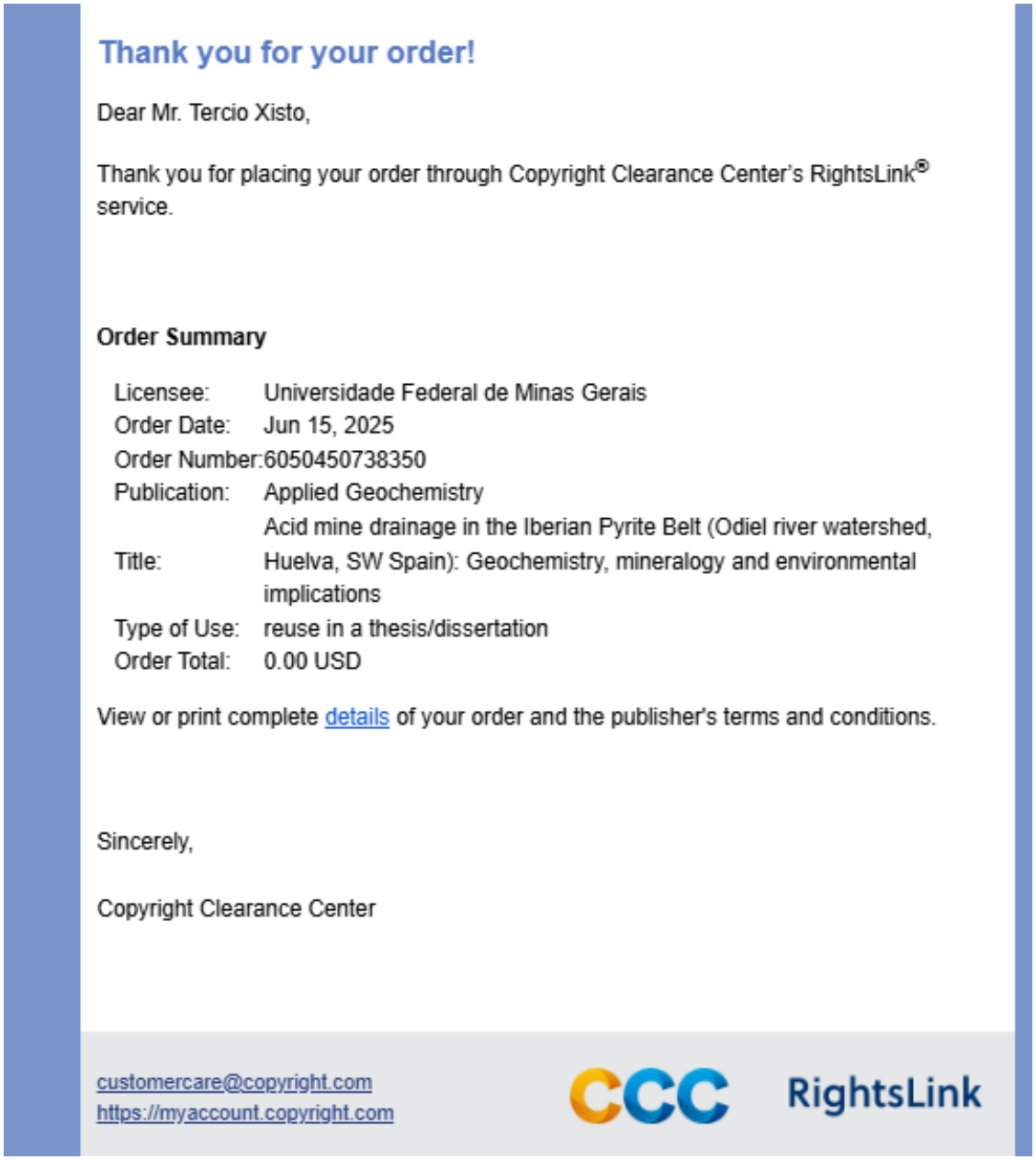

Thank you for your order!

Dear Mr. Tercio Xisto,

Thank you for placing your order through Copyright Clearance Center's RightsLink® service.

Order Summary

Licensee:	Universidade Federal de Minas Gerais
Order Date:	Jun 15, 2025
Order Number:	6050450738350
Publication:	Applied Geochemistry
Title:	Acid mine drainage in the Iberian Pyrite Belt (Odiel river watershed, Huelva, SW Spain): Geochemistry, mineralogy and environmental implications
Type of Use:	reuse in a thesis/dissertation
Order Total:	0.00 USD

View or print complete details of your order and the publisher's terms and conditions.

Sincerely,

Copyright Clearance Center

customercare@copyright.com
https://myaccount.copyright.com

CCC RightsLink

Figure A7: Image reused with permission from Applied Geochemistry (Order No. 6050450738350, June 15, 2025), from the article 'Acid mine drainage in the Iberian Pyrite Belt (Odiel river watershed, Huelva, SW Spain): Geochemistry, mineralogy and environmental implications.' Licensed to Universidade Federal de Minas Gerais. Copyright Clearance Center.

Participação em eventos, congressos, exposições e feiras

1. 48ª Reunião Anual da Sociedade Brasileira de Química. A DFT Study of the thermodynamic transformation of troilite into pyrrhotite. 2025. (Congresso).
2. 36º Encontro Regional da Sociedade Brasileira de Química de Minas Gerais (ERSBQ-MG). EXPLORING THE ELECTRONIC AND TOPOLOGICAL PROPERTIES OF MONOCLINIC PYRRHOTITE. 2024. (Congresso).
3. 47ª Reunião Anual da Sociedade Brasileira de Química. Investigation of the properties of pyrrhotite and troilite through DFT calculations. 2024. (Congresso).
4. Brazilian Meeting on Inorganic Chemistry. CLEAVAGE SURFACE AND OXYGEN ADSORPTION ON (001) MONOCLINIC PYRRHOTITE: A DFT STUDY. 2024. (Congresso).

Apresentação de trabalho

1. SILVA JUNIOR, E. ; **XISTO, T. P. F.** ; DUARTE, H. A. . Electronic Structure and Properties of Cu2S A DFT Study. 2025. (Apresentação de Trabalho/Congresso).
2. **XISTO, T. P. F.**; SILVA JUNIOR, E. A DFT Study of the thermodynamic transformation of troilite into pyrrhotite. 2025. (Apresentação de Trabalho/Congresso).
3. **XISTO, T. P. F.**; DUARTE, H. A. Investigation of the properties of pyrrhotite and troilite through DFT calculations. 2024. (Apresentação de Trabalho/Congresso).
4. **XISTO, T. P. F.**; DUARTE, H. A. CLEAVAGE SURFACE AND OXYGEN ADSORPTION ON (001) MONOCLINIC PYRRHOTITE: A DFT STUDY. 2024. (Apresentação de Trabalho/Congresso).
5. SILVA JUNIOR, E. ; **XISTO, T. P. F.** ; DUARTE, H. A. . From Troilite to Pyrrhotite: the effect of Fe vacancies on the electronic Properties. 2024. (Apresentação de Trabalho/Congresso).
6. SILVA JUNIOR, E. ; **XISTO, T. P. F.** ; DUARTE, H. A. . FORMAÇÃO DE VACÂNCIAS DE FERRO NA TROLITA E CARACTERIZAÇÃO DE SUAS PROPRIEDADES ELETRÔNICAS E TOPOLÓGICAS. 2024. (Apresentação de Trabalho/Congresso).
7. **XISTO, T. P. F.**; DUARTE, H. A. EXPLORING THE ELECTRONIC AND TOPOLOGICAL PROPERTIES OF MONOCLINIC PYRRHOTITE. 2024. (Apresentação de Trabalho/Congresso).

8. MENDES, A. C. G. ; SILVA JUNIOR, E. ; **XISTO, T. P. F.** ; DUARTE, H. A. . A química dos sulfetos minerais mitigando impactos ambientais na mineração. 2024. (Apresentação de Trabalho/Comunicação).